INAUGURAL-DISSERTATION

zur

Erlangung der Doktorwürde

der

Naturwissenschaftlich-Mathematischen

Gesamtfakultät

der

Ruprechts-Karls-Universität

Heidelberg

vorgelegt von

Dipl.-Phys. Detlef Rost

aus Hannover

Tag der mündlichen Prüfung: 26. Juli 2000

TOF-SIMS Analysen interplanetarer Staubteilchen

Gutachter: Prof. Dr. Elmar K. Jessberger

Prof. Dr. Ulrich Platt

Dissertation
submitted to the
Combined Faculties for the Natural Sciences and for Mathematics
of the Rubertus Carola University of Heidelberg, Germany
for the degree of
Doctor of Natural Sciences

TOF-SIMS analyses of interplanetary dust particles

presented by

Diplom-Physicist: Detlef Rost
born in: Hannover

Heidelberg, July 26, 2000

Referees: Prof. Dr. Elmar K. Jessberger

Prof. Dr. Ulrich Platt

TOF-SIMS Analysen interplanetarer Staubteilchen

Diese Arbeit ist Teil einer umfassenden Untersuchung von interplanetaren Staubteilchen (IDPs), die in der Stratosphäre gesammelt werden. IDPs können grundlegende Informationen über das frühe und äußere Sonnensystem liefern. Das oberste Ziel ist zunächst eine eindeutige Unterscheidung ihrer Herkunft: Kometen oder Asteroiden. Bevor jedoch solche Schlüsse gezogen werden können, müssen nachträgliche Veränderungen erkannt werden, die die Eigenschaften der Teilchen beeinflussen würden, z. B. eine Kontamination in der Stratosphäre.

Die geringe Größe der IDPs, nur $\sim 20\,\mu m$, erfordert hochentwickelte Analysemethoden wie die Sekundärionen-Flugzeitmassenspektrometrie (TOF-SIMS). Diese ermöglicht die nahezu zerstörungsfreie Elementanalyse von Teilchenoberflächen und -schnitten bei hoher lateraler Auflösung.

Obwohl TOF-SIMS eigentlich flache Proben voraussetzt, konnte diese Technik mit Hilfe von Modellrechnungen nun auch auf raue Oberflächen angewandt werden. Das Modell wurde an stratosphärischen Al_2O_3-Kügelchen erfolgreich überprüft. Die TOF-SIMS Ergebnisse von 17 stratosphärischen Staubteilchen zeigen, dass sie mit Halogenen kontaminiert sind, was weitreichende Konsequenzen für die IDP-Forschung hat. Diese Entdeckung wurde außerdem durch den Nachweis oberflächennaher Halogene in den Schnitten bestätigt.

In den IDP-Schnitten konnten mehrere unerwartete Minerale wie Mn-Sulfid sowie Mineralparagenesen nachgewiesen werden. Es wurde hier erstmals der Versuch unternommen, Untersuchungsergebnisse von TOF-SIMS mit PIXE- und SEM-Analysen identischer IDPs in Verbindung zu bringen, aufgrund der sehr unterschiedlichen Informationsvolumina ein schwieriges Problem. Eine vollständige Interpretation aller Daten wird erst nach weiteren TEM-Studien möglich sein.

TOF-SIMS analyses of interplanetary dust particles

This thesis is part of a comprehensive study on interplanetary dust particles (IDPs), collected in the stratosphere, that potentially bear information on the early and outer solar system. The first goal is to unambiguously establish the source of individual IDPs — comets or asteroids. However, secondary processes like stratospheric surface contamination could alter their original properties. It is thus indispensable to discern such influences before IDP sources can be deduced.

Particle sizes of only $\sim 20\,\mu m$ require sophisticated analytical tools as time-of-flight secondary ion mass spectrometry (TOF-SIMS). It enables almost nondestructive surface and section elemental analyses with high lateral resolution.

Designed for flat samples, the TOF-SIMS data interpretation for the first time was adapted to rough surfaces with model calculations that were experimentally tested with stratospheric Al_2O_3 spheres. TOF-SIMS results on 17 stratospheric particles indicate that they are halogen contaminated, a finding that seriously has to be considered in IDP research. It is corroborated by the TOF-SIMS detection of halogens close to the original surfaces of several sectioned IDPs.

In IDP sections a number of unexpected minerals, like Mn-sulfide, and mineral parageneses were detected. It is attempted for the first time to synthesize the results of TOF-SIMS with PIXE and SEM results on the very same IDPs, a complex problem because of the very different volumes of information. A full interpretation of the whole — and very large — data set, however, must await the results of the upcoming TEM study.

Contents

Chapter 1

Introduction

A central question in planetology is the formation of the solar system 4.6 Ga ago from an interstellar ('solar') dust cloud. One wants to know what the precursor material was, where it came from, when it was formed, and how it finally built up the Sun, the planets and moons, the asteroids, the comets, and the Kuiper belt objects. Concerning the smaller bodies of the solar system, asteroids are relics from the genesis of planets, *i.e.*, planetary building blocks that were prevented from further agglomeration by gravitational disturbances from Jupiter. The larger ones experienced significant differentiation processes. Comets and Kuiper belt objects, however, are supposed to be genuine remnants of the solar dust cloud. The investigation of meteorites, whose parent bodies are asteroids, contributed much to the understanding of the early solar system, especially to the formation process of planets. Comets, on the other hand, should enlighten the very nature of the solar system source material. But up to now no proven cometary material was available for laboratory analysis. Besides expensive space missions like Stardust, which will capture some cometary dust in aerogel and bring it back to Earth, also a cheaper and easier way is available: interplanetary dust particles (IDPs).

IDPs are submillimeter sized fragments of asteroids and comets, occurring all over the ecliptic plane. Most of them spiral into the Sun on a time scale of 10000 a (Dohnanyi, 1978). Some are captured by Earth's gravitational field and even survive the atmospheric deceleration from velocities > 11.2 km/s. They represent a significant portion of all stratospheric dust particles. These particles were first sampled with aid of balloons, later by aircraft, in order to examine the extraterrestrial component (Brownlee *et al.*, 1976a). Routine collection of stratospheric dust was established by NASA in 1981, combined with a suitable particle preparation and preclassification (Warren and Zolensky, 1994).

While the majority of the collected IDPs has asteroidal parent bodies, some percent should originate from comets (Kortenkamp and Dermott, 1995). The investigation of IDPs potentially contributes to a better understanding of the early and outer solar system (Brownlee, 1994), especially if the cometary IDPs can be identified.

The small size of the particles, typically $< 50\,\mu m$, requires highly developed analytical techniques to measure basic properties like element abundances, isotopic composition, occurring minerals, and (noble) gas contents. Appropriate analyses often result in (partial) destruction of the particles thus excluding other measurements. Therefore, the existing data base on individual IDPs is rather incomplete. Nevertheless, several distinct IDP types are observed indicating different parent bodies. But individual IDPs cannot yet be unambiguously identified as asteroidal or cometary. (Chapter 2 provides an introduction to interplanetary dust particles)

Most IDPs have a chemical composition similar to CI carbonaceous chondrites, which are supposed to represent the most pristine material of our solar system (Anders and Grevesse, 1989). However, some deviations are observed on the average of all particles: S and Ca are depleted, whereas some volatile (and rare) elements are more abundant than in CI chondrites. Especially Br is enriched by 21×CI on average and up to a maximum of 10^4×CI (Arndt *et al.*, 1996b). A new class of primitive solar system material was purposed in order to account for these findings (Flynn and Sutton, 1992), but a consistent explanation for its formation could not be given. Jessberger *et al.* (1992) suggested that element enrichments may result from secondary processes at aerobreaking or during atmospheric residence, *e.g.*, a contamination with stratospheric aerosols particles. Therefore, one must first discern — and, if required, correct for — these terrestrial modifications, before conclusions on properties of parent bodies can be drawn.

Thus two fundamental topics in IDP research arise: First, as much information as possible must be gathered for individual IDPs. Second, atmospheric alteration and contamination processes must be thoroughly revealed. For this purpose a comprehensive consortium study was initiated, the *Collector Project* (Stephan *et al.*, 1994a): Individual IDPs should be analyzed successively with several techniques. Their sequence is optimized to allow a maximum of different methods. Chapter 4 gives an overview of this project, discusses the different methods, and explains the particle preparation and classification.

The present work is part of this study. Surfaces and sections of stratospheric dust particles are analyzed with time-of-flight secondary ion mass spectrometry (TOF-SIMS). A pulsed beam of primary ions sputters secondary atoms and molecules off the sample surface, with a small fraction

of them being ionized. These secondary ions are separated in a time-of-flight mass spectrometer allowing to identify them. The main advantages of this method are high lateral resolution ($\geq 0.2\,\mu m$), simultaneous detection of all ions with the same polarity, and low sample consumption of several monolayers. Chapter 3 explains TOF-SIMS and the corresponding instrument in detail and presents a model calculation needed to understand the results from rough particle surface analysis.

TOF-SIMS is very surface sensitive, because the information depth only amounts to several monolayers. It is especially qualified to detect surface correlated element enrichments that may result from stratospheric contamination processes. The results from the analyses of IDP surfaces should be substantiated by the examination of the inner element distribution, which is achieved by investigating the respective sections.

A second focus of the TOF-SIMS study is the search for uncommon mineral phases that can be decisive to determine origin and history of individual IDPs. Minerals with distinctive compositions are easily recognized. Unlike conventional SIMS, ion species of interest need not to be selected prior to the actual measurement. However, another technique is needed for the exact characterization and unambiguously identification of the found conspicuous phases: Transmission electron microscope (TEM) analyses are scheduled for this purpose.

The results so far obtained by all methods are combined and compared. This allows a validation of the findings and provides an overall picture of the respective particles.

Chapter 5 provides the results from all TOF-SIMS analyses, separately presented for each particle. They are discussed together with the corresponding contributions from the other methods. Eventually, the significant findings are summarized in Chapter 6.

Chapter 2

Interplanetary dust particles

This chapter summarizes possible origins, history, and properties of interplanetary dust particles (IDPs), that are collected in Earth's stratosphere.

2.1 The interplanetary dust cloud

Dust particles fill the space between the larger and smaller bodies of our solar system, *i.e.*, Sun, planets, moons, asteroids, and comets. This so-called *interplanetary dust cloud* has increasingly higher density toward the ecliptic plane and is responsible for the zodiacal light that can be observed before sunrise or after sunset: the sunlight is scattered by interplanetary dust (Cassini, 1730). The term 'interplanetary dust' usually denotes submillimeter sized particles, though the size distribution is continuous up to the larger and less frequent meteoroids, the precursors of meteorites.

Comets and asteroids are the major sources of the cloud. In the asteroid belt, dust is produced by impacts or collisions. Comets contribute with particles from their dust trails, that develop at distances from the Sun less than a few AU: The solar radiation leads to a sublimation of frozen ices, carrying also away incorporated dust particles. Zook and McKay (1986) estimated the portion of cometary IDPs with diameters $< 100\,\mu\mathrm{m}$, that are crossing the Earth orbit at 1 AU, to be up to $\sim 50\,\%$, the remainder being derived by asteroids.

The density and size distribution of the interplanetary dust cloud is probably maintained on a time scale of millions of years (Morrison and Zinner, 1976). However, individual particles are estimated to have much shorter live times $\sim 10000\,\mathrm{a}$ (Dohnanyi, 1978), thus requiring a permanent dust production to keep the cloud in dynamic equilibrium. The reasons for this in detail:

Lorentz force. Bound orbits around the Sun cannot be supposed on principle, because for small particles other forces might be of the same magnitude. Particles $\lesssim 0.1\,\mu m$ can be swept out of the solar system by the Lorentz force (Hamilton *et al.*, 1995). It is caused by the Sun's magnetic field and the charging of the particles, which results from the photo effect of sunlight.

Radiation pressure. The sunlight itself has a significant influence on the trajectories of dust particles. If the ratio β of radiation pressure and gravitational force exceeds 0.5, these so-called β-meteoroids are no longer bound to the solar gravitational field (Dohnanyi, 1970; Zook and Berg, 1975). These particles have diameters up to 0.4 µm, depending on their density, shape, and albedo (Schwehm and Rohde, 1977). Also larger dust particles up to 20 µm can leave the solar system on a hyperbolic trajectory, even if $\beta \leq 0.5$, if they are in highly eccentric orbits, as it is commonly the case for cometary dust (Leinert and Grün, 1990).

Pointing-Robertson effect. Even larger particles and the IDPs with diameters $\gtrsim 0.5\,\mu m$ on a more circular orbit, like asteroidal dust, will spiral inwards to the Sun on a time scale of some 10000 years due to the Pointing-Robertson drag (Robertson, 1937; Wyatt and Whipple, 1950; Dohnanyi, 1978). Two simple explanations for this relativistic effect can be given — according to the chosen reference system (cf. Klačka, 1992, 1993a, 1993b). From the point of view of an observer traveling with the dust particle the direction of the radiation pressure does not coincide with the gravitational force but has a decelerating component. In the reference system of the Sun the dust particle emits radiation anisotropically, with the higher energetic radiation in flight direction, and therefore loses kinetic energy.

2.2 Stratospheric dust particles

Earth's gravitational field can capture passing dust particles and they eventually enter the atmosphere (Öpik, 1951). The mass distribution of the accreted dust peaks near 220 µm sized particles ($\sim 1.5\times10^{-8}$ kg), resulting in an accretion rate of $(40 \pm 20)\times10^{6}$ kg per year for particle sizes between 10 µm and 400 µm, which is at least as much as the average contribution from extraterrestrial bodies in the 1 cm to 10 km size range (Love and Brownlee, 1993).

The deceleration in the upper atmosphere causes friction heating that can even melt the particles. The chance of survival depends on several factors: entry velocity, entry angle, particle density and size. The more oblique the entry angle, and the smaller, less dense, and slower the particles are, the higher is their probability to reach the stratosphere intact or even unmodi-

fied (Love and Brownlee, 1991). Asteroidal particles normally have circular orbits, resulting in entry velocities slightly above 11.2 km/s. Cometary IDPs are on average faster than asteroidal, because they usually have highly eccentric, often even retrograde orbits. This decreases the probability of being captured by Earth (Flynn, 1990) and the probability to survive the entry. For example, an IDP with a diameter $\geq 10\,\mu m$ and a density of $2\,g/cm^3$ that enters under an angle $< 45°$ with a velocity $> 15\,km/s$ would be heated above 1200 K (Love and Brownlee, 1994). Considering these selection effects, the cometary contribution to the extraterrestrial component of the stratospheric dust was estimated to be less than 5 % (Kortenkamp and Dermott, 1995).

In the interplanetary dust cloud at 1 AU only few particles with radii of 1–1000 µm occur within $1\,km^3$ (Leinert and Grün, 1990). Atmospheric settling for 10 µm sized particles takes several weeks (Wilson and Huang, 1979; Mackinnon *et al.*, 1984). Only this enables a collection of interplanetary dust in the stratosphere with reasonable rates: Their reduced velocity in the stratosphere results in a drastic increase of their number density being now on the order of $10^6\,km^{-3}$ (Brownlee *et al.*, 1977). Since only few terrestrial and anthropogenic dust particle with sizes $\gtrsim 10\,\mu m$ occur in the stratosphere, the extraterrestrial component of the stratospheric particles becomes significant.

The opposite applies to the troposphere (altitudes $\lesssim 12\,km$) and the surface boundary layer ($< 100\,m$) where terrestrial dust prevails. Here, only in the Arctic and Antarctic ice fields and deep see sediments extraterrestrial particles can be identified, extracted, and analyzed (Maurette *et al.*, 1994). These so-called micrometeorites are typically larger than 50 µm. They are often severely altered, not only by atmospheric entry heating, but also from the residence in the ice that may last several thousands of years (*ibidem*).

Stratospheric dust particles are regularly sampled by NASA aircraft since 1981. Silicone oil coated collectors with $30\,cm^2$ or $300\,cm^2$ area are exposed to the airflow at a height of $\sim 20\,km$. The collectors are hermetically protected during start and landing to prevent contamination. Total flight times of 20–80 h are needed to gather reasonable numbers of particles, ~ 1 per hour. Therefore, the sampling must be spread over several flights. The collection and curating technique is reviewed by Warren and Zolensky (1994) and will also be explained in some detail in Chapter 4. Most collected particles have diameters greater than 2 µm. Smaller particles follow the air stream (relative velocity: 200 m/s) around the collector flags (Brownlee *et al.*, 1977). Only few collected particles are larger than 60 µm, because their shorter settling times make a capture increasingly unlikely. About 50 % of the collected stratospheric dust is of extraterrestrial origin, sometimes called *cosmic* dust. The other particles are re-entering space debris and remnants from space

launches or air-traffic (*e.g.*, paint particles or solid rocket exhaust), volcanic ashes, or even pollen (Stadermann, 1990).

2.3 Identification of IDPs

The next question is how to discern the extraterrestrial dust from the terrestrial particles. Adequate criteria must be found that are indicative of their origin.

The particles are hit by solar particulate radiation during their residence in the interplanetary dust cloud: solar wind and solar flares. Solar wind implanted He was detected within a 0.5 µm thick surface layer, having the same saturation concentration than in lunar soil (Rajan *et al.*, 1977). Other noble gases are also found enriched relative to terrestrial abundances, indicating again solar wind implantation (Hudson *et al.*, 1981). High energetic ions occurring in solar flares produce fission tracks in the crystal structure of IDPs. Their densities lead to space exposure ages of $\sim 10^4$ a (Bradley *et al.*, 1984) — in agreement with the calculated lifetimes of dust particles (Dohnanyi, 1978). Deviations of the oxygen isotope ratios relative to terrestrial values were also found for several IDPs (McKeegan *et al.*, 1986; Stadermann, 1990).

Another clue to the extraterrestrial origin arises from the particle's (major) element abundances. The majority of the identified IDPs has a chemical composition similar to carbonaceous chondrites of type CI (Brownlee *et al.*, 1976a; Ganapathy and Brownlee, 1979). These primitive meteorites reflect the overall composition of the solar system for all condensable elements: Their abundances match the composition of the solar photosphere (Anders and Grevesse, 1989). These *cosmic* or *chondritic* element abundances cannot be found in planetary material, because the planets differentiated during their formation into a core consisting of siderophile elements (*e.g.*, Fe, Ni, S) and into mantle and crust that are dominated by silicates and contain the lithophile elements (*e.g.*, O, Mg, Si).

CI abundances are not a necessary property of IDPs. Some particles that have a distinct composition are found with minor amounts of adherent chondritic material. They are also considered to be IDPs. One subgroup consists of $\gtrsim 3$ µm sized grains and is referred to as *coarse-grained* particles. Among them are the *mafic* IDPs, dominated by Mg-rich olivine and pyroxene (Brownlee *et al.*, 1976a; Esat *et al.*, 1979). Fe,Ni,S-rich *FSN* particles represent an other type of non-chondritic IDPs (Brownlee *et al.*, 1976a). They occur in various shapes: solid irregular masses, aggregates, or well-defined single crystals.

2.4 Characterization of chondritic IDPs

The particle type that most probably is of extraterrestrial origin are chondritic IDPs. They show a great variety in shape, density, grain sizes, and occurring mineral phases. Several subgroups of particles with similar properties are discerned. The basis for classification is the conjecture, that members of such groups have a similar history and/or origin.

Morphology. About 45 % of all stratospheric dust particles have a spherical shape (Mackinnon *et al.*, 1982). Some have a chondritic composition indicating either molten IDPs or ablation of (micro)meteorites. Other chondritic IDPs can be roughly divided into *chondritic porous* (CP) and *chondritic smooth* (CS) particles. The CP particles are fluffy agglomerates of $\lesssim 1\,\mu m$ sized grains, whereas the compact CS particles tend to consist of larger grains.

Mineralogy. The composition of individual IDPs is usually dominated by members of just one mineral group (cf. Fig. 2.1). In case of the CP IDPs, the anhydrous silicates olivine and pyroxene prevail. Several other mineral phases are found in smaller amounts, *e.g.*, glass, a carbonaceous phase, and *unequilibrated aggregates* (UAs). The UAs are agglomerates of $< 50\,nm$ sized, rounded crystals embedded in a carbonaceous matrix (Bradley *et al.*, 1988; Rietmeijer, 1989). The UAs are also called GEMS for *glass with embedded metal and sulfur* and possess chondritic bulk compositions (Bradley, 1994b). Anhydrous IDPs have an average C abundance of $1.7 \times$ CI (5.9 wt%), in rare cases up to 45 wt% (Thomas *et al.*, 1993, 1994). This high carbon content is comparable with in situ measurements of dust particles from comet P/Halley (Jessberger *et al.*, 1988). Based on their pristine mineralogy and infra red spectra, these IDPs bear the highest resemblance to comets (Bradley, 1994a).

The CS IDPs are rich in phyllosilicates that incorporate water. The majority of these hydrated minerals belong to the smectite group, *e.g.*, saponite; rarely particles are found with serpentine as the main phase (cf. Fig. 2.1). The UAs and the carbonaceous phase found in anhydrous IDPs are sometimes also observed in the smectite subgroup. The occurrence of phyllosilicates in CS IDPs indicates an aqueous alteration of the parent body. Despite this superficial resemblance to carbonaceous chondrites, only the smectite particles have comparable textural and mineralogical characteristics (Bradley *et al.*, 1988). This discrepancy can be explained, if serpentine IDPs and chondrites sample different parent asteroids. Reflectance spectra analysis indicate that some CS IDPs might be associated with the outer type P and D asteroids, whereas the presumed parent bodies of the CI and CM meteorites are type C asteroids from the main belt (Bradley, 1994a).

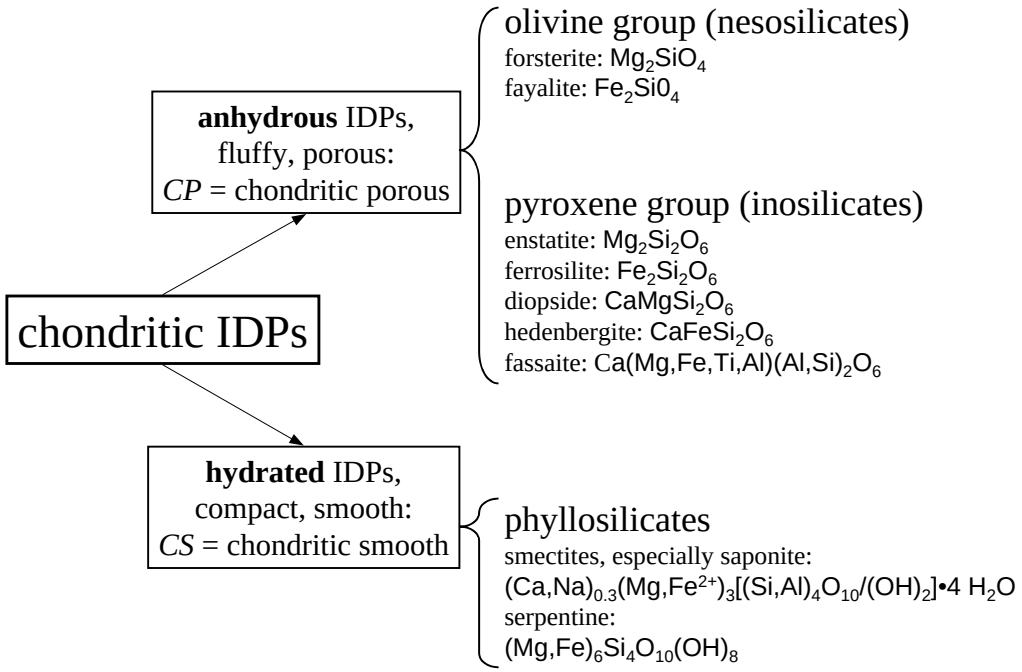

Figure 2.1: Overview of the basic characteristics of chondritic IDPs including the prevailing minerals. The exemplary given end members of a mineral group actually form solid solutions.

Figure 2.1 gives the basic properties of nonspherical chondritic IDPs, *i.e.*, anhydrous or CP particles and hydrated or CS particles. It also provides the chemical formulas for the main minerals of the respective type.

Bulk element concentrations. The bulk element abundances in individual chondritic IDPs are not entirely identical to the CI composition. Variations within a factor of two are tolerated for most elements to be classified as chondritic.

The average composition of chondritic IDPs shows several deviations from the CI abundances (cf. Schramm *et al.*, 1989; Arndt *et al.*, 1996). Refractory Ca and volatile S are found significantly depleted on average. Enrichments of Fe-normalized mean concentrations relative to CI abundances are observed for several rare and volatile elements: Cl, Cu, Zn, Ga, Se, and Rb amount to $\sim 1.7 \times$ CI.

The CI concentration of the halogens F, Cl, and Br is only 60.7 ppm, 704 ppm, and 3.57 ppm, respectively (Anders and Grevesse, 1989). For F an average enrichment in chondritic IDPs was not discovered up to now. But one has to keep in mind, that only little data is available for F, because

it cannot be measured with proton induced X-ray emission analysis (PIXE) and synchrotron X-ray fluorescence analysis (SXRF), which are the two most commonly applied techniques to measure trace element abundances in IDPs. Chondritic IDPs seem to be enriched in Cl to $\sim 1.7 \times$ CI on average (Arndt *et al.*, 1996b). Br is enriched to $21 \times$ CI on average in chondritic IDPs. F and Cl can be incorporated in a many different minerals, *e.g.*, phyllosilicates and apatite. For Br a specific host phases is still unknown. It can be assumed that traces of Br occur in most minerals, thus accounting for the overall content. However, Flynn and Sutton observed Br to be concentrated in a yet unidentified phase inside one IDP (Sutton *et al.*, 2000).

How can the deviations be explained? IDPs could have lost S during the atmospheric entry, if they were heated to temperatures around 800°C (Fraundorf *et al.*, 1982). Results from solar flare track analysis indicate, that most IDPs did not experience pulse heating above the annealing temperature of 600°C (Bradley *et al.*, 1984). Therefore it was concluded, that the volatilization of S during aerobreaking is not fully responsible for its depletion (Schramm *et al.*, 1989).

Selection effects can also result in depletion or enrichment (Schramm *et al.*, 1989; Arndt *et al.*, 1996b; Stephan *et al.*, 1997), here exemplarily explained for Ca: A heterogeneous distribution of this element in an IDP parent body will entail the concentration of Ca in a special type of interplanetary dust. If these Ca-rich IDPs occur among the other stratospheric particles, they might not yet be recognized as extraterrestrial, *i.e.*, a selection effect is caused by the disability to identify them. Also, the Ca-rich particles could have properties preventing them from being sampled or analyzed at all: They might be bigger or more fragile on average than other IDPs, so that they would be destroyed at atmospheric entry or during preparation more frequently than the 'typical' chondritic IDP. Selection effects can possibly account for all mean deviation from CI abundances except for Br (Stephan *et al.*, 1997).

The mean enrichment of some volatile elements may be explained by postulating a new class of primitive solar system material (Flynn and Sutton, 1992; Flynn, 1994): In the same way that the CM carbonaceous chondrites, the second primitive meteorites after CI, are depleted in their volatile element concentration relative to CI, the IDPs would represent a type of chondritic material even more primitive which is volatile rich. This explanation bears the problem, that CI material is supposed to have the 'most primitive' composition, for it matches the composition of the Sun's photosphere including volatile elements (Anders and Grevesse, 1989) and should therefore represent the mean solar system composition.

Eventually, another explanation for the enrichments might be alteration of the IDPs on Earth. Jessberger *et al.* (1992) suggested that at deceleration or during residence in atmosphere secondary processes affect their composition. Especially the distinct Br enrichment can easily be explained by halogen bearing aerosol droplets contaminating the IDPs. By now, this assertion is supported by the observation of a Br contamination of test particles flown on a collector in the stratosphere (Arndt *et al.*, 1996a; Arndt, 1997), surface bound Br-salt nanocrystals on IDP W7029E5 (Rietmeijer, 1993), a halogen rich rim of IDP L2006G1 (Stephan *et al.*, 1994c), weakly bound Br in several large IDPs (Flynn *et al.*, 1996), and halogen rich surface layers on aluminum oxide spheres sampled in the stratosphere (Rost *et al.*, 1999).

Possible groupings. IDPs from different parent bodies are expected to show deviations of their mean composition and its variation range. This could define groups discernible from others, which would allow to identify them. For this purpose the individual element abundances, not only for the major but also for the rare and trace elements, must be known for a great number of particles.

The analysis of the small, only $\sim 20\,\mu m$ sized, IDPs require highly developed techniques, *e.g.*, SXRF (Antz *et al.*, 1987; Sutton and Flynn, 1988; Flynn and Sutton, 1990, 1991), PIXE (Jessberger and Wallenwein, 1986; Wallenwein *et al.*, 1987, 1989; Bohsung *et al.*, 1995), and secondary ion mass spectrometry (SIMS) (Stadermann, 1990). Some analyses entail a (partial) destruction of the particle, *e.g.*, SIMS measurements. The existing data base of individual IDP compositions is rather incomplete, since no method can provide the abundances of all elements (Arndt *et al.*, 1996b).

Schramm *et al.* (1989) first used morphological criteria and distinguished three different subgroups of smooth, porous, and coarse particles. Since only major elements were measured, the observed variation in their mean composition might be just a result of their different mineralogy. However, Ca is distinctly less depleted in porous than in smooth particles. Arndt *et al.* (1996) performed a comprehensive statistical evaluation of all available bulk compositions including trace elements. They identified mathematically defined, chemically distinct subgroups that had already been proposed previously, mainly based on Ni and Zn concentrations of a smaller number of particles (Flynn and Sutton, 1990, 1992). However, it was not possible to relate the subgroups with particular parent bodies.

More comprehensive studies on individual IDPs are needed to scrutinize the significance of any grouping. An attempt in this direction is the analysis of *cluster* IDPs. Here several particle fragments were found on the collector spatially correlated indicating a common precursor particle. Altogether these fragments provide more material and thus allow the application of a broader

range of analytical methods (Thomas *et al.*, 1995). However, the individual fragments proved to be too different to represent the whole particle. Brownlee *et al.* (1993, 1994) were able to combine scanning electron microscopy (SEM), TEM, spectral reflectance analysis, and thermally stepped He release measurements on individual particles. In some cases they were able to relate indications of the particle's origin with a chemical-mineralogical characterization of the IDP.

The Collector Project. A similar approach represents the *Collector Project* (Stephan *et al.*, 1994a), to which this work is contributing. Several analytical techniques are successively applied to individual stratospheric dust particles. The sequence of measurements is optimized to allow the subsequent analyses. A preclassification according to the major element concentrations is achieved by SEM analyses. PIXE provides major and trace element abundances for the whole particle, as well as their distribution on a micrometer scale. TOF-SIMS enables the analysis of IDP surfaces, as well as sections with a submicrometer resolution. TEM studies yield the mineralogical characterization. A detailed description of the project implementation is given in Chapter 4.

Combined results on each IDP will help not only to establish any grouping of IDPs according to some of their properties, but also to relate these groups with possible parent bodies. The identification of cometary IDPs is most important in this context.

TOF-SIMS cannot provide unambiguous identifications of minerals or determination of absolute element concentrations with high accuracy. These are the tasks of TEM and PIXE, respectively. However, TOF-SIMS measurements reveal the distribution of most elements and can be used to find conspicuous mineral phases that will be further characterized with TEM. Some of these phases may be helpful to determine the particle's origin.

The main advantage of TOF-SIMS is its surface sensitivity: only the upper monolayers are analyzed. Therefore, TOF-SIMS analyses also address the question of possible contamination processes during the atmospheric residence of the particles. The very surfaces of IDPs are inspected for contaminants. Especially the controversially discussed origin of the Br (and other halogens) enrichment should be settled. Analyzing sections from the same particles helps to corroborate the findings of the surface inspection. The particles selected for this study are not only cosmic particles. Also probably terrestrial dust particles were chosen, because stratospheric contamination processes would affect all types of particles.

Chapter 3

TOF-SIMS

3.1 Introduction

Microanalytical techniques require a high efficiency to conclude physical and chemical properties from a small sample volume. The elemental composition is ideally derived by identifying all atoms of a sample and counting them. Mass spectrometry follows this concept by disintegrating sample material into ionized atoms and separating them according to their mass (and charge). There is a variety of realizations that differ in the involved ion formation process and the method of ion separation.

In secondary ion mass spectrometry (SIMS) high energetic primary ions impinge on the sample surface, resulting in a cloud of molecules, clusters, and atoms that is partly ionized. Typically, a quadrupole or a double focusing (DF) sector field spectrometer separates the ions according to their mass to charge ratio.

Time-of-flight secondary ion mass spectrometry (TOF-SIMS) takes advantage of the differing drift times of secondary ions that were accelerated in the same electric field. They are produced by a short primary ion pulse and then pass an electrostatic extraction field that accelerates them. All equally charged ions gain the same kinetic energy. Ions having the same ionization state but different masses will therefore obtain distinctive drift velocities after acceleration. Consequently, the drift times required to reach the detector are related with the mass to charge ratio of the ions. The respective equations read as follows:

$$q\,e\,U_{Ex} = E_{pot} = E_{kin} = \tfrac{1}{2}\,m\,v^2 = \tfrac{1}{2}\,m\,(d/t_d)^2 \tag{3.1}$$

$$\Rightarrow m = 2\,q\,e\,U_{Ex}\,t_d^2/d^2 \tag{3.2}$$

$$\text{or :} \qquad m \propto q\,t_d^2, \qquad t_d \propto (m/q)^{1/2} \tag{3.3}$$

Here U_{Ex} is the extraction voltage, q the ionization state of the particle (1, 2, ...), e the elementary charge, d the drift distance, and t_d the measured drift time of ions with mass m.

Several thousands of individual time-of-flight spectra must be added up to result in a sum or *total spectrum* of sufficient counts. In praxis, Equation 3.2 does not allow to relate drift times with masses: U_{Ex} and d are constant, but not known with the necessary accuracy. Furthermore, the measurement of t_d requires the exact starting time ($t_d = 0$), which is difficult to derive. A better conversion of the flight time into mass is achieved by simply using the proportionality between m and t_d (Eq. 3.3): A manual identification of at least two or more peaks with the corresponding ion species enables the calculation of the constant of proportionality that establishes the calibration. Ions with $q = \pm 1$ dominate the spectra, independent of their ionization state in the sample. Therefore, it is convenient to use the mass scale derived from singly charged ions instead of the time-of-flight scale.

One discriminates between *static* and *dynamic* SIMS. Static conditions are given, when the sample properties remain undisturbed by the measurement, whereas they are altered by the sputtering process in dynamic SIMS. The latter normally applies to DF-SIMS with its high current densities up to $1\,\mathrm{A/cm^2}$, resulting in a high sample consumption of about 1000 monolayers/second (Benninghoven *et al.*, 1987). This is necessary to compensate the low overall *transmission*, *i.e.*, the quotient of particles reaching the detector and particles entering the mass analyzer. Therefore, the actual chemical and physical properties of the analyzed sample surface are strongly influenced by the measurement itself and may change during the analysis if the sample's composition is inhomogeneous.

The TOF analyzer allows almost static conditions for two reasons. First, the mass spectra consist of all secondary ions with the same polarity including molecules. The high transmission of 20–80 % enables sufficient count rates with low primary ion current densities. Second, TOF-SIMS requires a pulsed operation of the primary ion beam for the determination of drift times. The shorter the pulses the higher is the mass resolution. Therefore, TOF-SIMS entails very low sample consumption: only the uppermost monolayers are affected and analyzed.

3.2 The Münster TOF-SIMS instrument

This study made use of the Cameca/ION-TOF TOF-SIMS IV instrument at the *Institut für Planetologie*, Münster. Starting as TOF-SIMS III in Heidelberg it was improved over the years to catch up with most of the state-

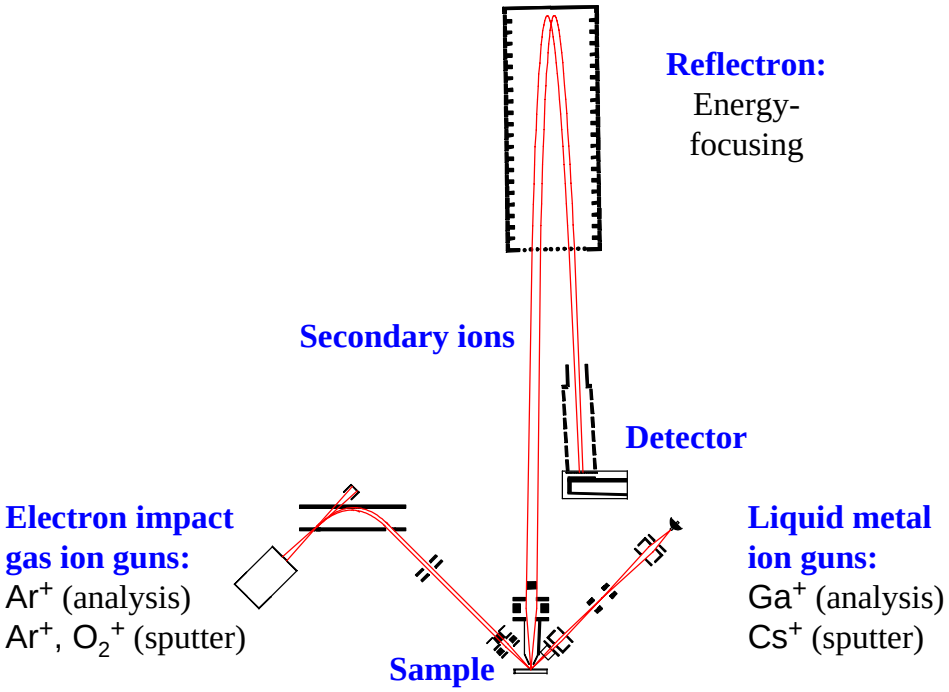

Figure 3.1: Sketch of a typical ION-TOF instrument. In fact, the Ar^+ and Ga^+ analysis guns are individually mounted, whereas the two sputter guns are combined in a way that they share the final focusing elements.

of-the-art possibilities Cameca/ION-TOF offers. This implied that not for all measurements all current features were already available. For a detailed description of the TOF-SIMS version III see Schwieters *et al.* (1990), a summary of the present-day technology can be found in Niehuis *et al.* (1998) and Stephan *et al.* (1999). Figure 3.1 shows a sketch of the presently installed instrument. It is equipped with two primary ion guns, two sputter guns, an electron flood gun for charge compensation, a TOF mass analyzer with detector system, and a secondary electron detector.

ION-TOF instruments offer the possibility of imaging, *i.e.*, measuring the lateral variation in the composition of the sample. In contrast to a camera, the surface information is not projected on the detector plane, but the pulsed primary ion beam successively scans over the area of interest. The lateral resolution of the resulting secondary ion distribution images depends on the quality of the primary ion focusing in the target plane.

Primary ion guns. Our system is equipped with two primary ion guns. The Ar electron impact gas ionization gun enables rather short primary ion pulses (~ 800 ps) that contain ~ 500 ions with an energy of 10 keV. But since

the Ar gun offers only a lateral resolution of 10 µm, it is not suitable to analyze particles of equal size as, *e.g.*, the stratospheric dust particles.

The ^{69}Ga liquid metal ion source is employed in the other primary ion gun. It operates with an acceleration voltages up to 25 keV. Several operating modes are available addressing different foci of interest: Since the positive ions in the primary ion pulse are repelling each other, it is not possible to optimize at the same time the secondary ion intensity (proportional to the number of primary ions per pulse), the mass resolution (depending on the length of the primary ion package), and the lateral resolution (proportional to its diameter).

The *normal* mode offers the highest lateral resolution. Under optimum conditions, *i.e.*, conductive samples, a resolution of 0.2 µm can be achieved. Pulse lengths ≥ 5 ns are accessible by means of a *blanker*. This capacitor deflects the continuous primary ion beam periodically, which results in one pulse every 100 µs. With this cycle time 10000 individual TOF spectra are acquired in one second and the mass spectrum covers a range up to approximately 800 u. Pulses of 5 ns (50 primary ions per pulse) result in fairly high secondary ion intensities, but allow only the separation of hydrocarbons from other molecules (*e.g.*, element-oxides and -hydrides) and elements with the same nominal mass. The available other modes increase the mass resolution at the expense of either lateral resolution or intensity.

The *bunched* mode makes use of a capacitor field that accelerates the rear ions of an ion package more than the front ions, so that they reach the target surface almost simultaneously. The hereby achieved pulse length of ~ 600 ps is sufficient for separating most elements, oxides, and hydrides in the secondary ion mass spectrum. This mode preserves the number of primary ions per pulse, so that the same count rates as in the normal mode are obtained. However, the primary ion packages broaden out. The resulting lateral resolution of 5 µm does not meet the requirements of IDP analysis.

The *chopped* mode is the suitable mode for this study, because it combines maximum lateral resolution with a reasonable good mass resolution. The primary ion beam is deflected in a periodic electric field (*chopper*). This sine shaped oscillation has a step-wise adjustable frequency up to 40 MHz. Only at zero-crossing a short primary ion package can pass the aperture. This results in a maximum pulse frequency of 80 Mhz, *i.e.*, one pulse every 12.5 ns. Each pulse has a length of $\lesssim 1.5$ ns. The supplementary operation of the blanker causes that just one of them occurs in each cycle. The disadvantage of this mode lies in the low secondary ion count rates due to the small number of ~ 10 primary ions per pulse.

The *burst* mode is a variation of the chopped mode with the blanker being adjusted to let pass several pulses within one cycle. Since its starting

time triggers the acquisition of an individual TOF (*i.e.*, mass) spectrum, several spectra are superposed with a constant time offset, resulting from the multiple primary ion pulses per cycle. Several separated peaks are now detected for the same secondary ion species, thus increasing the count rate of this ion by a factor equal to the number of pulses per cycle. According to Eq. 3.3, the arrival time differences between higher masses decrease, so that the superposed spectra finally intermingle, *e.g.*, at 50 u for 10 burst pulses. Since for the IDP study one is interested in all measurable elements, especially up to 81 u, in order to detect ^{81}Br, the burst mode is not applied.

Electron flood gun. Insulating samples like most minerals cause charging problems: The positive charge of the implanted primary ions affects the extraction field and thus reduces the secondary ion yields drastically. The electron flood gun (Hagenhoff *et al.*, 1989) provides low energy electrons (10–20 eV) between successive primary ion pulses to compensate positive charging.

Sputter guns. The Münster TOF-SIMS IV is equipped with two sputter guns that can be applied additionally to the primary ion gun: One electron impact gas ionization gun, which can be operated with O_2 or Ar, and a Cs liquid metal ion source. Their main purpose is the explicit removal of sample material. This allows depth-profiling and the fast cleaning of contaminated surfaces. They provide much higher ion currents than the primary ion gun: up to some 10 nA. One of them can be employed in the spare time after primary ions hit the target and secondary ions are drifting to the detector (*quasi-parallel sputtering*). The application of a sputter gun has an advantageous side effect: The resulting implantation of oxidizing O or reducing Cs increases the secondary ion yields of positive (Benninghoven and Mueller, 1972) or negative secondary ions (Storms *et al.*, 1977), respectively. Since this effect depends on the O and Cs concentration in the uppermost surface layers, the energy of the impinging sputter ions is set to 3000 kV. This is distinctly lower than for primary ions, thus reducing the penetration depth of the sputter ions.

The conditions for static SIMS are no longer fulfilled when quasi-parallel sputtering is applied, because the original surface composition and structure are altered. The usage of O_2^+ not only increases the intensities of metal ions but produces also high metal-oxide peaks (Fig. 3.2). Concerning the chopped mode used in this study, the mass resolution is not sufficient to discriminate them from the metal ions, *e.g.*, MgO, CaO, TiO from Ca, Fe, Zn. In the normal field of TOF-SIMS application, *i.e.*, semiconductor technology, this is not a disadvantage, because the samples of interest consist of just a few elements. However, in planetology multielement samples prevail, especially with at first unknown composition. Therefore, exact peak identification is

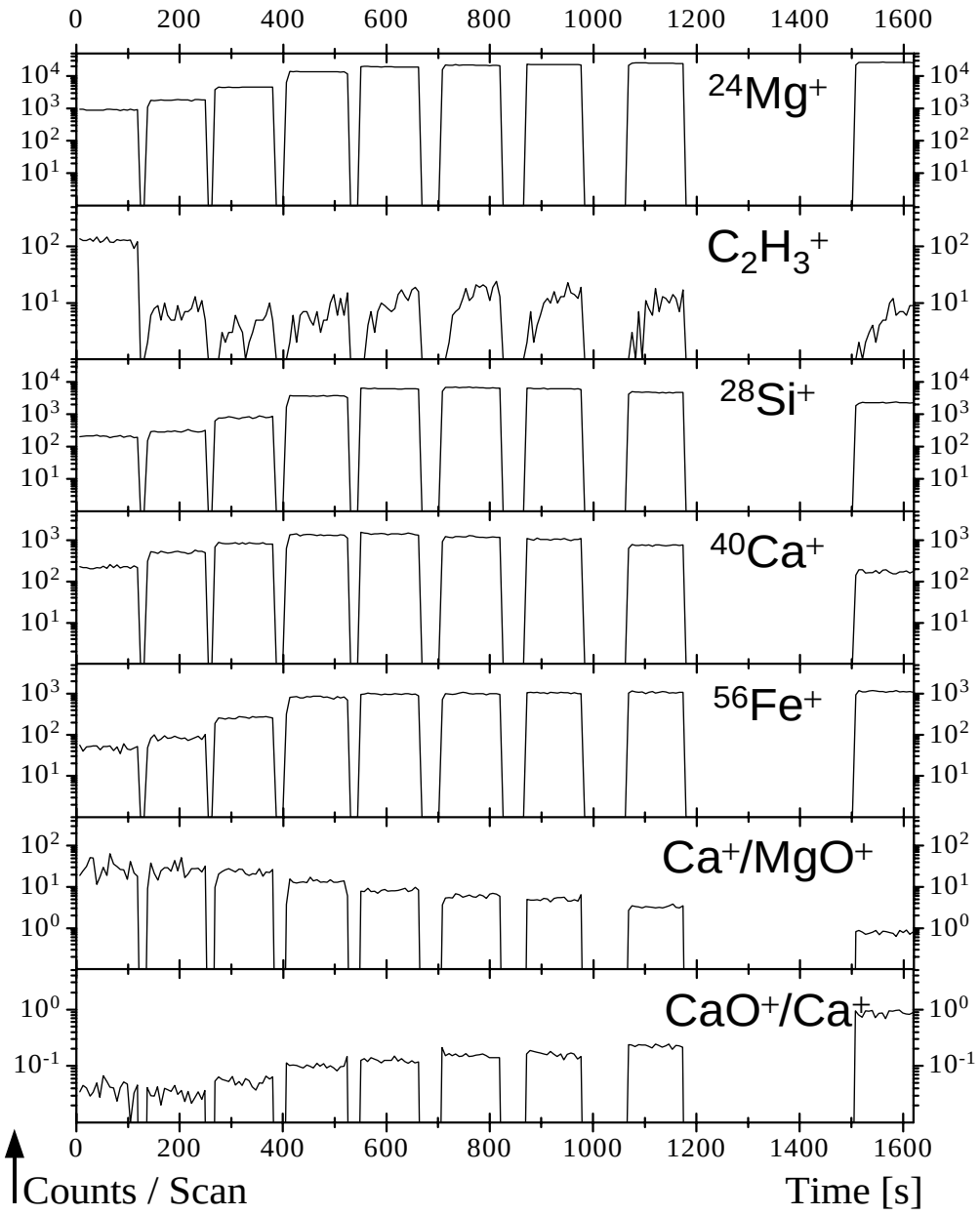

Figure 3.2: Secondary ion count rates are influenced by O_2^+-sputtering that was applied during the gaps. Each data point sums up the counts within a scan of 65536 primary ion shots. Count rates from elemental ions ($^{24}Mg^+$, $^{28}Si^+$, $^{40}Ca^+$, $^{56}Fe^+$) are increasing. The surface contaminant $C_2H_3^+$ is reduced after the first sputter interval. Oxide ions are increasing, even with respect to the corresponding element ($^{40}Ca^{16}O^+/^{40}Ca^+$). Their enhancement may interfere with the measurement of an element having the same nominal mass ($^{40}Ca^+/^{24}Mg^{16}O^+$). (Sample: San Carlos olivine)

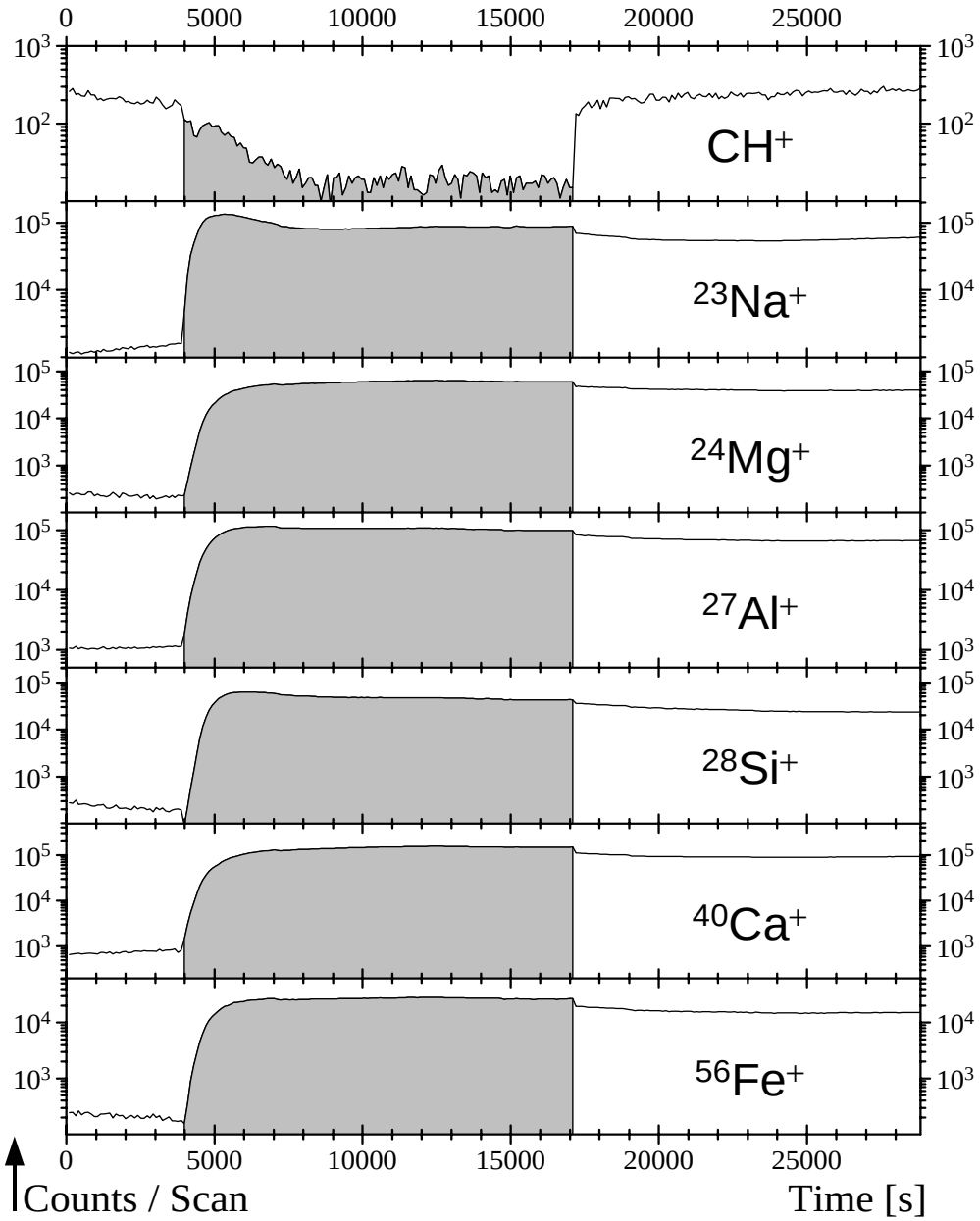

Figure 3.3: Secondary ion count rates are influenced by quasi-parallel Ar^+-sputtering, which was applied during the middle part (gray). Each data point sums up the counts within a scan of 1048546 primary ion shots. Count rates from elemental ions ($^{23}Na^+$, $^{24}Mg^+$, $^{27}Al^+$, $^{28}Si^+$, $^{40}Ca^+$, $^{56}Fe^+$) are enhanced by a factor of ~ 100 during quasi-parallel sputtering. After sputtering they slightly decrease by $\sim 50\,\%$. Surface contaminating CH^+ ions are suppressed throughout the sputtering, but emerge again with their original count rate afterwards. (Sample: glass standard)

imperative. The problem of increasing oxide interference can be avoided if the gas ionization sputter gun is operated with inert Ar (instead of O_2).

The intention for all analyses within the Collector Project is to minimize sample destruction. For the measurement of IDPs the sputter ion current was restricted to 100 pA, which is still 2000 times as much as the primary ion current in normal mode, but with the effective sputter area always chosen to be four times the analyzed area. The resulting primary ion current density is low enough to enable charge compensation as needed for insulating samples.

The technique of quasi-parallel Ar-sputtering (Fig. 3.3) has some distinct advantages. First, the omnipresent surface contamination layer of adherent gas molecules and hydrocarbons, which hampers the analysis, is removed about ten times faster. Moreover, fresh covering is effectively prevented throughout the quasi-parallel sputtering (cf. CH^+ in Fig. 3.3). But most importantly, Ar-sputtering significantly enhances the yields of elemental secondary ions up to about 100 times for, *e.g.*, Mg, Al, Si. This is comparable with the positive impact of quasi-parallel O-sputtering.

The exact reason for this effect is still unknown (cf. Chapter 3.3). A possible explanation is that the Ar-sputtering shortens the time needed to reach stable measurement conditions, *i.e.*, the removal of all contamination molecules adsorbed in the very surface region, and the reduction of surface related chemical bonds, which are not found inside the solid. This is plausible, because after some sputtering, and after stopping quasi-parallel sputtering at all, the secondary ion count rates form plateaus, whereas prior to any sputtering the count rates are increasing or decreasing, indicating that the measurement conditions are not in equilibrium. Moreover, the Ar^+ ions may effectively destroy chemical bonds in the upper monolayers, since their energy is with 3000 kV about eight times lower than the respective energy of the much deeper penetrating Ga^+ primary ions. The now less tightly bound atoms at the surface should be more susceptible for sputtering and ionization by Ga^+ primary ions. This conjecture is supported by the fact that the secondary ion intensities of the elements decrease by a factor of about two after stopping Ar-sputtering. Also, during Ar-sputtering hydrocarbons like CH^+ are apparently disintegrated (Fig. 3.3), but emerge again immediately after sputtering.

Mass analyzer and detector. An electric extraction field accelerates the secondary ions to an energy of $q \cdot 2$ keV (q is the ionization state, normally ± 1). On their way to the detector system, they must pass the *reflectron* (Mamyrin *et al.*, 1973) where they are reflected by an electric potential barrier. This device compensates the first order variation of the initial energy, which the secondary ions possess after leaving the solid state: The more energetic and hence faster ions penetrate deeper into the reflectron, resulting

in longer flight times than for the lower energetic ones. Right in front of the detector system, a post accelerator increases the particles energies up to $q \cdot 10\,\mathrm{keV}$. Only by this the slower heavy ions produce a sufficient electron response when hitting the detector's channelplate. A scintillator converts the electrons into photons, which leave the ultra high vacuum system through a glass plate and are finally detected with a photomultiplier outside. This method was chosen to avoid problems arising from the high potential of the channelplate relative to the ground potential of the target. A time-to-digital converter discriminates the photomultiplier signals by time channels of 200 ps.

Data acquisition and analysis. ION-TOF/Cameca also provides some appropriate software for data acquisition and analysis. Normally all useful information is kept in a *raw* file. For each primary ion shot the current position of the primary ion beam and all measured secondary ion arrival times are stored. After the actual measurement, this file enables to generate spectra of arbitrary selected regions of interest or distribution images of self-defined time bins, typically chosen to contain just one ions species.

The data have to be corrected for the 40 ns dead time of the detector (Stephan *et al.*, 1994b), which means, for instance, that an early arriving elemental ion prevents the detection of any further ions of the same nominal mass within this cycle. From the number of counts detected in the 40 ns before a specific channel, one has to calculate how often it was actual 'active' or 'dead' on the average. Based on the Poisson statistics, the counts in this channel can now be replaced by the correct amount of ions arriving at the detector within the channel time. The correction is essential for quantification, since the dead-time effects are nonlinear and would distort the results of the corresponding evaluation (Chapter 3.4).

Secondary ion distribution images also have to be shift corrected. The experimental conditions are not absolutely stable during hours of measuring. Therefore, the analyzed field of view can shift slightly in the range of micrometers. Since the resulting image typically consist of 100 or more scans, any feature in the sample blurs according to this shift. With the supplied software, it is possible to compensate the shift for each scan after the measurement, in many cases even automatically: one small feature in the distribution of an ion species, which must be present in all scans, is used to determine the x- and y-offset for each scan. With this set of parameters, a corrected sum image can be calculated.

The distribution images are obtained with pixel resolutions of $(2^n \cdot 64)^2$, $n = 0, 1, 2, 3, 4, 5$. According to the lateral resolution and the size of the sample area to be analyzed, useful selections are 128×128 and 256×256. Every 4096 shots the measurement is automatically halted to transfer data

from the time-to-digital converter to the computer. Artifacts emerge if this happens within a line scan, because the primary ion beam is at first slightly mispositioned when the acquisition continues. This can be avoided if the data transfer coincides with the end of a line scan. Since high secondary ion yields per scan are advantageous for the shift correction only two sensible combinations remain: either 16 primary ion shots per pixel in the 256×256 mode or 32 shots per pixel in the 128×128 mode. For one scan of this type 105 s or 52 s are required, respectively.

3.3 Sputtering and emission of secondary ions

The physics of the sputtering and ionization processes are not entirely understood, especially not quantitatively. It is not possible to calculate from first principles, *e.g.*, sputter rates and secondary ion yields per solid angle for arbitrary samples only on the basis of the experimental conditions. Nevertheless, the importance of some parameters is known (cf. Benninghoven *et al.*, 1987):

- the residual gas in the analysis chamber
- the properties of the primary ion (mass, ionization state, kinetic energy, electronegativity, first ionization potential)
- the properties of the target material (*matrix effect*): element abundances, mineral phase, orientation of crystal axes, if not amorphous
- the geometry: angle of primary ion incidence and position of the secondary ion detector

Normally, it can be ensured that the properties of the residual gas and of the primary ions are identical throughout all measurements. The nature of the target material, however, is varying from sample to sample and also within a given sample. In addition, the geometrical factors become important, despite constant instrumental conditions, if the sample possesses an irregular surface morphology.

Some models successfully predict some quantities if special conditions are realized, *e.g.*, a target of just pure metal or polycrystalline material. They are usually based upon the collision cascade model by P. Sigmund (1969, 1972). This model describes how the primary ions first lose their energy through several binary collisions while penetrating into the target. Later,

after their kinetic energies have decreased to some 10 eV, they interact with many atoms of the lattice simultaneously and their energy is dissipated into lattice vibrations, *i.e.*, heat. Although some of the first collision partners or even a backscattered primary ion might leave the target, most sputtered particles are a result of a collision cascade, which originated from the initial collision partners. It transports a minor fraction of the primary ion energy and momentum back to the surface region. Here, from the uppermost monolayer(s), the majority of secondary atoms, radicals and molecules are desorbed. Only a minority of them ($<1\,\%$) is ionized. On the other hand, the typical penetration depth for 25 kV Ga and 10 kV Ar ions is on the order of 10 nm (Schiøtt, 1970; Benninghoven *et al.*, 1987) depending on the target material. The energy distribution of the emitted secondary particles has a maximum at the half of their surface binding energy, which is on the order of some eV (Oechsner, 1970a, 1970b). Concerning TOF analyzers, the variation in first order is compensated by means of a reflectron to allow a sufficient flight time separation (Mamyrin *et al.*, 1973).

Most important for the interpretation of the secondary ion distribution images from whole particles is the angular dependence of the yields. First, the yields increase for a non-perpendicular but oblique incidence, because more collisions occur right beneath the very target surface. This enhances the energy available for desorption. At even higher angles of incidence (ϑ, cf. Fig. 3.4 for definitions) more and more primary ions are reflected from the target surface, decreasing the deposited energy again. The resulting maximum is observed for $\vartheta \sim 65°$ (Firsov, 1970). In special cases semi-empiric models can reproduce these findings (Oechsner, 1973). The *total sputter yield* $Y(\vartheta)$, *i.e.*, the number of all sputtered particles divided by the number of primary ions, can be approximated for values of ϑ much smaller than the angle at maximum:

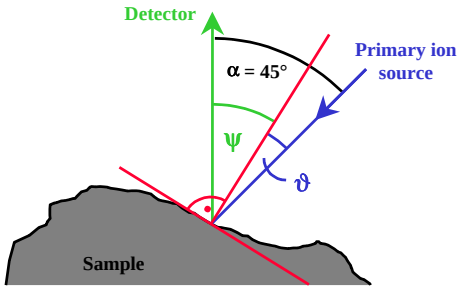

Figure 3.4: Definition of angles.

$$Y(\vartheta) \propto \cos^{-1}\vartheta \quad \text{for} \quad \vartheta \ll 65° \tag{3.4}$$

For just one ion species, the number of detected secondary ions is proportional to the total sputter yield if constant geometric conditions are maintained. This is normally fulfilled for flat targets and fixed positions of primary ion gun and detector. But if the relative position of detector and/or primary ion gun changes with respect to the (normal of the) sample surface, angle dependencies of secondary ion emission have to be considered. For small

ϑ and $\Delta\Omega$, which represents the solid angle of the detector, the following equation holds for the emission of secondary ions in the ionization state q (Hennequin, 1968):

$$\frac{\Delta Y^q(\psi,\vartheta)}{\Delta\Omega} = I_0 \underbrace{\frac{1-\lambda\cos\alpha}{1-\lambda}}_{\kappa} \frac{\cos\psi}{\cos\vartheta} \quad \text{for} \quad \vartheta \ll 65^\circ \tag{3.5}$$

Here ψ is the angle to the detector relative to the surface normal, and α the angle between detector direction and primary ion beam (Fig. 3.4). I_0 is the secondary ion yield for normal incidence and detector position, leading to $\vartheta = \psi = 0 \Rightarrow \alpha = 0$, $\kappa = 1$. λ is an ion specific correction factor modifying the simple symmetric $\cos\psi$-distribution. However, in the present experimental setup α is constant ($\sim 45^\circ$) causing also κ to be constant. But one has to keep in mind that ψ and ϑ themselves may actually vary if the target surface is rough or if small particles are analyzed. The remaining dependency reads as follows:

$$\frac{\Delta Y^q(\psi,\vartheta)}{\Delta\Omega} \propto \frac{\cos\psi}{\cos\vartheta} \quad \text{for} \quad \vartheta \ll 65^\circ \tag{3.6}$$

3.4 Quantification of element abundances

The influence of the angle dependencies can be neglected for flat surfaces like polished sections. Normally also all other instrumental parameters remain constant. But nevertheless, the sample properties still represent an important influence on secondary ion yields and must be considered for the calculation of element abundances. The ion emission depends on the crystal structure, crystal orientation, and the chemical environment — the so-called matrix effect. The relation between the actual abundance of an element and its secondary ion yield is not linear and can only be approximated locally.

To cope with the matrix effect one has to compare the results to measurements of standards with a composition that most closely matches that of the sample. However, even small differences in the matrix characteristics (*e.g.*, in composition or crystal orientation) or in the experimental conditions (*e.g.*, primary ion current, pressure and nature of the residual gas) can result in different secondary ion yields. Considering ratios of secondary ion yields, some variations of the overall count rate are compensated. The method of relative sensitivity factors allows further evaluation (McHugh and Stevens, 1972; McHugh, 1975). The following explanation is based on the formalism given by Benninghoven *et al.* (1987).

The evaluation of a (dead time corrected) spectrum results in the amount of ions $N^q(^A\mathsf{E})$ belonging to the nuclide of element E with mass number A in the ionization state q. Either positive or negative charged ions occur according to the polarity of the applied extraction field. Since the number of ions with $q = \pm 1$ greatly exceeds the ones in higher ionization states, the evaluation can be simplified by neglecting multiple charged ions, *i.e.*, considering only $N^{\pm}(^A\mathsf{E})$. By adding up the $N^{\pm}(^A\mathsf{E})$ of all isotopes one gets the sum of all arriving singly charged ions from element E: $N^{\pm}(\mathsf{E})$. If major isotopic anomalies are unlikely, $N^{\pm}(\mathsf{E})$ can also be calculated using the natural isotope ratios (Anders and Grevesse, 1989). For measurements of flat sample areas, the geometrical influence on ion emission and detection is invariable. Therefore, $N^{\pm}(\mathsf{E})$ is only proportional to the total number of emitted secondary ions from element E.

Supposing a homogeneous sample composition in the analyzed area, one can relate the secondary ion ratio with the ratio of atomic concentrations, $c(\mathsf{E})/c(\mathsf{R})$, by introducing the relative sensitivity factor $S^{\pm}_{\mathsf{R}}(\mathsf{E})$, which is, of course, also dependent on the reference element R:

$$\frac{N^{\pm}(\mathsf{E})}{N^{\pm}(\mathsf{R})} = S^{\pm}_{\mathsf{R}}(\mathsf{E}) \left[\frac{c(\mathsf{E})}{c(\mathsf{R})}\right] \tag{3.7}$$

This offers a means of quantifying the element abundances: one has to obtain the relative sensitivity factors of all elements by measuring $[N^{\pm}(\mathsf{E})/N^{\pm}(\mathsf{R})]_S$ from standards (marked by index S) with known composition $[c(\mathsf{E})/c(\mathsf{R})]_S$. Figure 3.5 shows the relative sensitivity factors $S^{\pm}_{\mathsf{R}}(\mathsf{E})$ with Si as reference element as derived from standard measurements at the *Institut für Planetologie*. Si was chosen, because it is abundant in most samples and forms positive, as well as negative secondary ions — only by this, the information from positive and negative secondary ion spectra can be combined.

$$S^{\pm}_{\mathsf{R}}(\mathsf{E}) = \left[\frac{N^{\pm}(\mathsf{E})}{N^{\pm}(\mathsf{R})}\right]_S \left[\frac{c(\mathsf{R})}{c(\mathsf{E})}\right]_S \tag{3.8}$$

Now it is possible to calculate the relative abundances $[c(\mathsf{E})/c(\mathsf{R})]$ of an unknown sample from the measured secondary ion ratios:

$$\left[\frac{c(\mathsf{E})}{c(\mathsf{R})}\right] = \frac{1}{S^{\pm}_{\mathsf{R}}(\mathsf{E})} \frac{N^{\pm}(\mathsf{E})}{N^{\pm}(\mathsf{R})} \tag{3.9}$$

Usually the goal is to obtain the element abundance in a sample, either in form of its concentration $C(\mathsf{E})$ (in wt%), or as atomic abundance $c(\mathsf{E}) = n(\mathsf{E})/n$ (in at%). $n(\mathsf{E})$ is the number of atoms E per volume and n the total

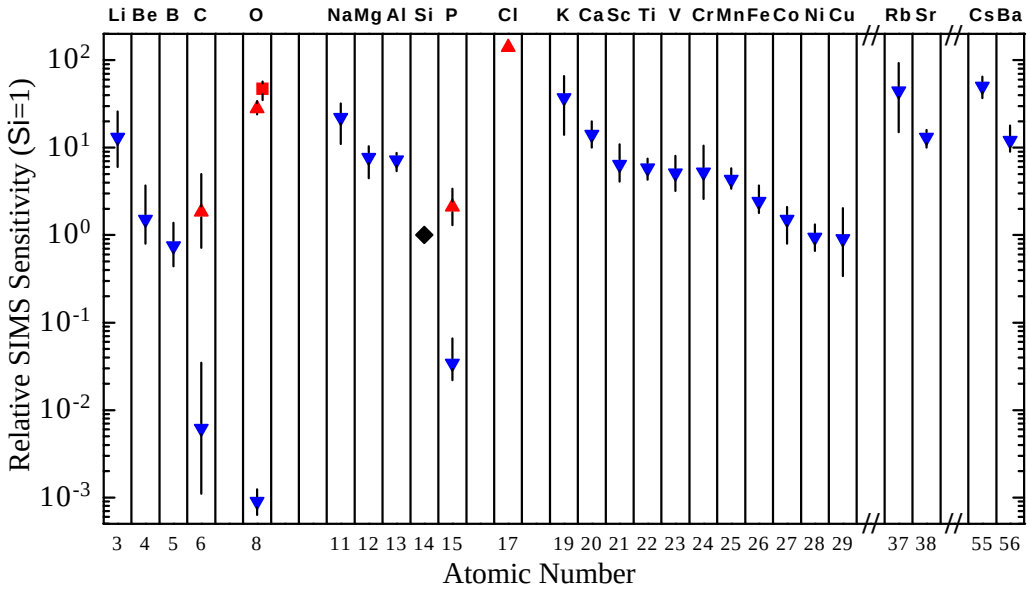

Figure 3.5: Mean TOF-SIMS sensitivity factors relative to Si obtained from glass standards with quasi-parallel Ar-sputtering. Blue ▼ and red ▲ indicate measurements of positive or negative secondary ions, respectively. The red ■ marks a distinct O sensitivity after sputtering, whereas the sensitivities of the other element remain valid. Additionally indicated is the range between the individual standards. (Stephan, 1999)

number of atoms per volume. $C(\mathsf{E})$ can be derived from $c(\mathsf{E})$, as well as from the normalized relative atomic abundances $[c(\mathsf{E})/c(\mathsf{R})] = n(\mathsf{E})/n(\mathsf{R})$:

$$C(\mathsf{E}) = \frac{n(\mathsf{E})\, m(\mathsf{E})}{\sum_{\mathsf{X}} n(\mathsf{X})\, m(\mathsf{X})} = \frac{c(\mathsf{E})\, m(\mathsf{E})}{\sum_{\mathsf{X}} c(\mathsf{X})\, m(\mathsf{X})} = \frac{m(\mathsf{E})\, [c(\mathsf{E})/c(\mathsf{R})]}{\sum_{\mathsf{X}} m(\mathsf{X})\, [c(\mathsf{X})/c(\mathsf{R})]} \quad (3.10)$$

The denominator sums up the contributions of all occurring elements X with mass $m(\mathsf{X})$.

This equation can be used to convert the relative abundances derived from Eq. 3.9 into the absolute concentration $C(\mathsf{E})$, but requires that all occurring elements are determined. However, one might use Eq. 3.10 as an approximation, if only the presumed majority of elements is measured.

Generally, this procedure is somewhat hazardous: $C(\mathsf{E})$ depends on *all* individual sensitivity factors and count rates. One inaccurately determined relative sensitivity factor or one wrong peak identification in the mass spectrum will affect all $C(\mathsf{E})$! In view of this risk, the results in this study are generally presented as relative element abundance.

Unfortunately, the relative sensitivity factors are not constant, but still dependent on the composition and mineral phase of the sample (matrix effect). Even the crystal orientation matters if the sample is not polycrystalline or amorphous (Benninghoven *et al.*, 1987). Furthermore, the standards for TOF-SIMS have to be homogeneous. Hence it follows that almost only glass standards are usable. $S^{\pm}_{\mathsf{R}}(\mathsf{E})$ is also a function of the E abundance itself. Therefore, one should measure various standards with different $c(\mathsf{E})$ to obtain a calibration curve. If, however, the abundances are a few percent, $S^{\pm}_{\mathsf{R}}(\mathsf{E})$ is approximately constant (Beske, 1967; Andersen, 1969; Hinthorne and Anderson, 1975).

The remaining problem is that the matrices of the samples are rarely amorphous but crystalline silicates. The actual accuracy by applying the relative sensitivities anyway is unknown, because no other analytical technique is able to measure the element abundances in the very same small sample volume as TOF-SIMS does. The intrinsic TOF-SIMS deviations resulting from measurements of different samples with similar composition is about 50 %, and less for repetitive measurements of the very same sample (Homma, 1994). A comparison of TOF-SIMS abundance ratios, which are derived by applying relative sensitivity factors from glass standards on silicates in general, with EDS and PIXE results from the same samples, gives reason to believe that the TOF-SIMS ratios are correct within a factor up to 2. But one has to keep in mind, that this simplified way to determine abundance ratios may yield wrong results if applied to non-silicate samples like salts, sulfides, and sulfates. This especially concerns elements that predominantly occur in such phases, *e.g.*, sulfur, the halogens, and the alkali metals.

3.5 TOF-SIMS analyses of small particles

One goal in this study is the analysis of very IDP surfaces, *i.e.*, the corresponding sample is rough on a scale of some micrometers. The measurements are therefore affected by angular dependencies (Fig. 3.4, Eqs. 3.6, 3.4). It therefore is mandatory to investigate the resulting effects. In case of spectra acquisition, varying heights of secondary ion emission decrease the mass resolution, because they lead to slightly different acceleration voltages and hence drift velocities. Four different effects have to be considered for the understanding of secondary ion distribution images from rough surfaces:

- The actual surface appears to be projected onto the substrate plane.
- From some points no secondary ions reach the detector (shielding).

- The secondary ion yields depend on the angle of incidence and on the angle to the detector.
- The sputter rate depends on the angle of incidence.

Taking these effects into account, the secondary ion image of a sphere as the simplest 'rough' sample is calculated. The results from this model are then compared to experimental data of a spherical particle.

Projection. Typically, the primary ions hit the flat sample surface with an angle of $\sim 45°$. The sputtered secondary ions are extracted perpendicular to this surface. Scanning over a well-defined surface area allows the generation of secondary ion distribution images: Each pixel is attributed to the known scan position of the primary ion beam. In the case of a rough sample surface, or a whole particle, the actually analyzed spot will be virtually projected onto the plane of a hypothetically flat substrate (Fig. 3.6). With the primary ions coming from the right hand side (with respect in the generated distribution images), any particle information is shifted to the left proportional to the height above the substrate plane. This is not a simple linear projection, because the particle surface has variable heights resulting in different shift distances. Therefore, images of rough samples or whole particles usually show distortion effects.

Shielding. It is possible that from some areas no secondary ions could reach the extractor, because they are shielded by the particle (Fig. 3.6). In the resulting images, this shows up as a shadow. Secondary ions are ignored in the model calculation if their point of emission lies right under the sphere.

Secondary ion yields and sputter rates. The angle ψ to the detector has an impact on the secondary ion yields (Eq. 3.6), as well as on the sputter yield (Eq. 3.4). This ψ-dependency approximately holds over the whole ψ and ϑ range (Formann *et al.*, 1968), whereas the formulas are only valid for $\vartheta \ll 65°$. Therefore, the ϑ-dependent part in Equations 3.6 and 3.4 requires a new approach: Introducing a *sputter yield function* $S(\vartheta)$ one can conclude that:

$$Y(\vartheta) \propto \cos^{-1}\vartheta \quad \rightsquigarrow \quad Y(\vartheta) \propto S(\vartheta) \quad \Rightarrow \quad \frac{Y(\vartheta)}{Y(0)} = \frac{S(\vartheta)}{S(0)} \tag{3.11}$$

$$\begin{aligned} \frac{\Delta Y^q(\psi,\vartheta)}{\Delta\Omega} \propto \frac{\cos\psi}{\cos\vartheta} \quad &\rightsquigarrow \quad \frac{\Delta Y^q(\psi,\vartheta)}{\Delta\Omega} \propto \cos\psi\, S(\vartheta) \\ &\Rightarrow \quad \frac{\Delta Y^q(\psi,\vartheta)}{\Delta\Omega\, Y^q(0,0)} = \cos\psi \frac{S(\vartheta)}{S(0)} \end{aligned} \tag{3.12}$$

The sputter yield $S(\vartheta)$ is now approximated by a polynomial that takes into account three boundary conditions: Approximation of $\cos^{-1}\vartheta$ for small

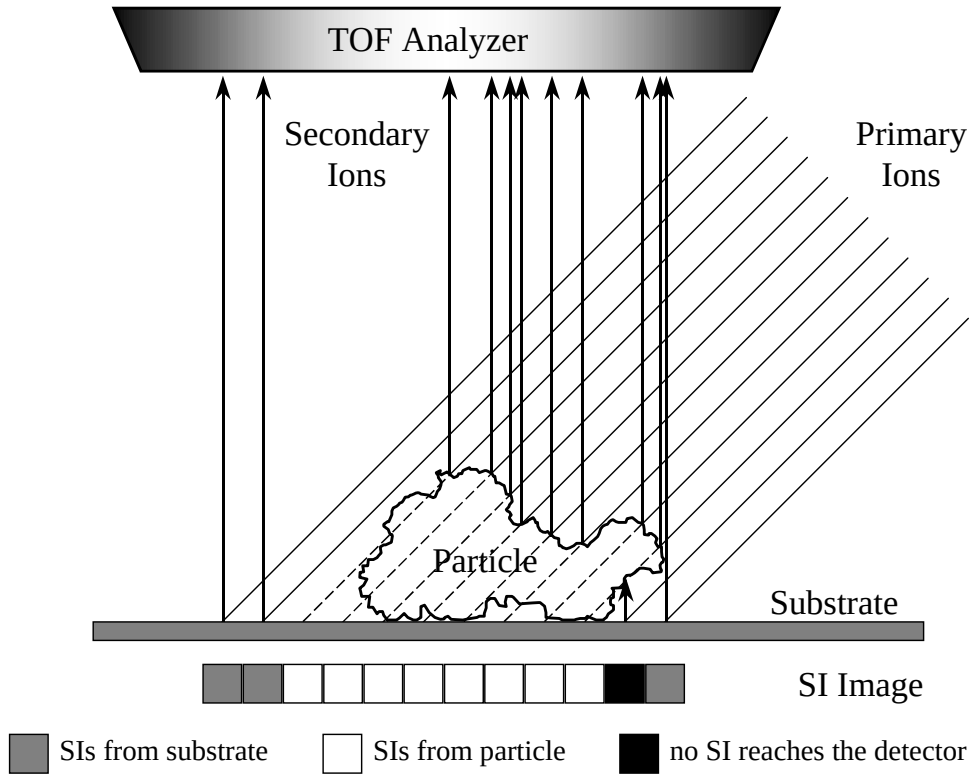

Figure 3.6: Influence of the topography on secondary ion images. As a result of the scanning technique, the actual surface information appears to be projected on the substrate plane. Shadowing or shielding occurs, because the particle obstructs the way of the secondary ions to the detector.

angles ($\Rightarrow S(0°) = 1$, $S'(0°) = 0$, $S''(0°) > 0$), the realization of a maximum, and $\lim_{\vartheta \to 90°} Y(\psi, \vartheta) = 0$. This determines a total of four parameters. Since $Y(\vartheta)$ and $Y^q(\psi, \vartheta)$ should be even functions in ϑ (*i.e.*, symmetric in the y-axis: $Y(\vartheta) = Y(-\vartheta)$, $Y^q(\psi, \vartheta) = Y^q(\psi, -\vartheta)$), also $S(\vartheta)$ must satisfy $S(-\vartheta) = S(\vartheta)$. Therefore, only even exponents are allowed:

$$S(\vartheta)/S(0) \quad = \quad a_0 + a_1\,\vartheta^2 + a_2\,\vartheta^4 + a_3\,\vartheta^6 \tag{3.13}$$

Furthermore, $a_0 = 1$ is a trivial implication from the $S(0°) = 1$ condition. It requires only a basic differential calculus to derive a set of parameters $a_{1,2,3}$ according to the selected position of the maximum secondary ion yield.

The removal of material for a surface point is given by the *sputter rate* $\Delta SR(\vartheta)$. This quantity is not simply proportional to the total sputter yield (Eq. 3.4, 3.11), because the sample area affected by a primary ion pulse dependents also on ϑ. Therefore, the primary ion intensity $I_{PI}(\vartheta)$ per area ΔA

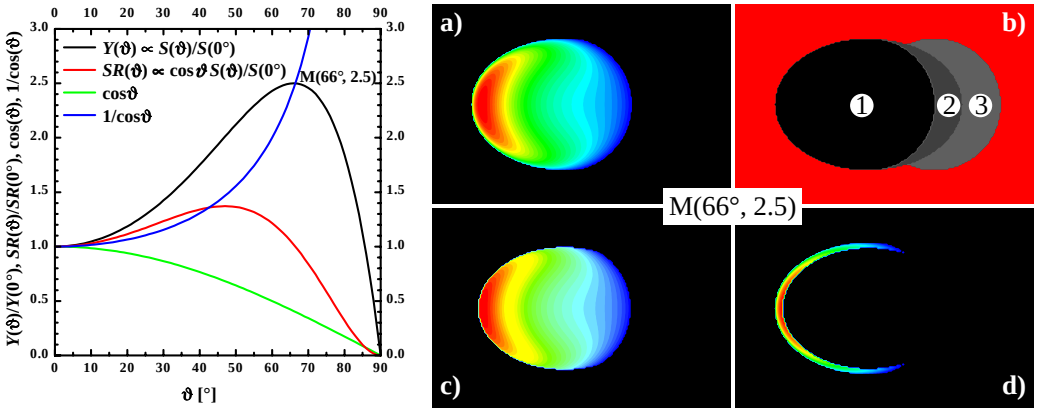

Figure 3.7: The diagram shows the ϑ-dependent parts of the functions used in the model, in this case according to the boundary condition of a maximum in $S(\vartheta)$ at $(66°, 2.5)$. The respective calculations for secondary ion yields are also shown: (a) for a solid sphere, (b) the substrate, and (c) the bulk sphere composition emerging after sputtering off the majority of a thin contamination layer (d). For numbers in (b) see text.

is varying. On the other side, this does not influence the total sputter yields and secondary ion yields, because for each primary ion shot the effective overall intensity remains constant. Basic geometry gives $\Delta I_{PI}(\vartheta)/\Delta A \propto \cos\vartheta$. This leads to:

$$\frac{\Delta SR(\vartheta)}{\Delta A} \propto \frac{\Delta I_{PI}(\vartheta)}{\Delta A} Y(\vartheta) \quad \rightsquigarrow \quad \frac{\Delta SR(\vartheta)}{\Delta A\, SR(0)} = \cos\vartheta \frac{S(\vartheta)}{S(0)} \tag{3.14}$$

Figure 3.7 shows the functions according to a set of parameters (a_1, a_2, a_3), which were calculated from a given position of the maximum in $S(\vartheta)$, here a relative intensity of 2.5 at $\vartheta = 66°$.

Model calculation. Now it is also possible to calculate secondary ion images. A homogeneous sphere lying on a flat substrate with distinct composition is taken as a model to show all occurring effects. A grid of virtual 'raster pixels' is projected onto this setup to account for the actual scanning technique. Based on the determined parameters and Equations 3.12 and 3.13, for each raster pixel the corresponding secondary ion yield is calculated, *i.e.*, the 'detected ions'. Figure 3.7a shows the resulting image for ions from the sphere and Figure 3.7b the respective substrate image. The secondary ion intensities are displayed color coded by first normalizing the image to the maximum intensity and then applying a linear color scale that ranges from black (zero intensity) over blue, green and yellow to red (maximal intensity).

The distribution image of ions from the sphere (Fig. 3.7a) shows a crescent-like enhancement of the signal toward the left side of the particle. The substrate ion yields (Fig. 3.7b) can only be maximum or zero: If primary ions reach the substrate at all, the same (typical) geometrical conditions apply. However, different shades of gray are used instead of just black to identify the differently caused 'shadows'. In the black central area (1) primary ions hit the surface of the sphere instead of the substrate and the produced secondary ions are displayed in Fig. 3.7a. The areas (2) and (3) are caused by shielding of secondary ions: In area (2) the primary ions hit the sphere underneath its equator, and in area (3) they reach the substrate directly under the sphere. In the latter two cases, the sphere obstructs the direct way of secondary ions to the detector.

The angular dependency of removing surface material, *i.e.*, the very sputtering, is simulated by introducing a thin surface layer covering the sphere with yet another composition, *e.g.*, a layer of contaminants. The 'measurement' or 'sputter duration' is realized by increasing the constant of proportionality in Equation 3.14, which gives the sputter rate. For each raster pixel the 'thickness' of the contamination layer is then compared with the achieved sputtering to decide whether the layer is still present or removed. Figure 3.7d shows the sickle-shaped remnant of the layer after parts of it are already removed, in this area the bulk material emerges (Fig. 3.7c). The impact of sputtering is highest toward the top and right side of the particle. Here the primary ions hit almost perpendicular. On the left side, the removal of surface material is less effective because of the lower sputter rates for oblique angles of incidence.

Comparison with experimental data. The results of the calculations are now compared to actual measurements. The most suitable sample is, of course, a spherical particle. Among the stratospheric dust particles, a type of aluminum oxide spheres (AOSs) occurs (Chapter 4.1). AOS particle U2071G8 is an almost perfect sphere. Measurements of the $^{16}O^-$ and $^{12}C^-$ distribution (Fig. 3.8, right) represent the real analysis to be compared with the simulation. A variety of model calculations, arising from different maxima in the sputter yield function $S(\vartheta)$, is also given in Figure 3.8. One has to keep in mind, that the exact position of this maximum is unknown and can therefore be varied to match actual results. The upper images show the solid sphere (Fig. 3.7a) and the lower ones show the contamination layer (Fig. 3.7d).

The actual $^{16}O^-$ and $^{12}C^-$ distributions can be similarly interpreted. Since surfaces are normally covered with thin layers of hydrocarbons, which must be removed prior to proper measurements, the $^{12}C^-$ image corresponds to the calculated surface layer distributions (Fig. 3.8, lower row), but the C

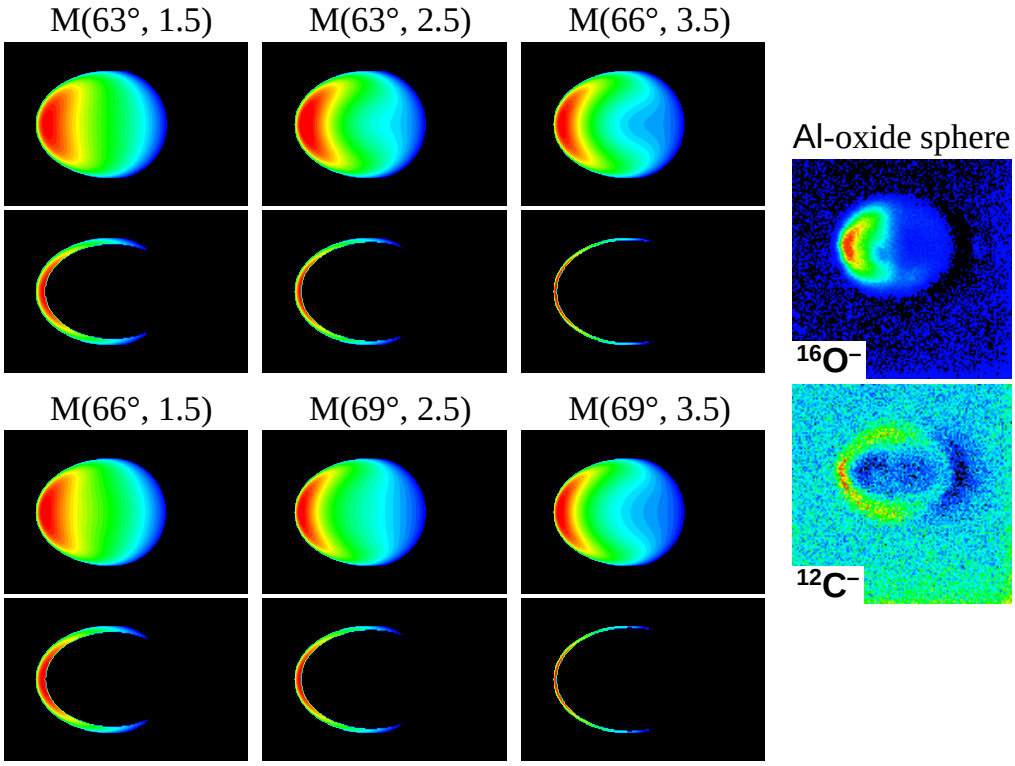

Figure 3.8: Secondary ion distribution images calculated for six different positions of the maximum M in the sputter yield function. Right: Whole particle TOF-SIMS analysis of the Al,O-sphere U2071G8, the field of view is $15 \times 15\,\mu m^2$.

containing substrate is also visible. $^{16}O^-$ mainly represents the bulk composition Al_2O_3. But oxygen is also abundant in the hydrocarbon layer (cf. Fig. 5.2), so that its distribution image corresponds with the simulation of a homogeneous sphere without contaminant (Fig. 3.8d, upper row), than with the image of emerging bulk material (Fig. 3.7c).

The simulated images are in good accordance with the actual measurement; at least qualitatively the variation of the secondary ion signal is reproduced by the model calculation: The $^{16}O^-$ distribution also shows the crescent-like enhancement of ion counts toward the left side of the particle, and the residual $^{12}C^-$ occurs in shape of a sickle that is almost closed to form a ring. A closed ring can only be observed in the simulation just after removing the contamination layer on the top of the particle, but on the 'virtual simulation time' scale it quickly gets thinner and finally opens. However, the simulation indicates that an increase of secondary ion counts on the left

verge of particles is a strong evidence for a thin surface layer covering the bulk particle material.

Concerning the choice of the maximum, slight variation of its ϑ angle only produces insignificant changes. On the other side, different maximum heights result in distinct intensity distributions. Best consistence with the experimental data is achieved with values near 2.5. Shielding is also observed in the measurement of the AOS particle, but the shadow is smaller than simulated.

Shortcomings. Though the match between the model and the measurement is satisfying, the model contains two inadequacies, that can possibly account for the observed minor differences between the calculation and the experiment.

First, of course, the actual shape of the sputter yield function $S(\vartheta)$ and the position of its maximum are unknown. It is also not sure that the very same function $S(\vartheta)$ has to substitute $\cos^{-1}\vartheta$ in the formula for the total sputter yield (Eq. 3.11), as well as in the formula for the secondary ion yield per solid angle (Eq. 3.12). Concerning the removal of the contamination layer a less expressed maximum in the sputter rate function — compared with the secondary ion yield function — would enhance the agreement between simulation and experiment.

Second, the extent of the shadowing effect might be decreased by secondary ions that follow bent field lines around the sphere. Since the actual electric field near the particle is not known, this could not be considered in the model. Such ions from 'forbidden' areas can explain, why the real shadow in Fig. 3.8 is less pronounced than the calculated one (3) in Fig. 3.7b. Furthermore, if ions from area (2) in Fig. 3.7b, which originate from the sphere below its equator, would reach the detector, the sickle-shaped appearance of the remaining contamination layer will close into a ring.

Summary. Altogether, the effects involved in the TOF-SIMS analysis of rough samples seem to be understood; the simulation qualitatively reproduces the measured secondary ion images. A major point is the discovery that any surface (contamination) layer on a sphere will appear in ring or sickle shape after some sputtering, because the sputter rate and hence removal of surface material approaches zero for glancing angles of primary ion incidence.

Chapter 4

Implementation of the Collector Project

This chapter provides details concerning the *Collector Project*, *i.e.*, the comprehensive consortium study of stratospheric dust particles. The *Johnson Space Center* (*JSC*) provided the small area collector U2071 for this study. It was exposed in a series of flights over the United States at an altitude of 20 km, between January 7 and February 8, 1994, resulting in an overall sampling time of 34.1 hours (Stephan *et al.*, 1995). Particle preparation was performed under class 100 clean room conditions, first at *JSC* in Houston, later at the *Max Planck Institut für Kernphysik* in Heidelberg, and finally at the *Institut für Planetologie* in Münster.

The selection of analytical techniques and the sequence in which they are applied is optimized to maximize the scientific information and to minimize disturbing effects from one technique on subsequent measurements:

Optical microscopy. Optical microscopy is first used to spot the particle in the silicone oil of the collector flag. Its position, size, and color is cataloged. All particle preparation is done by aid of microscopes.

SEM. Scanning electron microscopy (SEM) provides a highly resolved secondary electron image of the particle that allows characterization of the morphology. Combined with energy dispersive X-ray spectrometry (EDS), the major element abundances are obtained from the uppermost $\sim 2\,\mu m$ of particle material, referred to as *quasi-bulk* analysis. The results allow a preliminary classification.

TOF-SIMS. The very surface is inspected to determine a possible contamination. Secondary ion distribution images with a lateral resolution of $\sim 0.2\,\mu m$ and element abundances are gained.

PIXE. Proton induced X-ray emission analysis (PIXE) determines the absolute bulk abundances of all elements with atomic numbers $Z \geq 12$ (Mg),

including trace elements (Arndt *et al.*, 1997). With reduced proton beam intensity, as applied in the first step for the whole particle analysis, it is nondestructive (Maetz *et al.*, 1996). The element distribution is also obtained with the proton beam focused to $\sim 1\,\mu m$ and scanned over the sample.

STIM. The scanning transmission ion microprobe (STIM) measures the energy loss of the protons after they passed the particle. The energy loss depends on the penetrated mass. The mass density distribution, the mean density, and the total mass of the particle is derived (Maetz, 1994).

PIXE and STIM are part of the same experimental setup and are applied simultaneously. Samples must be tenuously coated with a conductive substance, *e.g.*, carbon.

TOF-SIMS (section). TOF-SIMS analysis of the sectioned particle allows to relate the internal element abundances with the surface composition. Minerals with particular composition are reliably discovered.

FEG-SEM. Field emission gun SEM provides a highly resolved secondary electron image of the whole particle or section just after TOF-SIMS analysis. The image allows to localize features found by TOF-SIMS.

TEM (thin section). Transmission electron microscopy (TEM) enables mineral identification and characterization with almost atomic resolution. Equipped with an energy dispersive X-ray spectrometer, the major element abundances are measured on the same scale. TEM is performed on thin sections (*i.e.*, $\sim 100\,nm$ thick slices) from the particle.

PIXE/STIM (section). High intensity measurements that could damage some minerals will be performed only with a $\sim 1\,\mu m$ thick section. Due to the now attained low limits of detection, it is especially suitable to determine trace element abundances. Element distribution images with micrometer resolution are derived as well.

4.1 Particle selection and classification by SEM-EDS

During a first survey at *JSC* with binoculars 326 particles or particle fragments $\gtrsim 10\,\mu m$ were located on the collector U2071. Their positions, sizes, and colors were catalogued. Subsequently, 114 *representative* particles or fragments, presumably belonging to 90 different particles, were analyzed with SEM-EDS (Stephan *et al.*, 1995). 'Representative' means that it was attempted to include all types of particles. The particles were mounted on Be-substrates and were not carbon coated in order to allow C analysis (Thomas *et al.*, 1993, 1994). Based on the results, the stratospheric dust particles are

pre-classified according to the scheme used in cosmic dust catalogs (Warren and Zolensky, 1994):

C These *cosmic* particles are most probable of extraterrestrial origin. The composition is *chondritic* for most of them, *i.e.*, the abundances of the major elements match CI abundances within a factor of two, in case of carbon within a factor of three. This does not apply for the Fe,Ni,S dominated FSN particles, but they often have a chondritic component attached or inside.

TCN = Terrestrial contamination, natural. Their compositions indicate a natural terrestrial origin, mostly volcanic.

TCA = Terrestrial contamination, artificial. These particles are presumably anthropogenic: fragments of paint, solar cells and so on.

AOS These aluminum oxide spheres are almost pure Al_2O_3. They represent a significant portion of the stratospheric particles $\lesssim 10\,\mu m$ and are combustion products of solid fuel rocket burning (Brownlee *et al.*, 1976b). They form as droplets and usually keep this shape. The largest contribution to this particle type results from the space shuttle booster rockets.

? Actually a nonclassification. Their SEM-EDS derived composition gives no clue to their possible origin.

The relative abundance of the particle types on a given collector depends on several factors like recent volcano eruptions (Rietmeijer, 1995) or number of space shuttle starts (Rietmeijer and Flynn, 1996). The pre-classified particles are named like, *e.g.*, U2071B7a, according to following notation: [name of collector, here U2071][capital letter (A–L) denoting the Be substrate][particle number (1–9) on substrate][supplementary lowercase letter referring to the fragment of a particle that broke apart during preparation].

The particles presented in this study are only a selection out of all 114 pre-classified stratospheric dust particles, *i.e.*, those that were subjected to the subsequent stages of the Collector Project, including TOF-SIMS analysis. This selection was not restricted to presumed cosmic dust, but included all types of stratospheric particles (cf. Table 5.1). With this, it might be possible to discover a new type of so far unknown extraterrestrial material. On the other hand, the terrestrial particles could also be indicative for contamination and alteration processes in the atmosphere. Following particles (with type) were selected: U2071B6, B7a, C3, D4, E8, F3, H1a, H9, J9a, and L1 (all C), U2071B3, D8, G8, and L2 (all AOS), U2071D1 (?), U2071E6 (TCN) and U2071I9 (TCA). All cosmic particles have chondritic compositions, except

for U2071H9 which is an FSN IDP that had a minor amount of chondritic material attached (Stephan *et al.*, 1995).

4.2 Particle preparation for TOF-SIMS surface analyses

Silicone oil (dimethyl polysiloxane, a chain of $-Si(CH_3)_2O-$ structure elements) plays a major role during collecting and handling stratospheric dust particles. First, its high viscosity enables capture of the particles in the stratosphere usually without damage. Its stickiness is also useful for particle manipulation and transfer onto different substrates (Fig. 4.1). Finally, silicone oil is chemically inert, which is a prerequisite for any substance in contact with IDPs. Prior to surface analysis, the silicone oil has to be removed by rinsing with hexane. A complete removal, however, was proved to be difficult (Sandford and Walker, 1985). A discontinuous contamination layer of about 1 nm thickness remains (Rietmeijer, 1987), which is for most analyses no obstacle. Following procedure was applied to all stratospheric dust particles of this study:

1. Transfer from the collector flag onto the Be substrates by use of a quartz glass fiber

2. Rinsing with hexane to remove the silicone oil. A notch in the substrate prevents particle loss. Sometimes particles broke apart.

3. Storage in (new) silicone oil on dimpled glass slides after SEM-EDS analysis. The transfer was done again with the fiber with a silicone oil droplet on the tip.

4. Transfer onto a substrate for TOF-SIMS analysis

For the initial TOF-SIMS surface analyses Kapton[1] was chosen as substrate (Rost, 1995), because it is a robust and inert material normally used for the subsequent PIXE analyses as well. Therefore, no additional particle transfer was needed for the next step in the sequence of analyses. Only very cautious and ineffective hexane rinsing was possible, because the particles were 'floating' in hexane — with considerable danger of particle loss. Because of that, rinsing was rather ineffective: The very surfaces of six stratospheric dust particles could not be analyzed.

[1] the brand name of a poly-(diphenyloxide-pyromellith-imid)

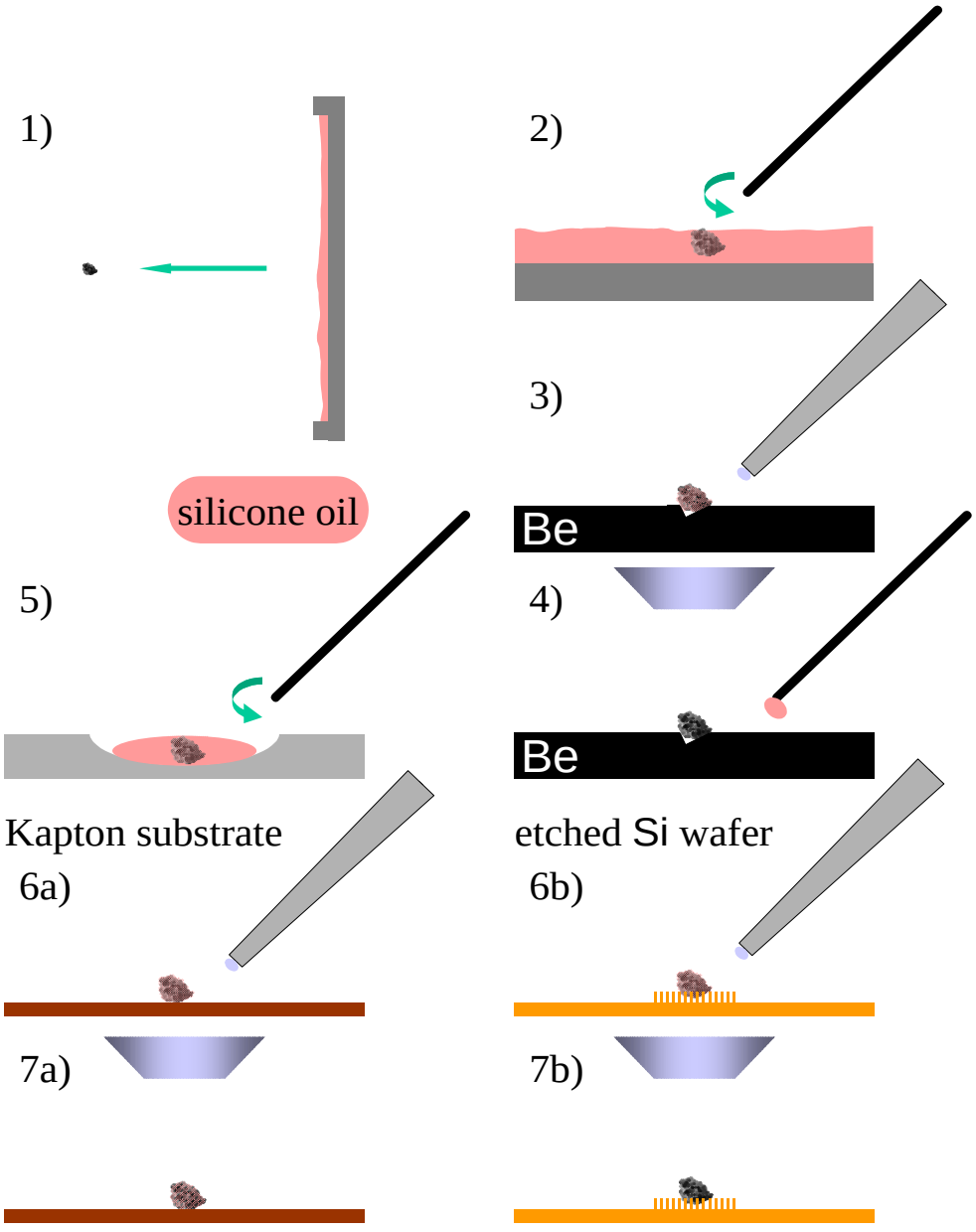

Figure 4.1: Schematic overview of particle preparation: (1) Collection in stratosphere (2) Picking with glass fiber (3) Hexane rinsing prior to SEM analysis (4) Transfer to storing slides afterwards — until being picked again (5) (6a, b) Use of different substrates for a second cleaning procedure before performing the TOF-SIMS analysis (7a, b)

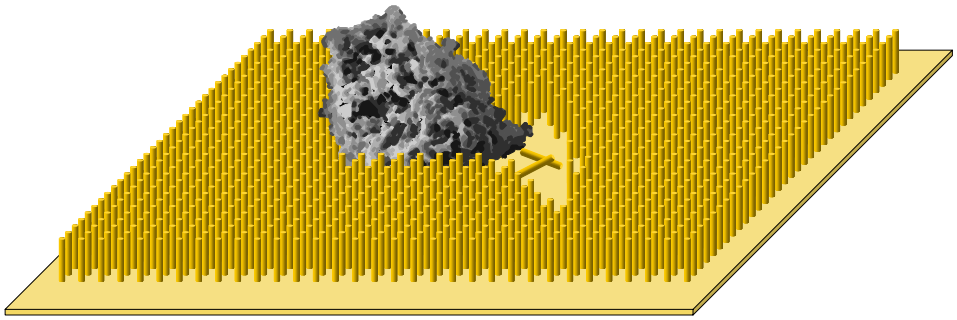

Figure 4.2: Particle on etched silicon wafer. The tiny needles hold it tight, but easily break when it is placed at first with the glass fiber.

A new method had to be implemented. Etched silicon wafers, provided by P. Hudek and I. W. Rangelow, proved to be a good solution (Fig. 4.2). These substrates are characterized by tiny upright standing needles, 0.5 µm in diameter and 4 µm long. The needles hold the particle tight enabling extensive hexane rinsing. From the production process — one of the etching acids was HF — the silicon surface is contaminated by F. The needles are very fragile and easily break when a particle is positioned.

The next step after TOF-SIMS surface analysis is a first PIXE measurement of the whole particle, including STIM, that require carbon coating. This was done with the particles mounted on Kapton. PIXE measurements of particles mounted on etched wafers were not possible, because the instrument was out of service. Therefore, these particles were directly prepared for TEM and TOF-SIMS section analysis. A carbon coating was not necessary for these particles.

4.3 Preparation for TEM, TOF-SIMS and PIXE section analyses

Afterwards the particles were embedded in epoxide resin and with an ultramicrotome thin sections (thickness: $\sim$100 nm) were made for the following TEM analysis. The cutting is stopped just after cutting approximately half of the particle. The remaining stub allows section analysis of the particle with TOF-SIMS.

The last stage of the Collector Project is a highly accurate PIXE analysis of the section. For this purpose a 0.5–2 µm thick section was attempted to

cut off the stub. That, however, only succeeded for the particles U2071B6, C3, E8, H9, and L1, while it failed for U2071D1, D4, E6, and I9.

Chapter 5

Results and discussion

Some general remarks and the status quo of the Collector Project are given at the beginning of this chapter. Then the presentation of the results is explained. Finally, the results of the selected particles are successively presented and discussed, with the emphasis on TOF-SIMS surface and section analysis.

The SEM-EDS analysis and the evaluation of major element abundances was performed at *JSC*, Houston, by T. Stephan, K. L. Thomas, and J. L. Warren. SEM images and elemental compositions are taken from Stephan *et al.* (1995).

P. Arndt, M. Maetz, and C. Wies analyzed the particles with PIXE/STIM at the *Max Planck Institut für Kernphysik*, Heidelberg, and interpreted the data. The here included results are taken from Arndt (1997) and Wies (1998).

The examination of particle thin sections with TEM was performed by W. Klöck and K. Nakamura (*Martin-Luther-Universität Halle-Wittenberg*). They also provided the here included interpretations (pers. comm.).

The Collector Project is continuously in progress. Table 5.1 summarizes the investigations until April 2000. It was not possible to apply each method on each particle as planed, the respective reasons are indicated in the table.

Method	**Particles**																
Binoculars	326 particles $\gtrsim 10\,\mu m$																
SEM-EDS (quasi-bulk)	90 particles / 114 fragments																
Type of...	C										AOS				?	TCN	TCA
...selected particle	B6	B7a	C3	D4	E8	F3	H1a	H9	J9a	L1	B3	D8	G8	L2	D1	E6	I9
TOF-SIMS (surface)	$(\checkmark_K)$	$(\checkmark_K)$	$(\checkmark_K)$	$\checkmark_W$	$\checkmark_W$	$(\checkmark_K)$	$(\checkmark_K)$	$\checkmark_K$	$\checkmark_W$	$\checkmark_W$	$\checkmark_K$	$\checkmark_K$	$\checkmark_K$	$\checkmark_K$	$\checkmark_K$	$(\checkmark_K)$	$\checkmark_K$
PIXE (bulk)	✓	†	✓	⇓	⇓	✓	◇	✓	†	⇓	◇	◇	✓	◇	✓	✓	✓
STIM (bulk)	✓	†	✓	⇓	⇓	✓	◇	✓	†	⇓	◇	◇	✓	◇	✓	✓	✓
TEM (thin section)	✓	†	✓	✓	✓	✓	◇	✓	†	✓	◇	◇	✓	◇	✓	✓	✓
TOF-SIMS (sect./stub)	✓	†	✓	✓	✓	†	◇	✓	†	✓	◇	◇	†	◇	✓	✓	✓
PIXE (section)	◇	†	◇	†	◇	†	◇	◇	†	◇	◇	◇	†	◇	†	†	†

Table 5.1: The progress of the Collector Project. Finished measurements are marked with ✓. The subscripts K and W specify the substrate used for TOF-SIMS surface analysis, Kapton or etched Si-wafer, respectively. Brackets indicate that the very analysis failed because of silicone oil residues on the particle's surface. † either indicates particle loss after TOF-SIMS surface analysis, absence of any particle residues in the remaining stub after preparing the TEM thin sections, or failure to prepare sections for PIXE. Some PIXE analyses had to be skipped (⇓), because the instrument was out of service. Finally, ◇ marks unfinished or future measurements.

5.1 Data presentation

The results of each particle are combined in individual sections, except for AOS particles which are discussed together. The presentation follows the same order as the actual measurements, as far as performed:

1. **SEM-EDS analysis** (size, morphology, secondary electron image, quasi-bulk elemental composition, classification)
2. **Surface analysis** (element abundances of outermost surface, secondary ion images)
3. **PIXE bulk analysis** (bulk elemental composition, 2-dimensional bulk element distribution)
4. **TEM** (interpretation of thin section analysis)
5. **Section analysis** (element abundances and distribution from a section surface)

A table with all element abundances and figures containing the image results are provided in the context:

Table of element abundances. Except for the AOS particles, each particle has a separate table providing the element abundances from SEM-EDS (quasi-bulk), PIXE (bulk), and TOF-SIMS (surface and section) — as far as they are available. Two columns are assigned to each technique. The first one presents the data in the way it is usually given for this technique:

SEM-EDS: in [wt%]

PIXE: E/Fe [wt] represents the mass ratio of the element relative to Fe (≡100; older measurements).
in [wt%]: when determination of absolute element concentrations was possible (Arndt *et al.*, 1997).

TOF-SIMS: E/Si [at] is the atomic abundance ratio of the element relative to Si (≡100).

The second column gives the element abundance relative to CI chondrites and normalized to Si (≡100):

$$[\mathsf{E}]_{\mathsf{Si,CI}} \equiv \frac{c(\mathsf{E})/c(\mathsf{Si})}{c_{\mathrm{CI}}(\mathsf{E})/c_{\mathrm{CI}}(\mathsf{Si})} \tag{5.1}$$

This enables comparison of the results from the different techniques. In the discussion the term '$\times\,\mathrm{CI}_{\mathsf{Si}}$' refers to data of this column, *i.e.*, indicates a value relative to the corresponding, Si-normalized CI abundance.

The error affects the last significant digit. If a value is given in italics, the relative error is $\geq 50\,\%$. For TOF-SIMS measurements the usage of relative sensitivity factors accounts for uncertainties up to a factor of two. In the data presentation only the statistical error is considered, but with the number of significant digits restricted to two — even if the statistical error would allow more digits. The CI and Si-normalized PIXE results ($[\mathsf{E}]_{\mathsf{Si,CI}}$ column) are affected by an additional systematic error. It is due to the error of the Si measurement. In case of the particles U2071C3 and I9, this error is greater than 10 %, otherwise less than 10 %.

TOF-SIMS results from measurements of positive and negative secondary ions are given. Element symbols printed in italics indicate negative secondary ions. The Cl and P values have to be taken with special caution, because usually they do not occur in silicates (cf. Chapter 3.4).

TOF-SIMS secondary ion distribution images. The TOF-SIMS scanning images represents the lateral variation of the secondary ion signal of the ion species indicated on the left side below the image. The number of counts in one pixel is normalized to the maximum of this distribution image and visualized through a commonly applied linear color scale: black corresponds to zero counts, then increasingly higher counts are given by a continuous sequence from blue over green and yellow, ending up with red for the pixel(s) with the highest number of counts. This number can be found on the right side below the image. Underneath that, the total number of counts is given, *i.e.*, the sum of all counts in this image. On top of all individual images the sample is specified (left), as well as the names of the data files and the number of primary ion shots per pixel (SpP). Sometimes also a secondary electron (SE) image is provided which was taken during the TOF-SIMS analysis. The caption gives some further information: the size of the field of view, the number of pixels, and if a sputter gun was applied.

The shift correction (Chapter 3.2) is responsible for some margins of low or zero secondary ion signal that can often be seen in the distribution images: Since the field of view shifted into one direction during the measurement, only some of the applied scans cover this margin. This effect is usually different for the measurements of positive and negative secondary ions.

Field emission gun SEM (FEG-SEM) images provide high lateral resolution and are provided for better orientation. The uncoated samples had to be analyzed with electron energies below X-ray excitation, so that at this stage no quantitative analysis was possible. The particle's orientation in the FEG-SEM image is the same as in TOF-SIMS analysis, because the particle is still lying on the same substrate. On the other hand, the orientation in the SEM image taken in Houston was usually different, because it experienced two transfers and hexane rinsing afterwards.

PIXE bulk element distribution images. 2-dimensional element distributions are shown, in the same color scale as applied for TOF-SIMS, whenever they supply further information, *i.e.*, a heterogeneous distribution which can be compared with TOF-SIMS section results. The image of proton induced secondary electrons (e^-) is also provided, because it shows the orientation of the particle. The basic principle of STIM analysis lies in the energy measurement of the protons that passed the sample: $E'(p)$. In the corresponding image the lowest energy, *i.e.*, the highest energy loss, is displayed in red and indicates the maximum mass experienced. Blue is assigned to the highest energy, *i.e.*, the lowest energy loss, which therefore denotes that less mass was penetrated — usually the surrounding Kapton substrate.

Discussion. A direct comparison of the results from different techniques is difficult, because the respectively analyzed material is different and its mutual relation unknown. Only in some cases a similar orientation of the particle during different analyses allows to compare results form the very same sample volume. The tremendous amount of information derived from the various methods prevents a thoroughly discussion of all given data. The discussion in this work is therefore restricted to the most relevant results.

5.2 Aluminum oxide spheres: U2071B3, D8, G8, L2

SEM-EDS analysis. All four particles are 7–8 µm sized spheres. While U2071G8 and D8 are almost perfect spheres with smooth surfaces, L2 and B3 have increasingly rougher surfaces (Fig. 5.1). Aluminum oxide spheres (AOSs), the solid fuel rocket exhaust, consist almost entirely of corundum: Al_2O_3 (53 wt% Al, 47 wt% O). The SEM-EDS derived quasi-bulk abundances (Table 5.2) correspond well with corundum. The minor occurrence of Si might be due to residues of silicone oil, by which the rougher particles U207L2 and B3 are more affected.

Surface analysis. As mentioned before (cf. Chapter 3.2) every sample surface is at first covered with adsorbed gas molecules and hydrocarbons. Underneath this layer more or less silicone oil resides. At the time of measurement, the TOF-SIMS instrument was not yet equipped with a special sputter gun. As a substitute, extensive usage of the Ga primary ion gun was necessary to remove the obstructive surface layer.

Figure 5.2 shows negative secondary ion images of U2071G8 from two different measurements, before (left) and after (right) sputtering off the majority of the impeding layer. The early measurement is dominated by H^-,

	U2071G8			U2071D8			U2071L2			U2071B3			
	SEM	TOF-SIMS (surf.)		SEM	TOF-SIMS (surf.)		SEM	TOF-SIMS (surf.)		SEM	TOF-SIMS (surf.)		
E	[wt%]	E/Si [at]	[wt%]	[wt%]	E/Si [at]	[wt%]	[wt%]	E/Si [at]	[wt%]	[wt%]	E/Si [at]	[wt%]	
Li		0.0005	60					*0.0004*	*100*				ppb
Be		0.67	100		4.3	670		0.07	36		2.2	3.1	ppm
B		0.16	30		0.12	22		0.010	6		0.016	27	ppm
C		400	8.3		410	8.5		470	31		130	25	
O	45	2000	55	47	2000	57	46	510	45	47	90	20	
Na		6.5	2.6		1.3	540		0.35	450		1	4.7	‰
Mg	0.2	0.078	32	0.2	0.20	85	0.3	0.030	41	0.2	0.015	55	ppm
Al	54	670	31	52	620	29	52	48	7.3	52	13	5.5	
Si	0.58	≡100	4.8	0.55	≡100	4.9	0.82	≡100	16	0.63	≡100	43	
P	*4*			*5*			*4*			*5*	*4*	*2*	‰
S										4			‰
Cl		1.7	9.1		0.36	970		0.12	320		0.18	320	‰
K		0.10	66		0.042	28		0.0073	16		0.013	78	ppm
Ca		0.58	400		2.6	1.8		0.20	450		0.026	160	ppm
Ti		0.008	*7*		0.02	10		*0.001*	*4*				ppm
V		0.0022	1.9					*0.0005*	*1*				ppm
Cr		0.27	240		0.04	40		*0.0008*	*2*				ppm
Mn					0.018	17		0.008	30		*0.001*	*10*	ppm
Fe					0.11	110		0.04	100		0.14	1.2	ppm

Table 5.2: Element concentrations in AOSs. 'SEM' denotes the SEM-EDS analysis. The average of two small area measurements is given for the TOF-SIMS surface analysis.

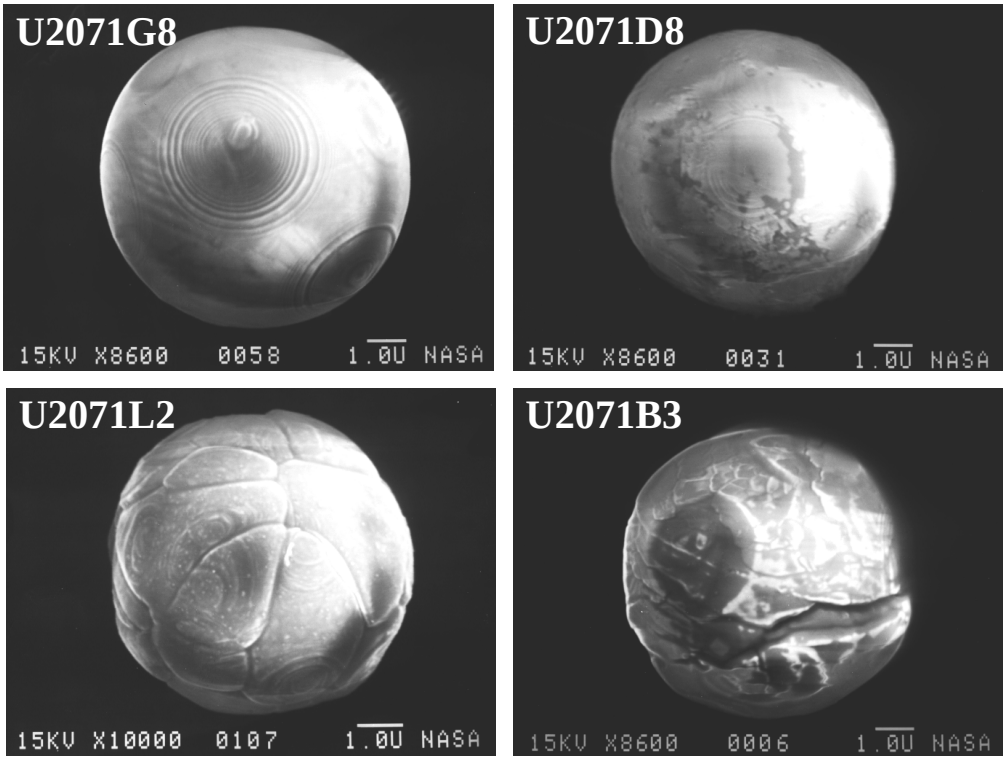

Figure 5.1: SEM images of the aluminum oxide spheres U2071G8, D8, L2, and B3.

C^-, O^-, and molecular ions composed of these elements. As expected for a surface contamination (Chapter 3.5), they appear ring-shaped. Neither Al compounds nor halogen ions are detected on the surface. After sputtering O^-, AlO^-, and even negative Al ions are detected with a distribution as expected for bulk material (cf. Fig. 3.7c). Now also the halogens F and Cl appear. They occur in a ring-shaped distribution comparable with H^-, C^-, CH^-, and OH^-. The diagonal 'band' of high Cl^- intensity is probably a contamination of the Kapton substrate. Br is also identified in the mass spectrum, but the signal was to weak for imaging.

Principally the same results are obtained from the other AOSs. Only measurements after sputtering are shown, with the bulk material visible. The TOF-SIMS secondary ion distribution images of particle U2071B3 (Fig. 5.3, left) indicate the cracked surface that can also be seen in the SEM image (cf. Fig. 5.1). Cl^- appears sickle-shaped as do H^-, C^-, CH^-, and OH^-. The CH^- image indicates, that residues may survive hexane rinsing in the cracks. The more diffuse F^- distribution rather appears ring-shaped, at least it is clearly

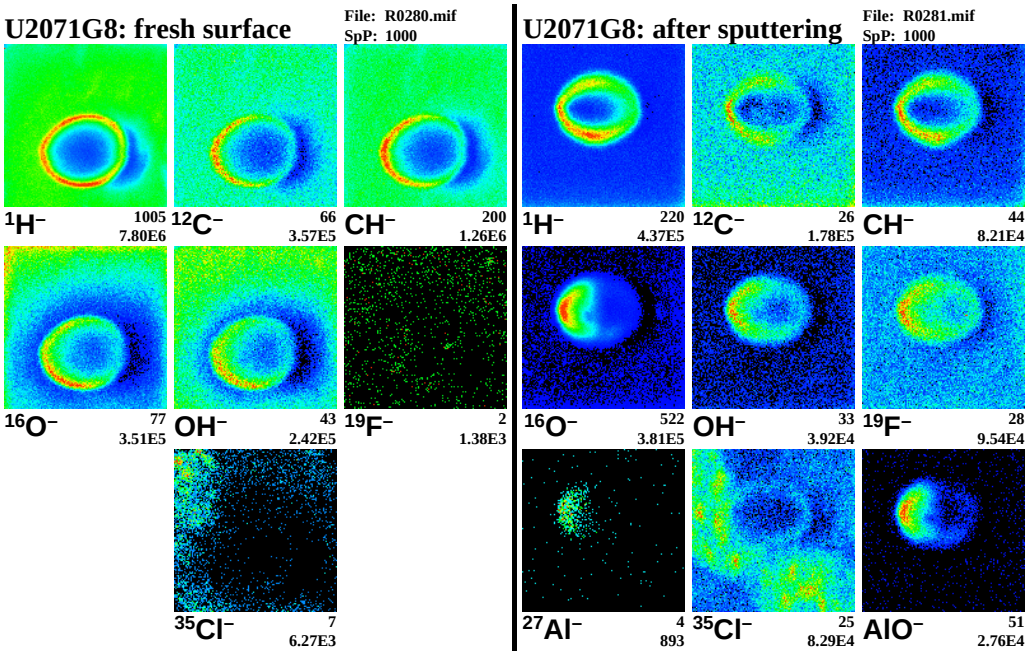

Figure 5.2: Field of view: $19 \times 19\,\mu m^2$; 128×128 pixels; no sputtering

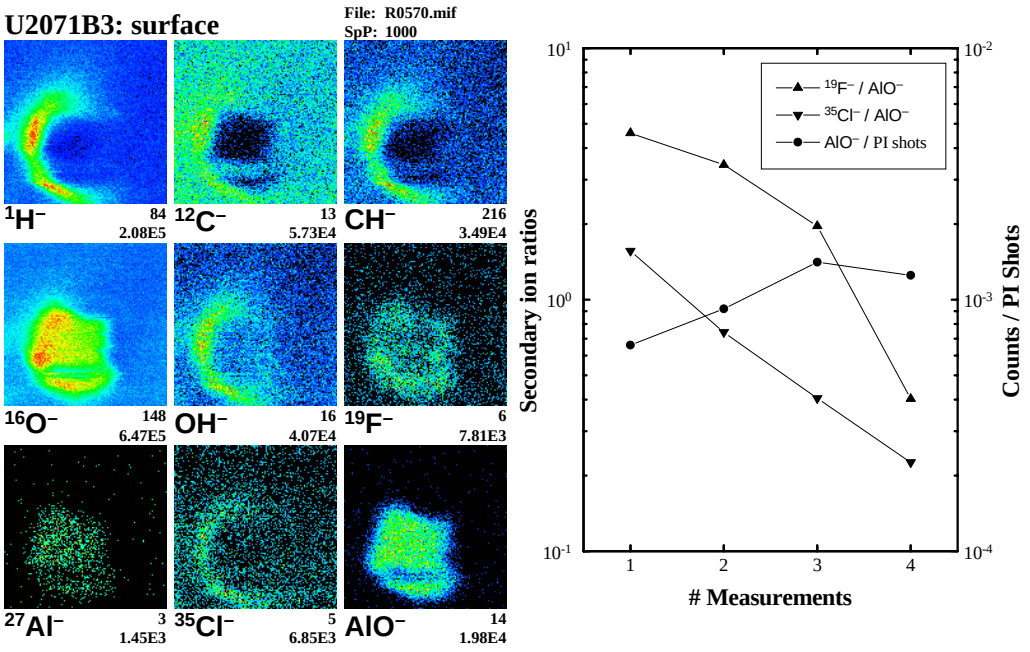

Figure 5.3: (Left) Field of view: $12 \times 12\,\mu m^2$; 128×128 pixels; no sputtering. (Right) For subsequent TOF-SIMS measurements the $^{19}F^-/AlO^-$ and the $^{35}Cl^-/AlO^-$ ratios are shown, as well as the absolute occurrence of AlO^-.

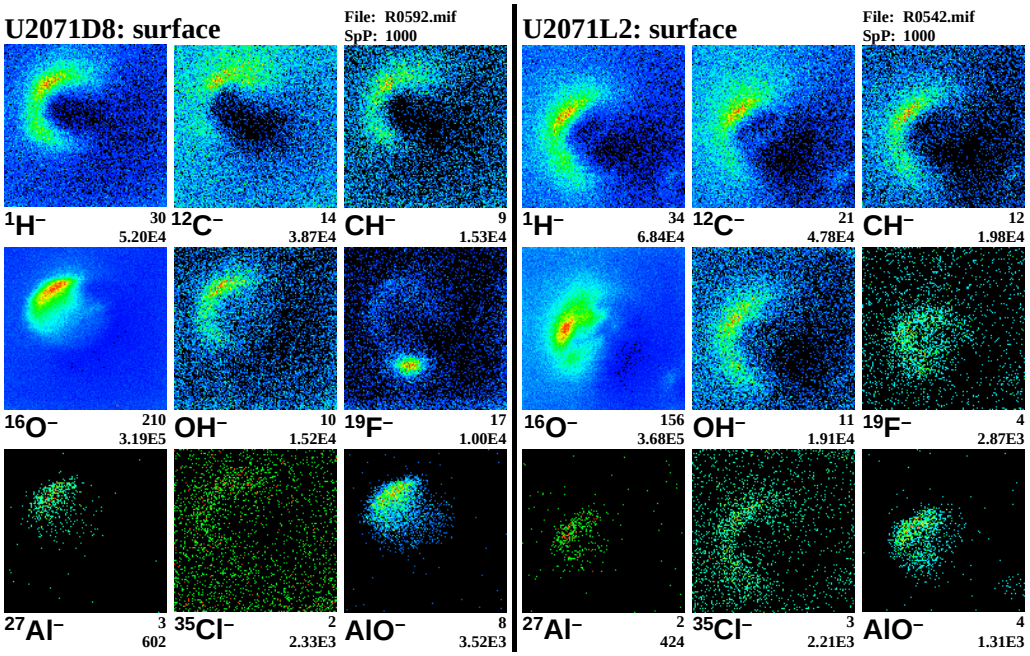

Figure 5.4: Field of view: $12 \times 12\,\mu m^2$; 128×128 pixels; no sputtering

distinct from the AlO^- image representing the bulk material. The intensity distribution of the AlO^- ions is not semicircular and lacks the enhancement on the left particle edge that is obvious for U2071G8 (Fig. 5.2) and expected from the model calculations (Fig. 3.7c). This lack results from the particle shape that is not a perfect sphere.

Several subsequent secondary ion mass spectra are acquired for U2071B3. While the count ratios of the halogen ions $^{19}F^-$ and $^{35}Cl^-$ relative to AlO^- are decreasing, the absolute occurrence of AlO^- increases (Fig. 5.3, right). This is the expected behavior when sputtering off a thin surface layer.

Figure 5.4 shows the AOSs U2071D8 and L2. In case of D8, the halogen intensities are rather weak, but clearly distinct from the aluminum oxide. Most of the F^- comes from a small spot at the lower particle edge and may be the residue of an aerosol droplet. On U2071L2 only Cl^- appears slightly sickle-shaped, whereas F^- corresponds to the bulk AlO^- ion distribution.

The quantitative results of the TOF-SIMS surface analyses are given in Table 5.2. The particles are arranged according to increasing surface roughness. Here also element concentrations are given for comparison with the SEM-EDS results. The normalization to Si has to be taken with caution, because Si may stem from silicone oil. Moreover, the amount of silicone oil residues is different on the various Al,O-spheres.

The TOF-SIMS data of the two particles with the smoothest surface (U2071G8, D8) match the SEM results best. Nevertheless, the TOF-SIMS determined Al abundance is too low by a factor of ~ 1.5. Si and C indicate minor residues of silicone oil. For the rougher AOSs (U2071L1, B3) the oil presents a much more persistent impediment: The Al abundances are more than five times lower than expected, and Si and C prevail — O is a constituent of silicone oil as well as of aluminum oxide. Other elements are only found in traces.

Section analysis. As yet it was not possible to prepare a section of an AOS particle. Cutting with an ultramicrotome failed for U2071G8 and the remaining stub contained no AOS remnants: Since corundum is very hard, the particle broke out of the more pliable epoxy.

Discussion. SEM-EDS and TOF-SIMS results indicate that the amount of silicone oil residue is correlated with the surface roughness, which was concluded before from cosmic particles (Rietmeijer, 1987). With TOF-SIMS a thin halogen bearing surface layer was found. It is not plausible to assign the halogens to the silicone oil, because the halogens emerge only after sputtering. After extended measuring (and sputtering), they disappear again with increasing intensity of aluminum oxide ions. Therefore, the halogen layer is localized directly above the constituent Al_2O_3.

Previous studies on AOSs indicate a general contamination with Cl just after their formation (see Turco *et al.*, 1982, and references therein), since the exhaust of solid fuel rockets contains not only AOSs (30 wt%) but also HCl (21 wt%) and other gases (Prather *et al.*, 1990). Chlorine can form a chemically bound, one monolayer thick aluminum salt crust, onto which other hydrophilic substances may adhere (Cofer *et al.*, 1984).

Consequently, the observed Cl could (in part) be an original characteristic of AOSs, but the F and the Br found in the mass spectrum of U2071G8 probably result from subsequent stratospheric contamination processes.

5.3 Terrestrial contamination particles

5.3.1 U2071E6 (TCN)

SEM-EDS analysis. U2071E6 37 µm × 23 µm sized particle has an irregular surface morphology (Fig. 5.5). It was classified as natural terrestrial contamination according to its element concentrations (Table 5.3) that do not match CI values and are also not characteristic for known non-chondritic IDP types. The concentration of Al (8.1 wt%), Si (24.7), and Ca (7.7 wt%) in

	SEM-EDS		PIXE (bulk)		TOF-SIMS (surf.)		TOF-SIMS (sect.)	
E	[wt%]	$[E]_{Si,CI}$	E/Fe [wt]	$[E]_{Si,CI}$	E/Si [at]	$[E]_{Si,CI}$	E/Si [at]	$[E]_{Si,CI}$
Li							0.058	1000
Be							*0.007*	*9000*
B							0.23	11000
C	5	60			15000	20000	150	200
C					72000	95000	240	320
O	43	41			50	6.5	330	43
O							350	45
Na			140	420			1.9	33
Mg	1.5	6.5	35	5.4			6.4	6.0
Al	8.1	400	224	395			20	230
Si	25	≡100	694	≡100	≡100	≡100	≡100	≡100
P			4.8	61			0.5	40
S	0.93	6.4	12.0	2.93				
Cl	*0.2*	*100*	6.4	140			5.3	1000
K	3.0	2300	77.5	2130			7.2	1900
Ca	7.7	360	149.1	246.4			12	190
Sc							0.01	300
Ti	0.5	500	8.2	290			0.1	50
V							0.004	10
Cr							0.004	0.3
Mn			1.7	13			0.15	16
Fe	4.7	11	≡100	8.05			9.5	11
Co			0.5	20				
Ni			0.36	0.50				
Cu			0.33	40				
Zn			0.47	23				
Rb							0.014	1900

Table 5.3: Element abundances in U2071E6. The TOF-SIMS surface analysis actually represents a measurement of impeding silicone oil residues.

contrast to the relatively low Mg (1.5 wt%) and Fe (4.7 wt%) content suggest a volcanic origin and hence a TCN particle.

Surface analysis. This particle is a typical example for a strongly silicone oil contaminated particle. The impeding oil is at least several monolayers thick, since extended sputtering with Ga primary ions did not remove it. Therefore, no TOF-SIMS analysis of the proper surface was possible. Only oil constituents and organic compounds are detected, *e.g.*, C_2H^- and $C_4H_7^+$ in Figure 5.5. Other typical molecular ions include: $C_2H_3^+$, Si^+, $SiCH_3^+$, $C_4H_7^+$, $Si(CH_3)_3^+$, C^-, CH^-, O^-, OH^-, C_2H^-, SiO_2H^-, and $Si(CH_3)O_2^-$. The effect

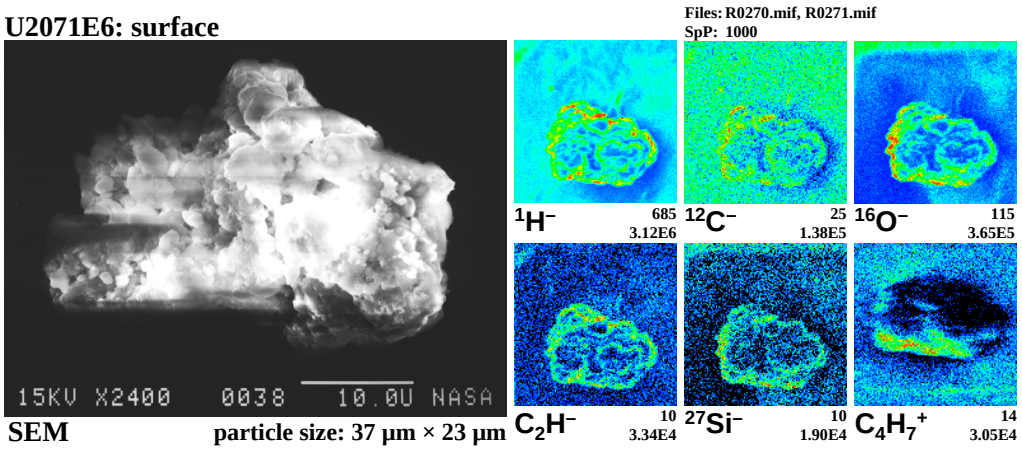

Figure 5.5: Field of view: $60 \times 60\,\mu m^2$; 128×128 pixels; no sputtering

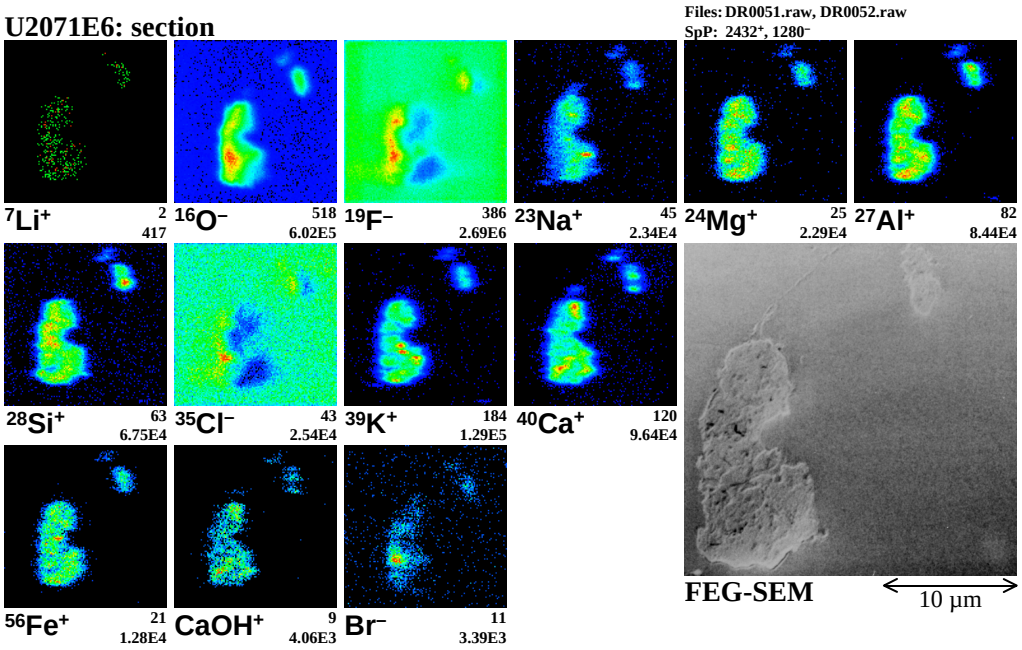

Figure 5.6: Field of view: $30 \times 30\,\mu m^2$; 128×128 pixels; no sputtering

of silicone oil on the analysis is also reflected in the quantitative evaluation (Table 5.3): C is at least 150 times more abundant than Si. The oil is possibly polymerized and therefore Si and O are strongly bound. On the other hand, the detachable methyl groups may combine to longer hydrocarbons, or they are further disintegrated into its constituents explaining thus the high C abundance (Rost, 1995).

PIXE bulk analysis. The derived bulk element concentrations correspond well with the SEM-EDS results from a smaller volume of analysis (Table 5.3), indicating a homogeneous element distribution in U2071E6.

Section analysis. Figure 5.6 shows the TOF-SIMS section analysis of U2071E6. The small spot in the upper right corner may also be a part of E6, because it shows the same elements than the main body. Probably some fragment broke off the particle when embedding it into epoxy.

Most elements show a very homogeneous distribution over the whole area of the particle (Li, Mg, Al, Si, Fe), or they are at least found everywhere but with varying abundances (O, Na, K, Ca). Only F and Cl are an exception. F and Cl are clearly enriched on the left side of the particle, close to its surface. Inside the particle only a $\sim 4\,\mu m$ wide stripe in its center shows minor amounts of these halogens. K is enriched in several submicrometer sized spots, one of them coinciding with higher Na abundances. Several $\sim 1\,\mu m$ sized Ca enrichments are found in correlation with CaOH indicating a phase bearing Ca and O. It is probably not CaOH, because H_2, the dominating residual gas, may be responsible for hydrides.

Generally, the TOF-SIMS derived abundance ratios are in good agreement with the respective SEM-EDS data (Table 5.3). Only Cl and Ti show a severe deviation: $1 \times CI_{Si}$ (SEM-EDS) and $10 \times CI_{Si}$ (TOF-SIMS) for Cl, $5 \times CI_{Si}$ (SEM-EDS) and $0.3 \times CI_{Si}$ (TOF-SIMS) for Ti.

Discussion. U2071E6 is the first nonspherical particle presented here and a short comparison with the model calculation (Chapter 3.5) seems reasonable. A shadow appears in accordance with the simulation (cf. Fig. 3.7b), whereas the secondary ions from the particle itself have distributions unlike the model sphere (cf. Fig. 3.7c, d). The reason lies in the irregular shape and rough surface of U2071E6. This results in 'ridges' all over the particle, where the primary ions impinge under oblique angles — thus producing local intensity maxima.

Considering the homogeneous element distribution in the particle as observed by TOF-SIMS, one can expect that TOF-SIMS and SEM-EDS result in similar element abundances, although the analyzed volumes are different. This is indeed found for most elements thus proving the reliability of TOF-SIMS within its inherent uncertainties.

The low Mg and Fe and high Al, K and Ca abundances found by SEM-EDS in the analyzed $2\,\mu m$ surface layer are confirmed by TOF-SIMS section analysis. This corroborates the conjecture of U2071E6 being a terrestrial basalt particle.

The halogen enrichment close to the surface on one side of the particle may indicate contamination.

5.3.2 U2071I9 (TCA)

SEM-EDS analysis. The 20 µm × 15 µm sized particle has a compact, irregular shape but smooth surface (Fig. 5.7). When picking the particle from the collector flag, a big adherent aerosol droplet was observed, however, it remained in the silicone oil (Stephan *et al.*, 1995). U2071I9 was classified as

	SEM-EDS		PIXE (bulk)		TOF-SIMS (surf.)		TOF-SIMS (sect.)	
E	[wt%]	$[E]_{Si,CI}$	[wt%]	$[E]_{Si,CI}$	E/Si [at]	$[E]_{Si,CI}$	E/Si [at]	$[E]_{Si,CI}$
Li					0.013	220	0.024	420
Be					280	3.8×10^8	5.8	7.9×10^6
B					0.4	20000	0.20	9600
C	4	50			3000	3900	22	28
C					4400	5900	1.9	2.4
O	51	44			43	5.7	590	78
O					460	60	230	31
Na	0.3	20			0.81	14	0.18	3.1
Mg	1.5	6.0			3.2	3.0	3.1	2.9
Al	6.9	310	4.2	230	5.1	60	16	190
Si	27	≡100	22	≡100	≡100	≡100	≡100	≡100
P	*0.5*	*200*			*5*	*400*		
S	4.6	29	5.8	45				
Cl	*0.1*	*60*	0.087	59	*0.005*	*0.9*	0.58	110
K	1.4	1000	1.4	1200	2.0	530	2.2	590
Ca	0.42	18	0.40	20	1.2	20	0.12	1.9
Sc							0.0017	51
Ti	*0.2*	*200*	0.44	480	0.53	220	0.35	150
V					*0.004*	*10*	0.0088	30
Cr					0.005	0.4	0.0086	0.64
Mn			0.01	2.4	0.04	4	0.030	3.1
Fe	2.1	4.4	2.4	6.0	4.9	5.5	7.4	8.2
Co							0.0019	0.85
Ni			0.0029	0.13			0.010	0.20
Cu			0.0070	27				
Zn			0.004	7				
Ge			0.003	40				
Rb					0.0071	1000	0.0062	870
Cs							0.00035	930
Ba							0.025	5600

Table 5.4: Element abundances in U2071I9. The average of three small area measurements is given for the TOF-SIMS surface analysis.

terrestrial artificial contamination according its elemental composition (Table 5.4) that does not match known cosmic particles. Its is rich in Al (6.9 wt%) and Si (29.9 wt%). Together with its glassy and rounded appearance, one can suppose that the particle has experienced an atmospheric entry. Since it is most probably not extraterrestrial, it could be a man-made relic of space technology. Therefore it was classified as TCA.

Surface analysis. Secondary ions from this particle are only produced at a small region near the left edge (Fig. 5.7). Remains of the hydrocarbon layer (H, C) are found on the outer rim. Be, Na, Mg, Al, Si, K, Ca, Ti, and Fe are predominantly coming from one $\sim 4\,\mu m$ sized area.

The most striking feature is the high occurrence of Be. The spectrum evaluation results in an elemental surface abundance almost three times as much as that of Si (Table 5.4). Dominated by some residual hydrocarbons (extraneous high C) and the Be, the TOF-SIMS derived surface composition cannot reasonably be compared with the SEM-EDS data.

PIXE bulk analysis. The derived bulk element concentrations closely match the results of SEM-EDS quasi-bulk analysis (Table 5.4). This points toward a homogeneous element distribution within U2071I9.

Section analysis. The major elements O, Mg, Al, Si, and Fe show a uniform distribution inside U2071I9 (Fig. 5.8). Especially Mg, Al, and Fe are entirely correlated. The Na and K distribution is approximately correlated, their secondary ion signals enriched in the same regions. Cl, Ca, and Ti are enriched in one ore more spots, with little correlation.

While the particle is rich in F relative to the surrounding epoxy, little Cl is coming from the particle — in contrast to the epoxy. Two thirds of the shown negative ions with nominal mass 32 u are $^{32}S^-$ ions, as can be deduced from the $^{34}S^-$ data by applying the natural isotopic ratio, the remaining third must be attributed to $^{16}O_2^-$.

The rare and light elements Li and Be also occur in U2071I9, especially Be is nearly as abundant as in the surface measurement (Table 5.4).

Discussion. The rare Be (CI abundance relative to Si: 7.3×10^{-7}; Anders and Grevesse, 1989) is enriched on the surfaces of many stratospheric dust particles in this study. Therefore it was proposed, that these Be enrichments may not be pristine (Rost, 1995; Rost *et al.*, 1999): A plausible explanation is a contamination during SEM-EDS analysis, where the particles lay on Be substrates. Often the particles stuck to the substrate after the measurements. The 15 keV electron beam probably 'glued' them onto the Be, possibly aided by silicone oil residues. When tearing off the particle to remove it from the substrate, some Be is likely to remain on its surface.

The finding of highly enriched Be throughout the particle in the section analysis may indicate an indigenous occurrence in U2071I9 that might by

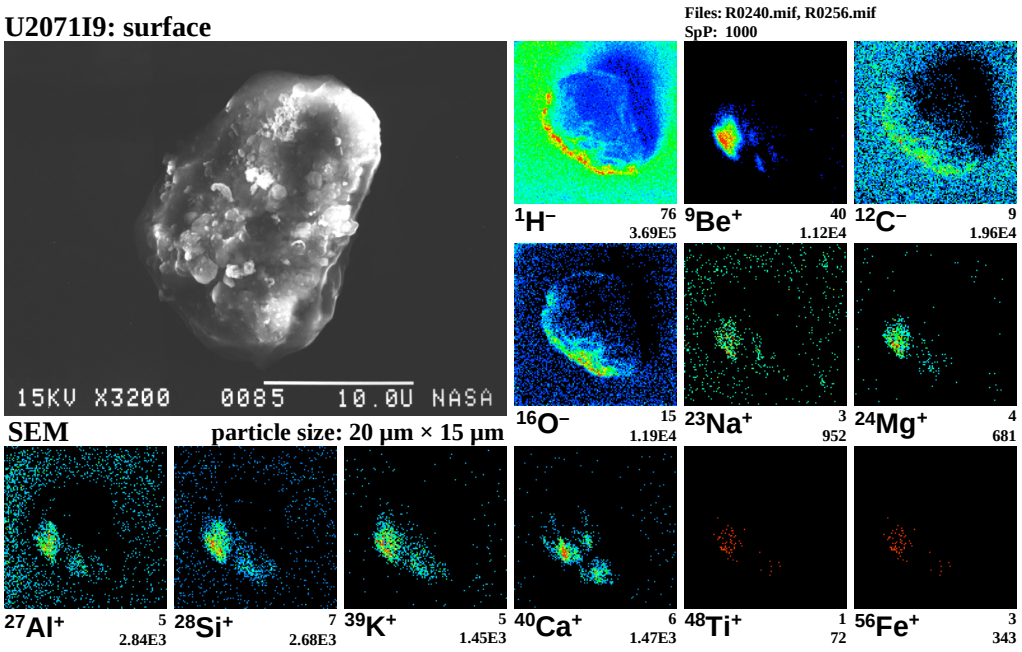

Figure 5.7: Field of view: $30 \times 30\,\mu m^2$; 128×128 pixels; no sputtering

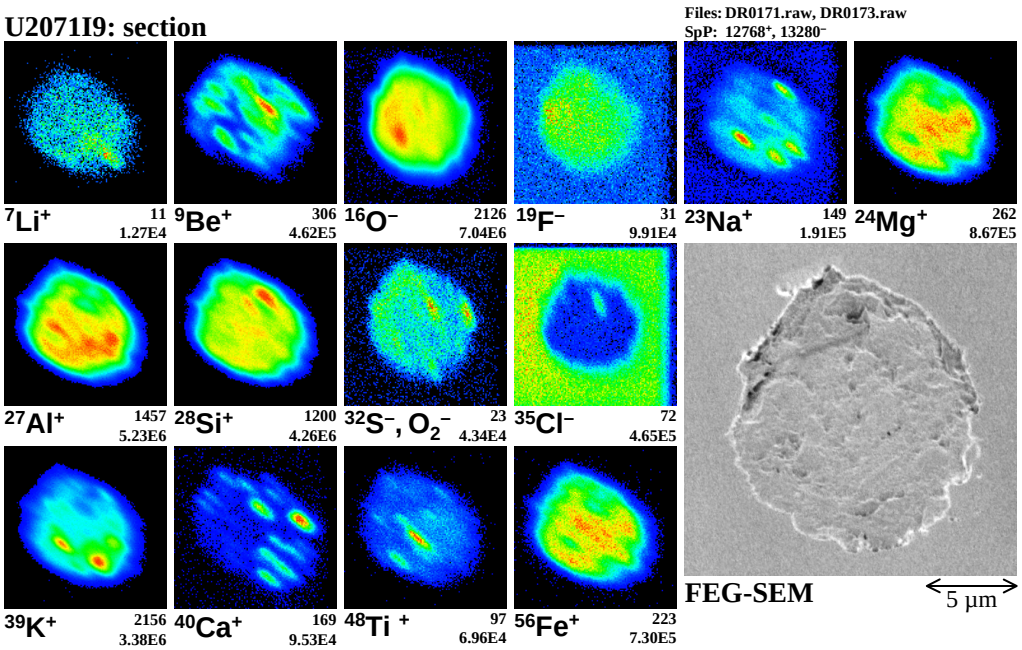

Figure 5.8: Field of view: $20 \times 20\,\mu m^2$; 128×128 pixels; with Ar sputtering

possible for this anthropogenetic particle. But taking the analyses of other particle surfaces (*e.g.*, U2072D1 and D4) into account, one should exclude the possibility that during the cutting of the particle some contaminating Be was smeared over the section plane.

The aerosol droplet, which was spotted in relation with the particle on the collector flag, caused no discernable contamination.

5.4 Type ?: U2071D1

SEM-EDS analysis. With a size of approximately 50 µm × 33 µm, U2071D1 (Fig. 5.9) is the largest of all selected particles from collector U2071. There it was found with attached aerosol droplets, which remained in the

	SEM-EDS		PIXE (bulk)		TOF-SIMS (surf.)		TOF-SIMS (sect.)	
E	[wt%]	$[E]_{Si,CI}$	E/Fe [wt]	$[E]_{Si,CI}$	E/Si [at]	$[E]_{Si,CI}$	E/Si [at]	$[E]_{Si,CI}$
Li					0.036	630	0.11	2000
Be					2.3	3.1×10^6	2.8	3.8×10^6
B					0.22	10000	0.30	14000
C	11	310			430	560	690	920
C					500	660	810	1100
O	46	94			290	38	810	110
O					430	56	430	56
Na	*0.1*	*30*			0.32	5.5	1.8	31
Mg	0.81	7.9	40	6	1.8	1.7	7.1	6.6
Al	3.4	370	200	330	17	200	15	180
Si	11.1	≡100	760	≡100	≡100	≡100	≡100	≡100
P					0.9	90		
P					*5*	*500*		
S	3.7	57	190	42.6				
Cl	*0.5*	*600*	16	330	17	3200	21	4000
K			27	670	0.90	240	3.4	900
Ca	22	2200	1580	2380	84	1400	71	1200
Ti	*0.1*	*200*	10	300				
V					*0.002*	*8*	0.013	45
Cr					0.08	6	0.011	0.80
Mn	*0.1*	*60*	5	40	0.08	8	0.26	27
Fe	1.6	8.3	≡100	7.36	0.76	0.85	5.0	5.6
Zn			14	630				

Table 5.5: Element abundances in U2071D1. The average of seven small area measurements is given for the TOF-SIMS surface analysis.

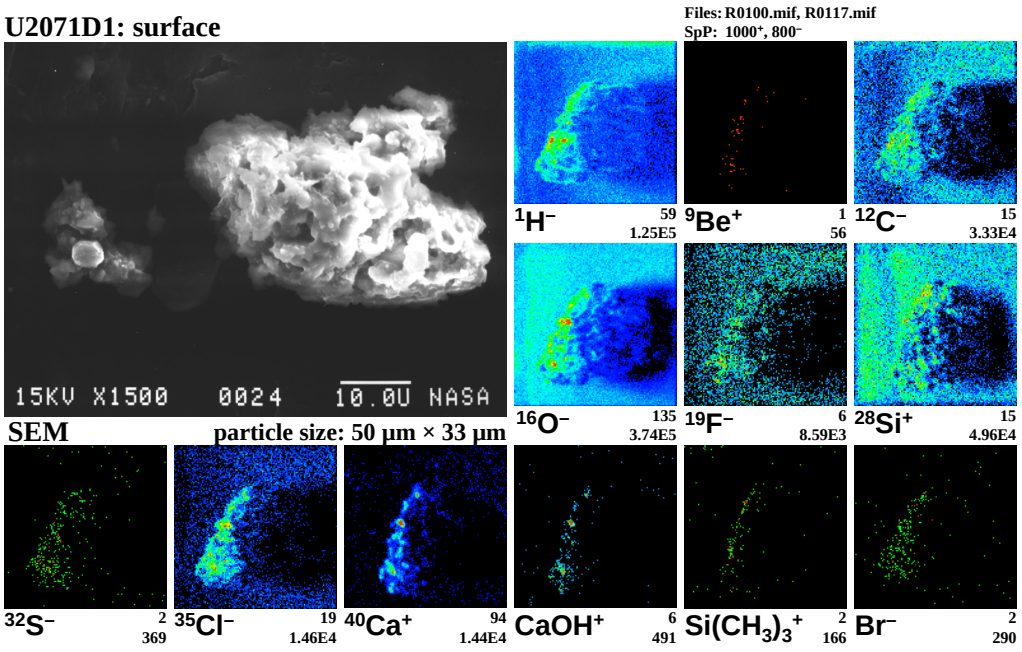

Figure 5.9: Field of view: $60 \times 60\,\mu m^2$; 128×128 pixels; no sputtering

silicone oil after picking the particle (Stephan *et al.*, 1995). It has a irregular shape. Preliminary classification from the SEM-EDS data (Table 5.5) was not possible. Its composition resembles neither known IDPs nor common terrestrial particles. It is very rich in Ca (22 wt%), C (11 wt%), and Al (3.4 wt%). The Si content of 11.1 wt% matches (by chance?) the 10.7 wt% of CI chondrites. Relative to CI abundances, Mg (0.8 wt%, $0.08 \times \mathrm{CI_{Si}}$) and Fe (1.6 wt%, $0.09 \times \mathrm{CI_{Si}}$) are severely depleted, whereas 3.7 wt% S, corresponding to $0.68 \times \mathrm{CI_{Si}}$, is typical for chondritic IDPs.

Surface analysis. The distribution of the silicone oil derivative $\mathrm{Si(CH_3)_3^+}$ indicates some minor residues on the surface (Fig. 5.9). They are no serious impediment for the surface analysis, although U2071D1 has a surface morphology comparable to U2071E6, of which the very surface was entirely obstructed. The composition of the surface, as derived from TOF-SIMS analysis (Table 5.5), qualitatively matches the SEM-EDS results: It is rich in C ($\sim 6 \times \mathrm{CI_{Si}}$), Al ($1.95 \times \mathrm{CI_{Si}}$), and Ca ($14 \times \mathrm{CI_{Si}}$) but low in Mg ($0.017 \times \mathrm{CI_{Si}}$) and Fe ($0.0085 \times \mathrm{CI_{Si}}$).

The halogens F, Cl, and Br could be detected on the surface, too. Element abundances can be evaluated for Cl giving an enrichment of $\sim 30 \times \mathrm{CI_{Si}}$.

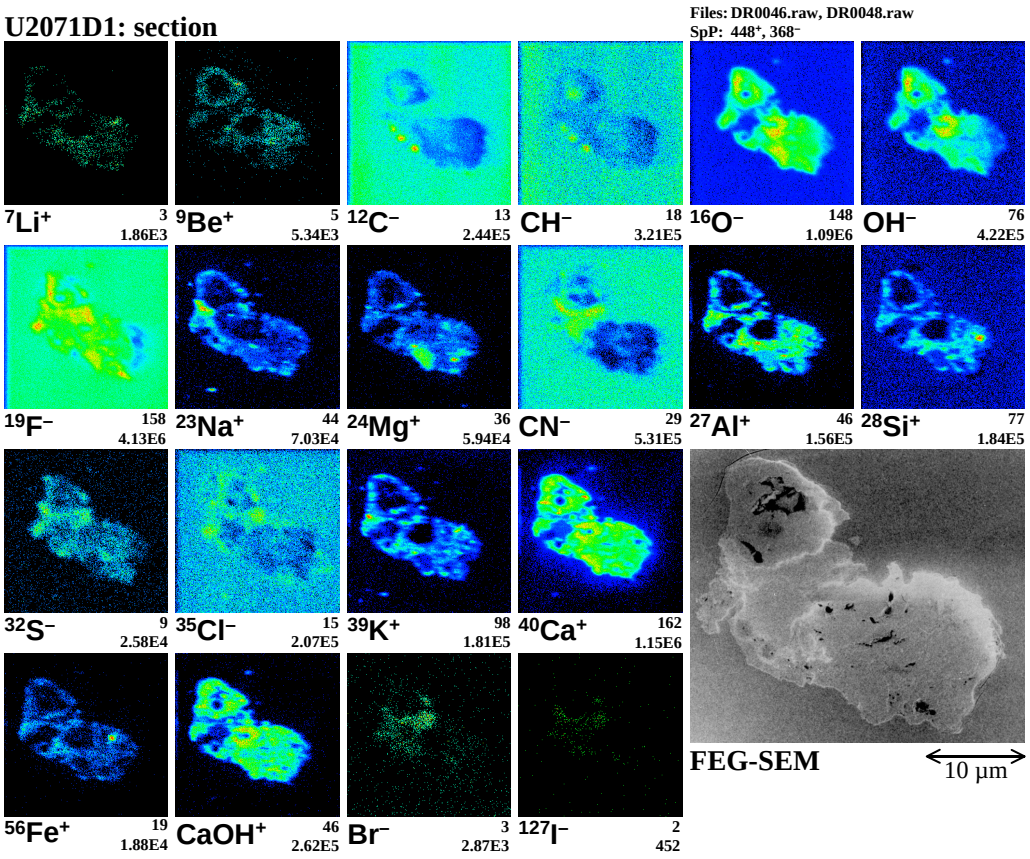

Figure 5.10: Field of view: $50 \times 50\,\mu m^2$; 256×256 pixels; no sputtering

The rare light elements Li, Be, and B are also detected. While Li is rather moderately enriched ($6.3 \times CI_{Si}$), Be ($31000 \times CI_{Si}$) and B ($100 \times CI_{Si}$) are very abundant.

TEM analysis. Phyllosilicates (saponite) and sulfates are identified as major phases. Some bubbles in the saponite indicate that the particle was heated to some extent. Smectite like saponite loses most of its interlayer water between 100°C and 250°C, so that U2071D1 should at least have experienced such temperatures. Generally, the phyllosilicates appear to be similar to those found in hydrated chondritic IDPs (Klöck and Nakamura, pers. comm.).

Section analysis. U2071D1 separates into two main parts, in which the main phases are arranged like onion shells. Around central cavities a Ca and O-rich phase resides, which contains no Al and Si, and only little Mg and Fe (Fig. 5.10). This phase is surrounded by Al-rich silicates and a S containing phase.

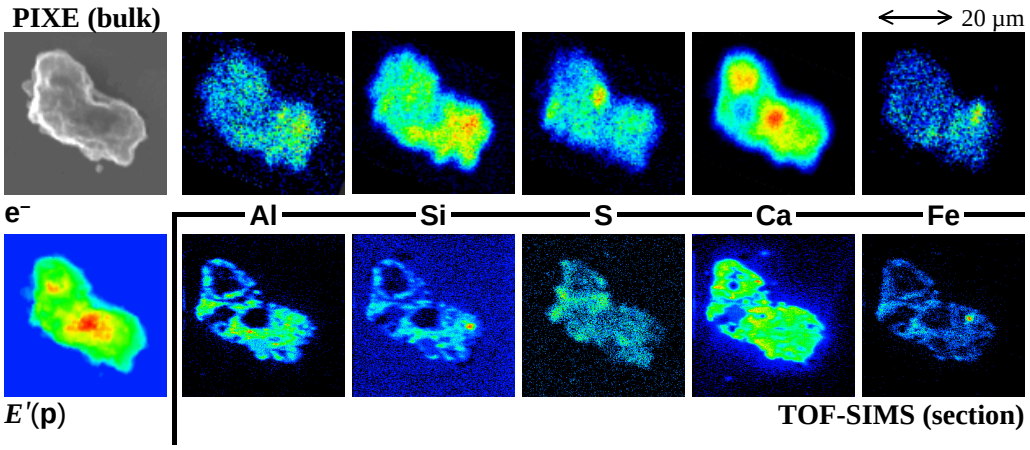

Figure 5.11: 2-dimensional distribution of the element concentrations in U2071D1 as derived from PIXE bulk analysis. For a better comparison the corresponding TOF-SIMS section results are repeated.

C and carbonaceous compounds are abundant between the two major segments. Here also S and the halogens F, Cl, Br, and I are found. Moreover, F and Cl occur in some other region on the verge of the particle.

PIXE bulk analysis. The PIXE derived images of element distributions (Fig. 5.11) resemble closely the results from the TOF-SIMS section analysis. By chance, the particle was equally orientated. According to the bimodal mass distribution (E'(p) in Fig. 5.11), the particle can be subdivided into two parts, consistent with the TOF-SIMS findings. In the centers of both segments high Ca concentration occur, which is a good proof of the above proposed onion shell structure of the particle. Here a clear anti-correlation for the other major elements like, *e.g.*, Si, cannot be observed and would not be expected, if the central Ca-rich phase is embedded in silicates. The PIXE measurement confirms a S-rich phase between the segments.

Discussion. The results obtained from U2071D1 with the different techniques are complementary. Around two central cavities, possibly resulting from heating, Ca is concentrated, surrounded by Al-rich silicate. Based on TOF-SIMS results, one can speculate on the nature of the Ca-rich phase. It is for sure, that it contains also O and is not a silicate. The most probable candidate is certainly carbonate (calcite: $CaCO_3$), although CO_3^{2+} ions or derivatives are not unambiguously identified. Other possibilities include portlandite, $Ca(OH)_2$, or CaO, which — if not indigenous — would result from portlandite or calcite after heating to $\sim$450°C or $\sim$900°C, respectively. Saponite, on the other hand, is unstable above 750°C, giving an upper limit for the heating event.

Between the two main parts of U2071D1, as observed in the section, a C and halogen rich phase occurs. It might be caused by contaminating silicone oil: If the particle shape is highly reentrant, this region of the particle section can represent surface material. In this case, the halogens and the sulfur may result from aerosols and the carbonaceous material from silicone oil. However, the SEM image shows a irregular particle but gives no clue to a shape of this kind. An alternative explanation is a pristine carbonaceous phase, into which the halogens and sulfur migrated, if they are not indigenous. The occurrence of a C-rich phase in U2071D1 is unavoidable to account for the 11 wt% C found with SEM-EDS.

Since F and Cl are also found in other spots related with the original particle surface, an extraneous origin of the halogens and S is more plausible.

Despite the rather exhaustive chemical studies, the origin of U2071D1, extraterrestrial of terrestrial, is still not clear. The findings prove a heating event in the history of the particle and indicate phyllosilicates resembling those in hydrated IDPs. These are clues pointing toward an extraterrestrial origin, but do not prove it.

Eventually, a nonchondritic type of Ca-rich IDPs, a type that is not recognized as such up to now, could solve the problem of the average Ca depletion (cf. Chapter 2.4). U2071D1 might be a representative of this type. To establish a new type unambiguously, at least in one specimen solar flare tracks must be identified. But the high probability of heating at atmospheric entry will usually ensure the annealing of these tracks.

5.5 IDPs (substrate: silicon wafer)

Etched silicone wafers (cf. Chapter 4.2) served as substrates for the TOF-SIMS surface analysis of the next four particles: U2071D4, E8, L1, and J9a. The particles lay on this substrate for rinsing off the silicone oil and during the following analysis. The oil could be satisfactorily removed and an analysis of the very surface was possible. However, minor amounts of silicone oil derived (molecular) ions are detected. The oil is probably responsible for a general C enrichment relative to SEM-EDS values, especially for positive ions.

5.5.1 U2071D4

SEM analysis. The particle has a size of 20 µm × 15 µm and a compact, irregular shape (Fig. 5.12). According to the SEM-EDS analysis (Table 5.6), U2071D4 is rich in Si (20 wt%, 1.9 × CI). Therefore, most other major elements are depleted relative to Si and CI. But also with regard to absolute element concentrations, Fe and Ni are depleted, 12 wt% (0.63 × CI) and 0.5 wt% (0.5 × CI), respectively. Mn is enriched to 7.8 × CI. This may indicate the occurrence of *LIME* silicates (Low Iron Manganese Enriched) in this IDP

	SEM-EDS		TOF-SIMS (surf.)		TOF-SIMS (sect.)	
E	[wt%]	$[E]_{Si,CI}$	E/Si [at]	$[E]_{Si,CI}$	E/Si [at]	$[E]_{Si,CI}$
Li			0.0023	40	0.0067	120
Be			3.1	4.2×10^6	0.088	120000
B			0.016	760	0.005	200
C	3	50	4.6	6.0	12	16
C			150	190	23	30
O	42	49	170	22	310	41
O			170	23	290	38
Na	1.8	190	8.8	150	20	350
Mg	9.9	54	15	14	29	27
Al	0.9	60	7.6	90	2.0	24
Si	19.6	≡100	≡100	≡100	≡100	≡100
P	*0.6*	*300*	0.14	13	0.52	50
P			*2*	*200*	*3*	*300*
S	6.7	59				
Cl	*0.1*	*80*	0.35	66	0.81	150
K			0.32	85	0.84	220
Ca	0.7	40	1.1	18	1.6	26
Sc					0.0017	48
Ti			0.029	12	0.049	20
V			0.0016	5.3	0.0046	16
Cr	0.4	80	0.34	25	0.60	44
Mn	1.6	420	1.0	110	3.4	350
Fe	12	34	11	12	9.8	11
Co			0.026	11	0.0031	1.4
Ni	0.5	30	0.75	15	0.085	1.7
Cu			0.096	180	0.003	5
Rb			0.0017	230	0.0013	180
Sr			0.0084	360	0.0012	50

Table 5.6: Element abundances in U2071D4

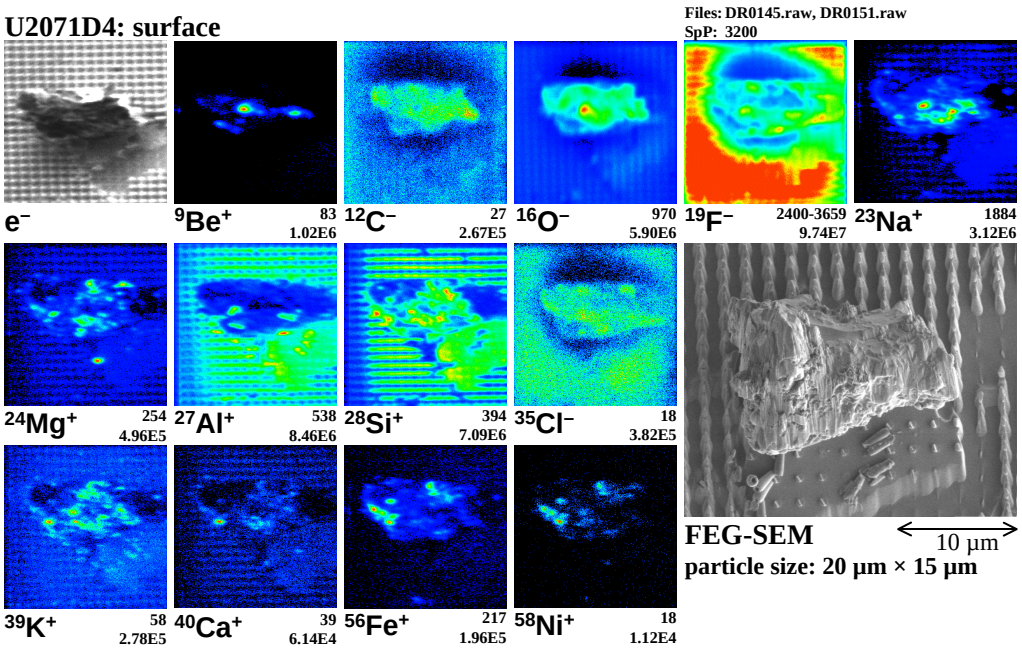

Figure 5.12: Field of view: $40 \times 40\,\mu m^2$; 128×128 pixels; no sputtering

(Stephan *et al.*, 1995). The compact morphology indicates that U2071D4 is a hydrated particle.

Surface analysis. The particle itself cannot be recognized in the 'light' of F, Al, and Si, because these ions come from the particle as well as from the substrate (Fig. 5.12): The Si wafer is rich in Al, F and its compounds, a result from the etching process. Even molecular ions like AlF_4^- and $Al_2F_7^-$ can be detected.

The halogens F and Cl have a similar intensity distribution on the surface of the particle, resembling also the one of the major element O.

The depletion of the major elements relative to Si and CI, except Mn, is also reflected in the TOF-SIMS surface analysis (Table 5.6).

Be is very abundant is concentrated in two spots. This can be associated with an exposed ridge (cf. the e^- image in Fig. 5.12).

TEM analysis. Phyllosilicates are identified indicating that U2071D4 is a hydrated IDP.

Section analysis. The distribution of the major elements in U2071D4 (Fig. 5.13) shows two main silicate phases. One is the principal host phase of Na, K, and Fe, whereas Li, Mg, Ca, and Cr occur in another phase. The Si signal is weaker in the latter one, indicating either a lower abundance or

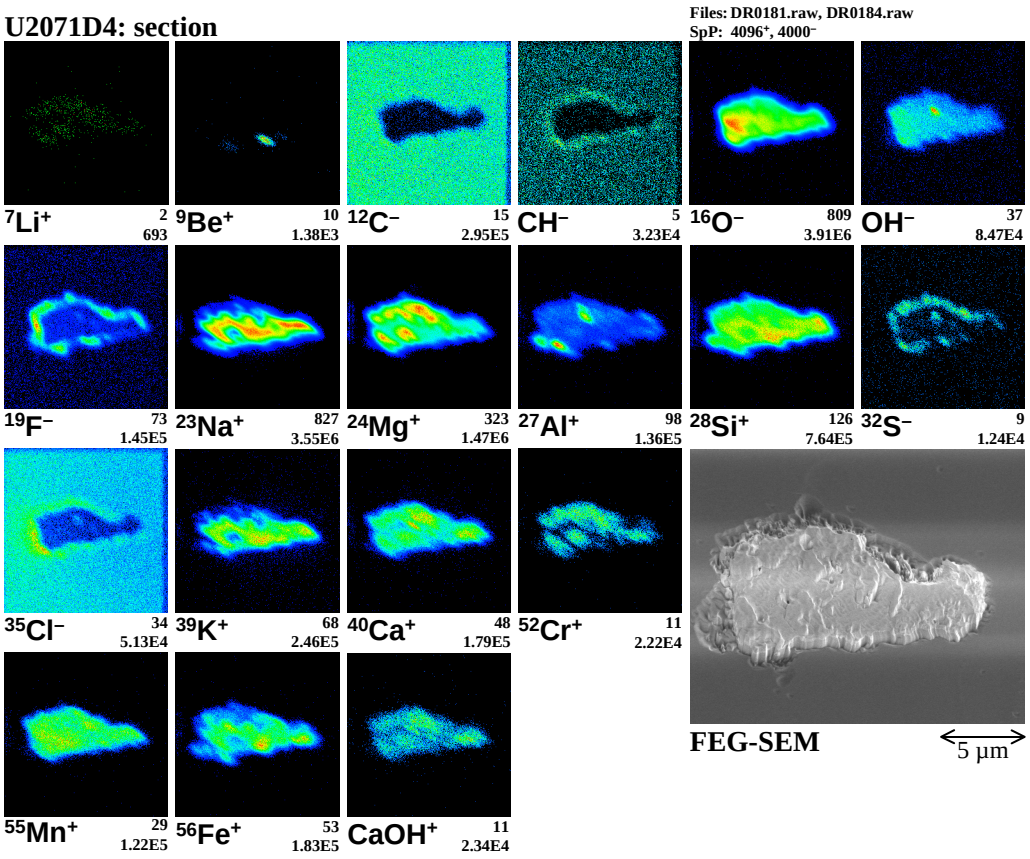

Figure 5.13: Field of view: $25 \times 25\,\mu m^2$; 256×256 pixels; with Ar sputtering

a matrix effect that arises from a different chemical environment of Si in the two phases.

Al is concentrated in two small areas. First, a micrometer sized phase in the center, where it is correlated with Ca, some S, and minor amounts of F and Cl. Second, it occurs in a somewhat larger phase at the lower left side of the particle.

Mn is rather homogeneously distributed inside the particle.

The halogens F and Cl, as well as S occur in a rim around the particle. This can be associated with a fringe visible in the FEG-SEM image, formed by roughened epoxy surface. It is more marked on the top and left side of the particle and looks like the impression of fragments that broke out of the particle during sectioning. This phenomenon was also observed in sections of two other particles, U2071E8 and L1. All three are cut within two days after embedding. Therefore, it may be that the epoxy was not entirely set at cutting time, but strained in a way that it withdrew a small distance from

the particle. With the primary ions coming from right, the rim on this side had to be associated with the very particle surface, whereas on the left side the withdrawn epoxy, formerly in contact with the particle surface, would be responsible for the rim.

In both cases the halogens and the sulfur originate directly or indirectly from the very surface of the IDP. This is also indicated by the distribution of Mg, Al, Si, and Fe, which outline the rim as seen in the FEG-SEM image.

Be is concentrated to a micrometer sized spot at the original surface of the particle.

Discussion. LIME olivine (Brownlee and Wheelock, 1985) and pyroxene are found in hydrated, as well as in and anhydrous IDPs. They are probably unequilibrated solar nebula condensates (Klöck *et al.*, 1989), *i.e.*, primitive material dating back to the formation of the solar system.

The TEM results indicate that U2071D4 is a hydrated IDP and consequently phyllosilicates represent the main phase. In such particles LIME phases occur only as accessorial mineral. But concluding from the uniform Mn distribution in U2071D4, Mn is incorporated in the main phase, *i.e.*, phyllosilicate. Although this finding is contrary to the original assumption, it may be interpreted as formerly abundant LIME silicates that did not survive the aqueous alteration commonly assumed for hydrated IDPs.

The finding of F and Cl with a secondary ion distribution on the surface similar to O indicate that the halogens uniformly occur on the whole surface, and that their intensities are only modulated by the surface morphology.

The detected high abundance of Be is limited to a spot on the surface and can be explained by contamination during SEM analysis.

S and most of the observed halogens are correlated with the original particle surface. Contamination by aerosols in the stratosphere is the simplest way to achieve this.

5.5.2 U2071E8

SEM analysis. This compact particle is equidimensional and has a size of 17 µm. It turned out to be very heterogeneous even in the SEM-EDS analysis: apart from chondritic material, two (Fe,Ni)S grains are found on the surface, as well as an Fe-rich phase (Stephan *et al.*, 1995). Ni is enriched to $13 \times \mathrm{CI}_{\mathrm{Si}}$. The volatile elements P, S, and Cl are also abundant: $3 \times \mathrm{CI}_{\mathrm{Si}}$, $2.4 \times \mathrm{CI}_{\mathrm{Si}}$, and $6 \times \mathrm{CI}_{\mathrm{Si}}$, respectively (Table 5.7).

Surface analysis. This particle shows a disadvantage of using etched silicon wafers as substrate: Needles, which broke off during positioning of the IDP, spread over the particle during the hexane rinsing and adhered to the surface. They can be spotted directly in the FEG-SEM image. High

	SEM-EDS		TOF-SIMS (surf.)		TOF-SIMS (b.)		TOF-SIMS (i.)	
E	[wt%]	$[E]_{Si,CI}$	E/Si [at]	$[E]_{Si,CI}$	E/Si [at]	$[E]_{Si,CI}$	E/Si [at]	$[E]_{Si,CI}$
Li			0.0031	55	0.0058	100	0.0011	20
Be			0.027	37000	0.0011	1600	*0.0004*	*600*
B			0.13	6100	0.081	3800	0.12	5500
C	7	200	170	220	79	110	100	140
C			2300	3000	76	100	96	130
O	30	74	1500	190	1000	130	1100	140
O			190	25	260	34	340	45
Na	1.4	310	5.6	98	9.4	160	9.6	170
Mg	6.5	75	29	27	51	47	34	32
Al	0.7	100	40	470	6.5	76	6.4	75
Si	9.3	≡100	≡100	≡100	≡100	≡100	≡100	≡100
P	*0.3*	*300*	*3*	*300*	0.4	40	*0.4*	*40*
P					*2*	*200*		
S	11.2	204						
Cl	*0.4*	*600*	79	15000	7.9	1500	20	3800
K			0.27	71	0.33	88	0.21	56
Ca			0.46	7.5	0.52	8.6	0.090	1.5
Sc					0.0021	63	0.013	390
Ti			0.042	18	0.16	66	0.49	200
V					0.017	60	0.038	130
Cr			0.27	20	1.0	74	4.1	310
Mn			0.30	31	0.26	27	0.24	25
Fe	20	120	23	26	31	34	92	100
Co			0.059	26	0.071	32	1.2	530
Ni	12.8	1340	3.1	63	1.5	30	16	320

Table 5.7: Element abundances in U2071E8. Results from two TOF-SIMS section analyses are given: (b.) the bulk silicate phase, (i.) the smaller, Fe-rich silicate phase.

secondary ion intensities of F^-, Al^+, and — the most distinguishing mark — compounds of them like AlF_4^- indicate their presence in the TOF-SIMS surface analysis (Fig. 5.14). About one half of the particle surface is obstructed in this way. These regions were excluded for the evaluation of the abundance ratios. The Al enrichment to $4.71 \times CI_{Si}$ (Table 5.7) probably indicates, that this could not be achieved thoroughly.

These needles must also be considered in the discussion of other secondary ion distributions. Additionally to F and Al, which predominantly stem from the needles, C, O, and Si originate from the needles and from the particle itself. The elements Na, Mg, Cl, K, Ca, Fe and Ni are mainly coming from

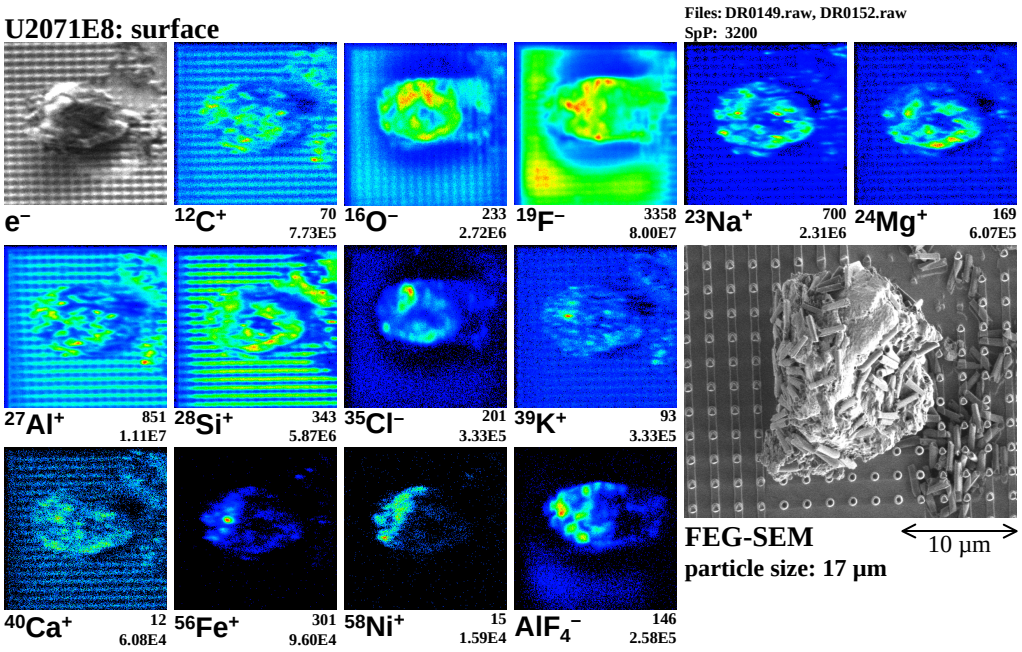

Figure 5.14: Field of view: $40 \times 40\,\mu m^2$; 256×256 pixels; no sputtering

the very surface of U2071E8. Most of these elements are found on the whole accessible surface, probably just modulated by the surface morphology. Cl, on the other hand, is enriched in a $4 \times 7\,\mu m^2$ sized area. Fe and Ni occur mainly in an area on the left side of the particle. This can be indicative of the Fe-rich phase found during SEM analysis.

Section analysis. FEG-SEM and TOF-SIMS analysis reveal three distinct areas (Fig. 5.15): First, there is a silicate phase occupying three quarters of the section and representing the bulk material particle. Some micrometer sized Ca-rich phases occur within the silicate, with Si being less abundant there. They are correlated with Mn and anti-correlated with Al.

On the right side of U2071E8, there is a smaller silicate phase, which is distinctly enriched in Fe and Ni relative to the bulk phase. Furthermore, Ca-rich phases do not occur.

Both silicates are separated by a phase that contains only Fe, Ni, and S in significant amounts. This certainly points to a sulfide, as was identified before on the surface of this IDPs with SEM.

The distribution image of S^- ions is almost complementary to the S^+ image: Positive sulfur ions arise from the sulfide, whereas the negative ions predominantly stem from the silicates.

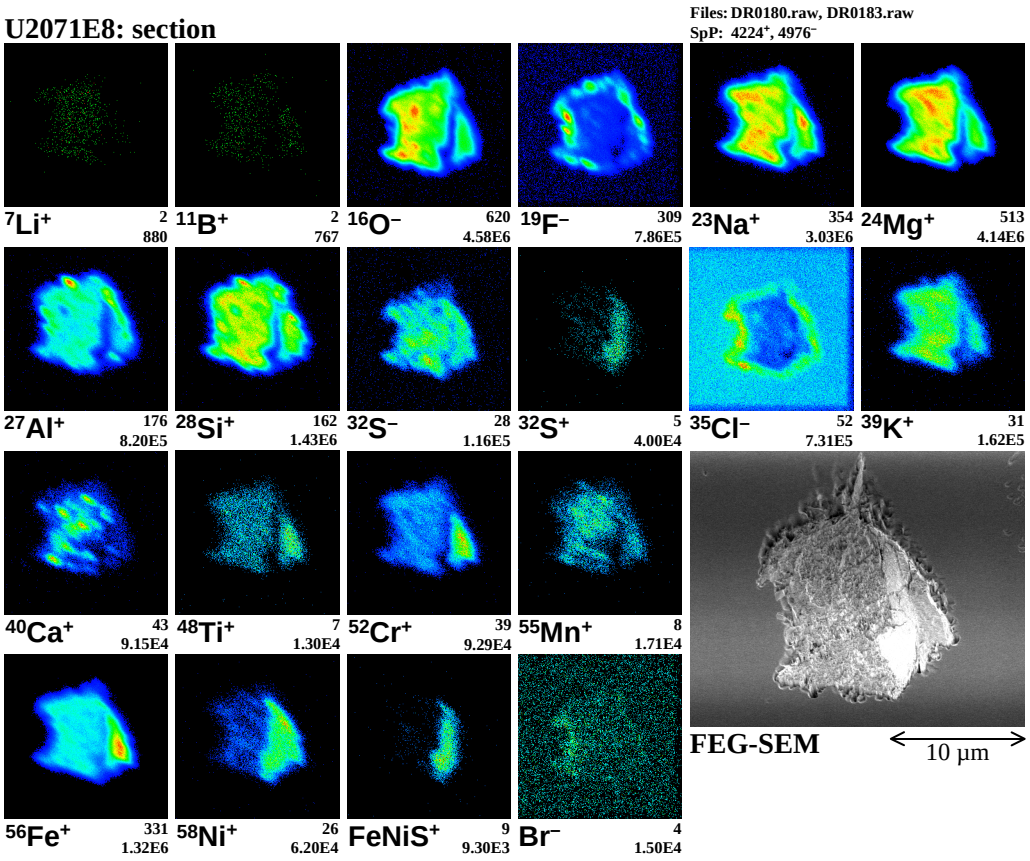

Figure 5.15: Field of view: $30 \times 30\,\mu m^2$; 256×256 pixels; no sputtering

Figure 5.16 shows the composition of the Fe-rich and the S-rich phases relative to the bulk silicate as secondary ion intensity ratios, corrected for the area size of the respective phases. Since the plotted data is derived from the same measurement of positive secondary ions, the element abundances can be compared. Concerning the sulfide phase, some elements (Mg, Al, Si, Ca) are similarly depleted by a factor of ~ 5, which may indicate a contribution from the surrounding silicates that could not be entirely excluded because of the limited lateral resolution. This phase show a high secondary ion signal of (positive) S ions and compounds that bear S, Fe, and Ni. The composition of the bulk and the Fe-rich silicate are also quantitatively given in Table 5.7. The evaluation of the sulfide phase is not possible, because here it is neither reasonable to normalize to the extraneous Si nor to apply the relative sensitivities derived for silicates. Concerning the silicates, most major elements, *e.g.*, O, Mg and Al, have similar abundances, except Fe: The Fe content is $0.34 \times CI_{Si}$ in the bulk silicate but chondritic in the smaller phase.

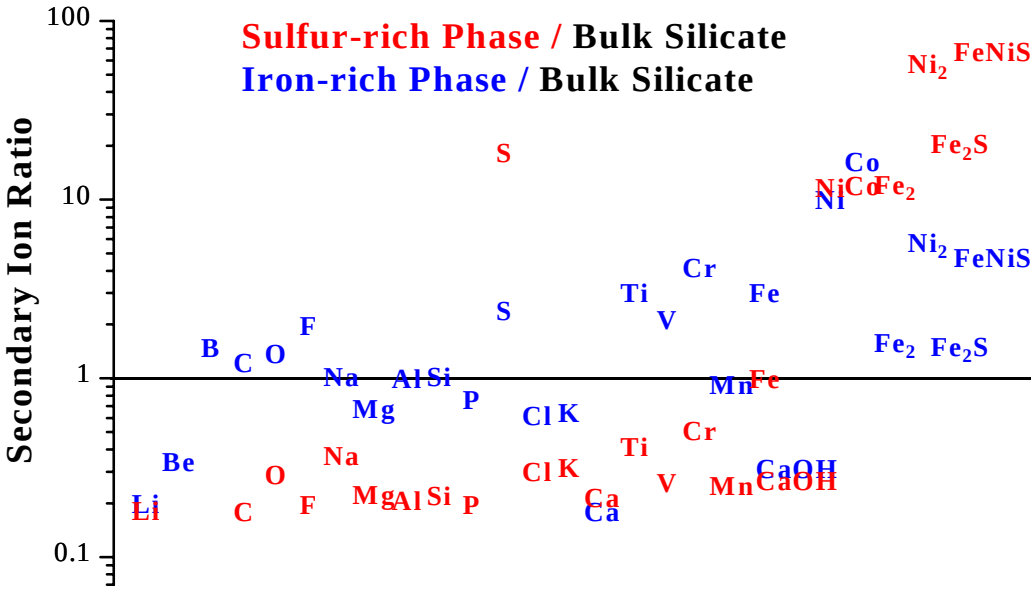

Figure 5.16: The differences in secondary ion ratios between the three main phases found in the section of U2071E8 are shown for the two smaller phases relative to bulk silicate.

Other metals, *e.g.*, Ti, V, Cr, Co, and Ni, show the same behavior: They are depleted to ~ 0.3–$0.7 \times \mathrm{CI_{Si}}$ in the bulk — and chondritic or enriched in the other silicate. The opposite applies for Li: It is chondritic in the major silicate but depleted to $0.2 \times \mathrm{CI_{Si}}$ in the other.

The halogens F and Cl are coming predominantly from a rim around the particle, similar to U2071D4. Again, the FEG-SEM image indicates that particle material broke out during cutting at the corresponding locations, especially on the top side of the particle. Though the Br image suffers from statistical noise, a correlation with the Cl and F-rich rim on the left side of the particle can be noticed.

Discussion. The small Ca-rich phases within the bulk silicate are probably carbonates, because they are correlated with Mn that is frequently found in carbonates partly substituting the Ca.

The complementary distribution of the positive and negative S secondary ion signal can only be explained by the very distinct chemical environment of S in the sulfide or the silicate. However, in other sulfides (*e.g.*, in U2071B6) also S^- prevails.

One can try a rough estimate of the metal composition in the sulfide by using the ratio of the relative Ni sensitivity factor to the relative Fe sensitivity factor, which are known for silicates (Fig. 3.5), resulting in an approximated

Ni sensitivity relative to Fe. An abundance ratio of 1 : 0.62 for Fe : Ni is hereby obtained. In chondritic interplanetary dust particles only pentlandite, $(Fe,Ni)_9S_8$, contains such a high portion of Ni (Zolensky and Thomas, 1995; Klöck, 1999). Taking the stoichiometry of pentlandite for granted, one ends up with 33 at% (40 wt%) Fe, 20 at% (26 wt%) Ni, and 47 at% (33 wt%) S. This is a typical composition for pentlandite phases in hydrated chondritic IDPs (*ibidem*). Unusual is the size of 10 µm × 2 µm — usually sulfides in chondritic IDPs are smaller than a few micrometers.

This compact and probably hydrated IDP bears two silicate phases with approximately equal major element abundances but varying occurrences of minor and trace elements. This unequilibrated appearance is interesting, because it had to sustain a hydrothermal alteration on the parent body that is supposed for hydrated IDPs.

Most of the detected halogens are related with the outer surface of U2071E8, and thus are due to stratospheric contamination.

5.5.3 U2071L1

SEM analysis. This equidimensional and compact particle has a size of 15 µm and a rough surface (Fig. 5.17). The elemental composition of this compact IDP is typical for chondritic IDPs (Table 5.8). Mg is slightly depleted to $0.71 \times CI_{Si}$, whereas Fe is enriched to $1.5 \times CI_{Si}$. Ca is depleted to $0.3 \times CI_{Si}$, which is quite common for chondritic IDPs, and the low S abundance of $0.35 \times CI_{Si}$ may indicate a loss during the atmospheric entry of the particle.

Surface analysis. AlF_4^- is enriched in several spots (Fig. 5.17), indicating again broken off needles. Actually, they can be perceived in the FEG-SEM image of the particle. Unlike U207E8, only two of them are lying on the surface. In the TOF-SIMS images of F and AlF_4^- they can be identified with the intense spot on the left side of the particle and a less conspicuous at the top side. The two AlF_4^- spots on the right side of U2071L1 are caused by needles lying beside the particle.

Most elements appear uniformly distributed on the surface, just modulated by topographic effects. Be emerges only from three micrometer sized spots. They probably represent exposed surface points (cf. the e^- image in Fig. 5.17), which had contact to the Be substrate in the SEM-EDS measurement.

Ca is concentrated in a spot on the left side of the particle. In an second measurement this region was studied in greater detail (Fig. 5.18): Ca is correlated with O, P and the oxide ions PO^-, PO_2^-, and PO_3^-. Only PO_2^- is

	SEM-EDS		TOF-SIMS (surf.)		TOF-SIMS (sect.)	
E	[wt%]	$[E]_{Si,CI}$	E/Si [at]	$[E]_{Si,CI}$	E/Si [at]	$[E]_{Si,CI}$
Li			0.0064	110	0.0011	19
Be			0.0062	8500	0.012	17000
B			0.021	1000	0.015	690
C	3	70	33	44	46	61
C			130	170	44	58
O	34	58	1300	180	1100	140
O			270	35	410	54
Na	0.9	200	7.2	130	5.2	90
Mg	8.3	68	49	45	68	63
Al	1.6	140	15	180	13	150
Si	13.2	≡100	≡100	≡100	≡100	≡100
P	*0.5*	*300*	4.3	410	2.2	210
P			2.7	260	*3*	*300*
S	2.3	29				
Cl	*0.05*	*60*	2.7	520	6.3	1200
K			0.42	110	0.47	120
Ca	0.36	31	1.1	17	1.9	31
Sc			0.0017	51	0.0036	100
Ti			0.15	62	0.20	84
V			0.0099	34	0.015	50
Cr	0.2	70	0.63	47	1.0	77
Mn	0.2	80	0.45	47	0.80	84
Fe	34	150	43	48	110	120
Co			0.10	46	0.23	100
Ni	1.7	120	2.1	44	3.6	72
Cu			0.062	120		
Rb			0.0014	200		
Sr			0.0092	390		

Table 5.8: Element abundances in U2071L1

shown, because it occurs with the highest intensity. These findings indicate a phosphate, *e.g.*, apatite, $Ca_5(PO_4)_3(F, Cl, OH)$, or whitlockite, $Ca_3(PO_4)_2$.

Section analysis. In Figure 5.19 element distributions from the section analysis of U2071L1 are presented. The color assignment in the O^- distribution image was adjusted to make details visible inside the particle. The lower left O and Ca-rich material is of unknown origin, not related to the particle and will not be discussed.

The bulk material may be attributed to phyllosilicates form, as usual for compact (hydrated) IDPs. Two silicate grains with diameters of about one micrometer are conspicuous because of their enrichments in O and Mg,

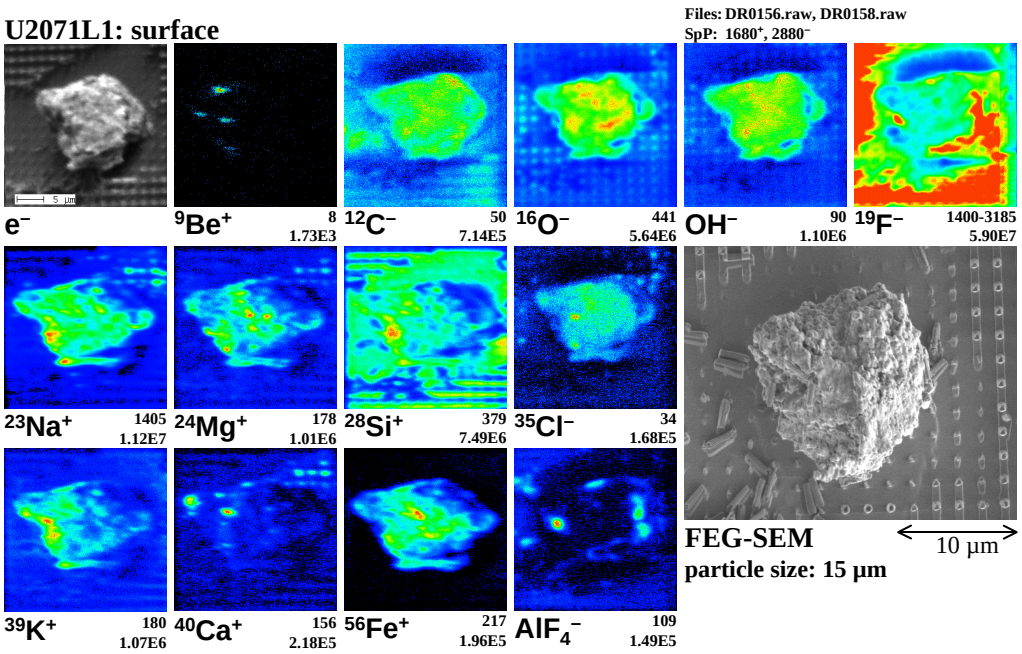

Figure 5.17: Field of view: $30 \times 30\,\mu m^2$; 256×256 pixels; no sputtering

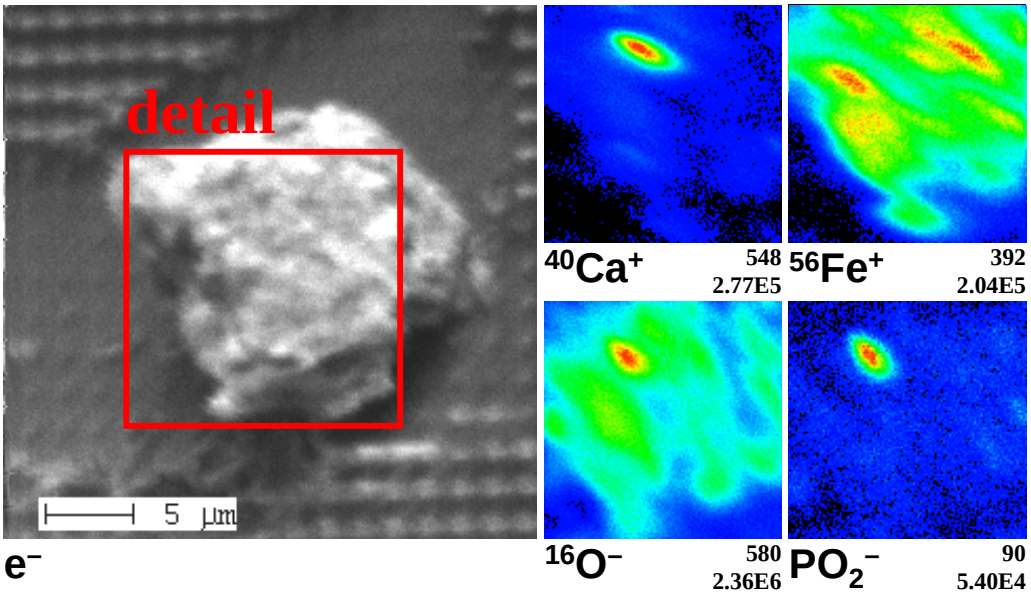

Figure 5.18: Presumed apatite grain on the surface of U2071L1

the lack of Al, and low abundance of Fe. These grains probably consist of forsterite, Mg_2SiO_4, or enstatite, $Mg_2Si_2O_6$, which are sometimes accessory minerals in hydrated IDPs.

Most elements are uniformly distributed over the particle's section plane. Na is enriched in a broad rim around the particle and depleted in the center, a so far unique observation.

The halogens F and especially Cl are enriched in a narrow rim around the particle, which is apparent also in the FEG-SEM image. The highest intensities of F are coming from three small areas coinciding with gaps in the Cl rim. In one case F is clearly correlated with Al and indicates a surface adherent needle from the wafer.

O, Ca, and phosphorous oxides like PO_2 coincide in five micrometer sized spots inside the particle. Figure 5.20 shows an intensity profile through two of these phosphates as indicated in the Ca distribution image. F is clearly enriched in the grains relative to the surrounding. Cl shows a similar but less pronounced trend. O, Ca, and PO_2 are enriched in these grains, Si is depleted, but not entirely absent. The observation of Ca and halogens favors apatite. The phosphates may be intergrown with the surrounding silicate on a submicrometer scale.

Be is found in a small spot close to the original surface of the particle.

Discussion. There are two contrary explanations of the observed surface related Na enrichment. First, the Na got into the particle from outside, possible through dissolved salt (NaCl) in aerosol droplets. The second explanation implies that U2071L1 was rich in water bearing phyllosilicates before being captured by the Earth. Then, during the atmospheric entry heating, inter-layer water evaporated on the surface leaving behind the otherwise well soluble Na, now deposited and enriched in the surface near material. Here, a further characterization by TEM should reveal an alteration of minerals by entry heating and settle this question.

Phosphates like apatite are a result of aqueous alteration. They are found as accessory phases in many meteorites including chondrites. However, phosphates are rare minerals in IDPs. One other phase could be found before in IDP L2006E10, again during TOF-SIMS section analysis (Stephan *et al.*, 1994c). This finding is not a sufficient criteria for U2071L1 originating from one of the chondrite parent bodies, but may indicate a similar history. Future, detailed TEM analyses will clarify to what extent U2071L1 can be related to certain meteorite classes.

The surface bound halogens are again contradictory to an indigenous origin.

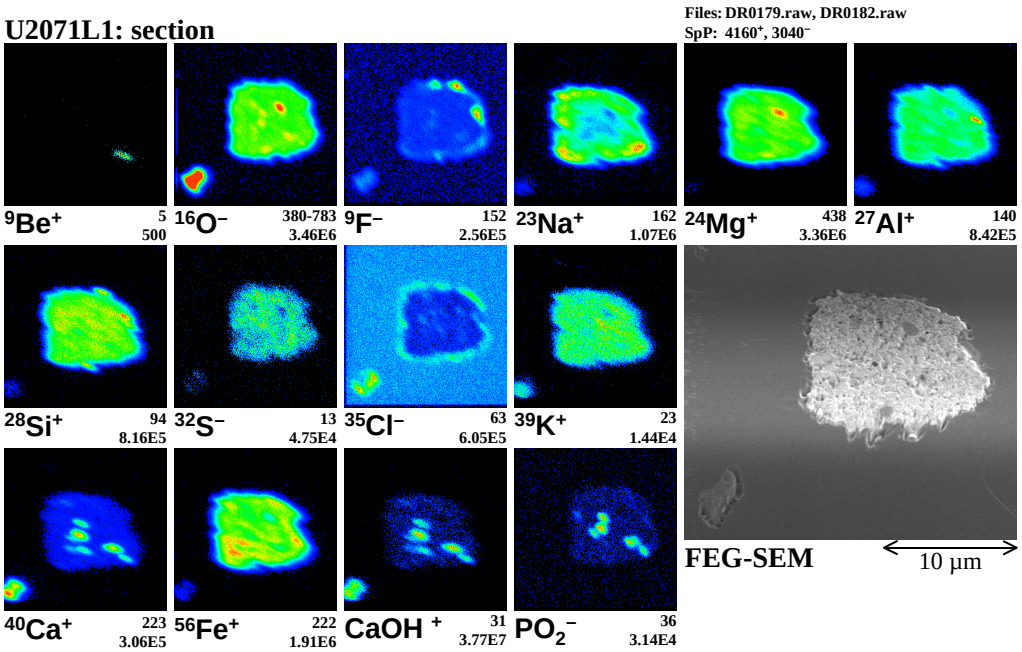

Figure 5.19: Field of view: $30 \times 30\,\mu m^2$; 256×256 pixels; with Ar sputtering

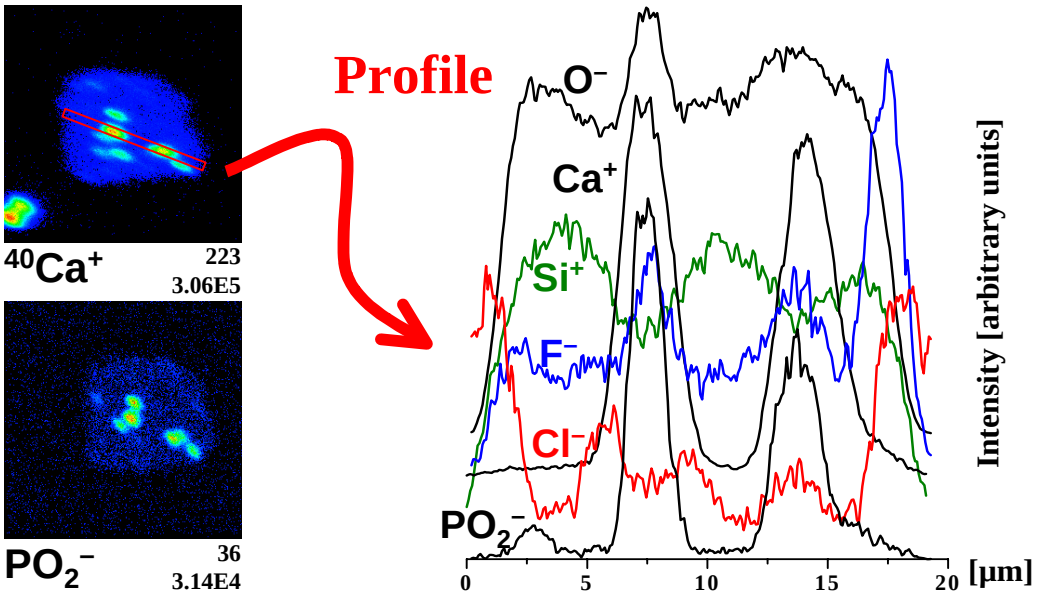

Figure 5.20: Profile through presumed apatite grains in U2071L1. Secondary ion intensity are given in arbitrary units.

5.5.4 U2071J9a

SEM analysis. This originally collected particle broke apart during the first hexane rinsing. The fragments were designated with U2071J9a and J9b. They are both irregularly shaped particle, 12 µm × 10 µm and 12 µm × 7 µm in size. Their surface morphology is rough to fluffy and they were classified as cosmic particles. U2071J9b broke into another two pieces after SEM analysis and J9a disintegrated during the preparation for the TOF-SIMS surface analysis. Only some tiny fragments of U2071J9a could be transferred onto the substrate, with the largest one being about 3 µm × 2 µm in size (cf. Fig. 5.21).

	SEM-EDS		TOF-SIMS (surf.)	
E	[wt%]	$[E]_{Si,CI}$	E/Si [at]	$[E]_{Si,CI}$
Li			0.0033	57
Be			0.011	1500
B			0.021	1000
C	7	130	30	40
C			220	290
O	36	50	450	60
O			170	23
Na	0.7	100	2.5	44
Mg	10.6	70	37	34
Al	1.7	130	20	240
Si	16.5	≡100	≡100	≡100
P	*0.7*	*400*	0.9	80
P			1.5	140
S	5.5	56		
Cl	*0.1*	*100*	0.64	120
K			0.27	71
Ca	2.7	190	1.0	17
Ti			0.050	21
V			0.003	10
Cr	0.3	70	0.42	31
Mn	*0.1*	*40*	0.23	24
Fe	17	57	8.0	8.9
Co			0.017	8
Ni	1.3	76	0.57	12

Table 5.9: Element abundances in U2071J9a. The TOF-SIMS surface measurement was only performed on a fragment of this IDP.

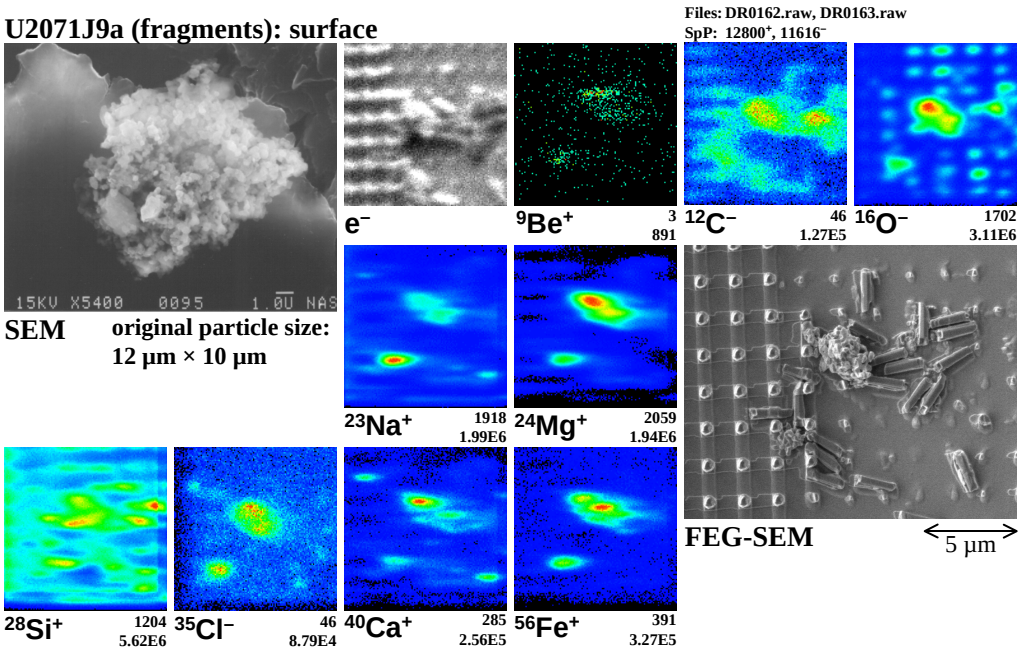

Figure 5.21: Field of view: $15 \times 15\,\mu m^2$; 128×128 pixels; no sputtering

U2071J9a is enriched in Si to $1.5 \times$ CI corresponding to 16 wt% . Because of the normalization to Si in the $[E]_{Si,CI}$ column, here most elements are depleted. Actually, the composition of the J9a and J9b is approximately chondritic, even in S. Both fragments are equally rich in P: $6 \times CI_{Si}$. U2071J9b is depleted in Ca ($0.6 \times$ CI), whereas J9a is enriched ($3 \times$ CI), so that for the original particle a Ca abundance of $\sim 2 \times$ CI follows. This is unusual, because most chondritic IDPs are depleted in Ca (Schramm *et al.*, 1989; Arndt *et al.*, 1996b).

Surface analysis. Two fragments of U2071J9a can be perceived in the FEG-SEM image and in the secondary ion images of O, Na, Mg, Cl, Ca, and Fe (Fig. 5.21). The larger one in the center has a size of $3\,\mu m \times 2\,\mu m$ and the smaller one, on the left side below, has a diameter of $\sim 1\,\mu m$.

The TOF-SIMS derived abundances of the larger fragment (Table 5.9) are not corresponding well with the SEM-EDS results or chondritic abundances.

The results may be somewhat falsified by the surrounding substrate material, which could have contributed because of the limited lateral resolution. This explanation is supported by the relative high content of Al ($2.4 \times CI_{Si}$), which is very abundant on the etched silicon wafer.

The Ca abundance seems to be only $0.17 \times CI_{Si}$, about 10 times lower than from the SEM-EDS. Probably Ca was distributed heterogeneously within J9a,

which is also suggested by its enrichment in the upper left region of the larger fragment.

C and Si stem from the fragments, but also from the surrounding substrate. Be is found everywhere on the surfaces of both fragments and is probably due to the Be substrate.

Section analysis. The fragments on the silicon wafer were too small for a further preparation and were lost.

Discussion. The precursor IDP of U2071J9a and J9b was a very fragile chondritic IDP, possibly a chondritic porous particle. Together with the fact that it survived atmospheric entry indicates a low atmospheric entry velocity and/or an oblique entry angle to ensure a gentle deceleration.

The particle was rich in Ca, similarly to U2071D1, which, however, is not confirmed to be extraterrestrial. The most fragile IDPs are most likely to disintegrate at atmospheric entry and thus are lost for collection. If they would represent a type of Ca-rich IDPs, this would explain the average Ca depletion in more compact IDPs.

5.6 IDPs (substrate: Kapton)

The interplanetary dust particles presented in the following were prepared on Kapton substrates for the TOF-SIMS surface analysis. With this initially applied mount it was in most cases not possible to remove the silicone oil: Except for U2071H9, no analysis of the very surfaces was possible (Rost, 1995; Rost *et al.*, 1999).

5.6.1 U2071B6

SEM analysis. U2071B6 is a 20 µm sized chondritic IDP with a rough surface. The absolute content of 15 wt% Si ($1.4 \times$ CI) feign a depletion of most major elements in the column $[\mathsf{E}]_{\mathsf{Si,CI}}$ (Table 5.10). Actually, O, Mg, Al, Si, S, and Fe have chondritic abundances within a factor of 1.4. This compact IDP is enriched in Cl ($7 \times \mathrm{CI}_{\mathsf{Si}}$) and P ($3 \times \mathrm{CI}_{\mathsf{Si}}$).

Surface analysis. Silicone oil residues prevented a proper TOF-SIMS surface analysis of U2071B6. Secondary ion distribution images (Fig. 5.22) and the results from the TOF-SIMS surface analyses in Table 5.10 represent only measurements of the oil.

PIXE bulk analysis. The silicone oil contamination for U2071B6 precluded PIXE.

Section analysis. Figure 5.23 shows the results from the TOF-SIMS section analysis and a FEG-SEM image of the section. U2071B6 itself is

	SEM-EDS		TOF-SIMS (surf.)		TOF-SIMS (sect.)	
E	[wt%]	$[E]_{Si,CI}$	E/Si [at]	$[E]_{Si,CI}$	E/Si [at]	$[E]_{Si,CI}$
C	9	190	480	640	370	500
C			120	20000	250	340
O	36	56	26	3.4	310	41
O					100	13
Na	1.8	260			3.3	58
Mg	10.2	74			35	33
Al	1.1	87			4.2	50
Si	14.8	≡100	≡100	≡100	≡100	≡100
P	*0.4*	*200*			*0.8*	*80*
S	7.3	84				
Cl	*0.7*	*700*	0.0018	0.3	4.2	800
K					0.22	58
Ca	0.32	25			0.40	6.5
Ti					0.10	40
Cr	0.3	70			0.68	51
Mn	0.4	160			1.5	150
Fe	15	58			25	28
Co					0.08	30
Ni	2.0	130			2.8	57

Table 5.10: Element abundances in U2071B6. The TOF-SIMS surface analysis actually represents a measurement of impeding silicone oil residues.

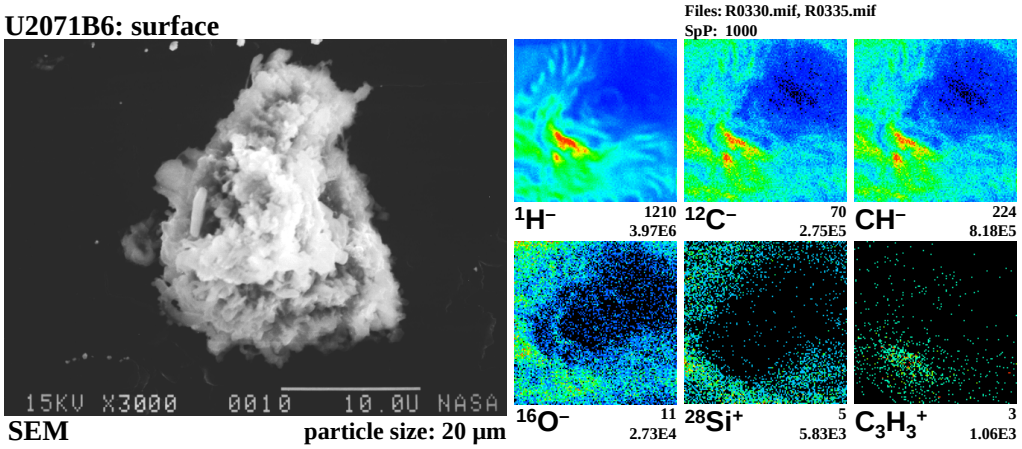

Figure 5.22: Field of view: $40 \times 40\,\mu m^2$; 128×128 pixels; no sputtering

outlined by a dotted line, because it can be hardly recognized in its wrapping of polymerized silicone oil. The color assignment in the Si^+ and Cl^- image had to be adjusted to emphasize the ion distribution inside the particle. The particle is dominated by Al, Mg, and Fe-rich silicates.

In contrast to the epoxy resin, the polymerized silicone oil is rather free of F and Cl, but rich in O, Na, Si, and K.

Several distinct grains exist within this matrix. There are about five submicrometer sized Ca and CaO-rich phases. The anti-correlation with Si point at calcite, $CaCO_3$. F, Cl, and Mn also occur within the Ca-rich phase. Mn is frequently found in carbonates, where it replaces the Ca, this may be indicative for this mineral. The highest intensity of F is correlated with the largest grain of the Ca-rich phase.

Two S-rich phases occur close to the center of the particle. One is about one micrometer in size and iron dominated. The other one is slightly larger, about $2\,\mu m \times 1\,\mu m$, and is rich in Mn (Rost *et al.*, 1998). They are both low in Si or, because of the limited lateral resolution, it is probably entirely absent. Probably the grains are sulfides.

The Mn-rich phase is shown in grater detail in Figure 5.24. The FEG-SEM detail image indicates a substructure within the grain, maybe a clue to an intergrowth of two different phases, possibly two distinct sulfides or a sulfide and a silicate phase. Unlike Si, Fe is not depleted and is therefore also occurring in the sulfide, with an estimated composition of $(Mn_{0.47}Fe_{0.53})S$. Mn-rich sulfides are called alabandite, with increasingly Fe content also ferroalabandite.

Alabandite with comparable high Fe abundance was found only once before in a meteorite: 49 wt% Fe in the EL7 enstatite chondrite LEW 87119 (Zhang *et al.*, 1993), but there it also contained MgS that is absent in the here discussed phase.

TEM analysis. Unfortunately, a thin section representing the very counterpart to the section analyzed with TOF-SIMS was not available; it was torn during microtome cutting. Therefore, the interesting Mn,Fe-sulfide could not be further characterized with TEM. Only one ~ 50 nm sized Fe-sulfide with minor Mn content was found. Some saponite fibres could be identified. Several Ni containing inclusions with sizes ≥ 50 nm were found roughly aligned.

Discussion. The most interesting feature of this IDP is the occurrence of a Mn-rich sulfide, probably alabandite, which was never observed before in any interplanetary dust particle. Its unusually high Fe content and the appearance in the FEG-SEM image can be interpreted as an intergrowth of two phases, possibly an Fe-rich mineral and a Mn dominated sulfide, with the latter being the mineral alabandite. However, the typical extraterrestrial homes of alabandite are enstatite chondrites and achondrites, which have a reducing

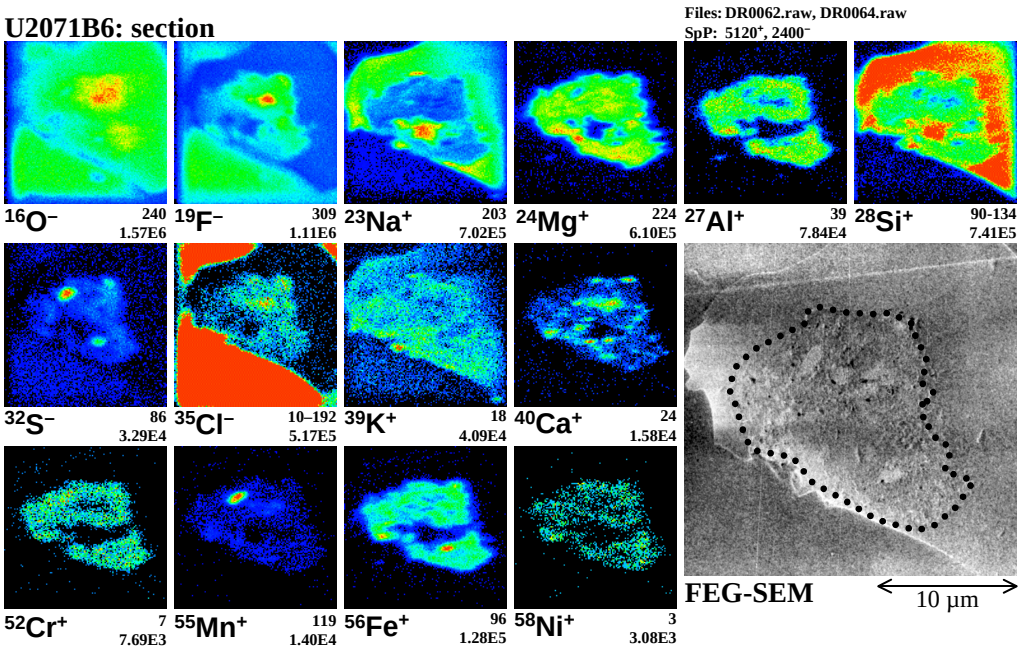

Figure 5.23: Field of view: $25 \times 25\,\mu m^2$; 128×128 pixels; no sputtering

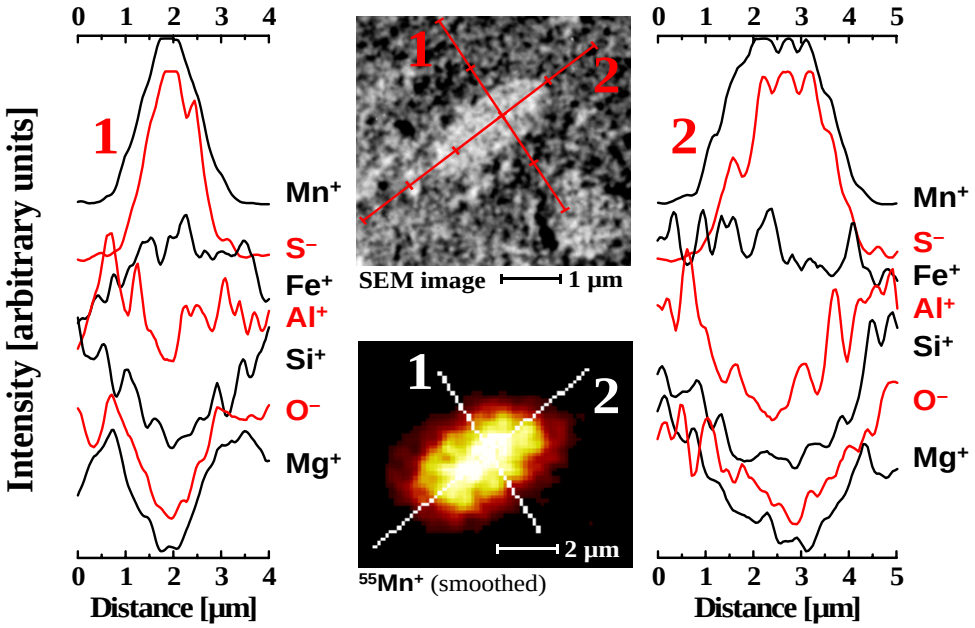

Figure 5.24: Detail images of the Mn-rich sulfide in U2071B6. The profile through the phase demonstrates which elements coincide (Mn, Fe, S) in the phase and which do not (O, Mg, Al, Si).

chemistry. U2071B6's chemical and mineralogical composition (saponite!) is comparable to carbonaceous chondrites, but not to the metal rich enstatite chondrites. Therefore, the occurrence of this mineral in U2071B6 remains to be explained.

5.6.2 U2071C3

SEM analysis. This compact and irregular shaped IDP has a size of 19 µm × 14 µm and chondritic abundances in all elements (Table 5.11) except the enriched Na ($2.4 \times CI_{Si}$) and the depleted S ($0.16 \times CI_{Si}$) and Ca ($0.5 \times CI_{Si}$).

	SEM-EDS		PIXE (bulk)		TOF-SIMS (surf.)		TOF-SIMS (sect.)	
E	[wt%]	$[E]_{Si,CI}$	[wt%]	$[E]_{Si,CI}$	E/Si [at]	$[E]_{Si,CI}$	E/Si [at]	$[E]_{Si,CI}$
Li							0.0065	110
B							0.008	400
C	2	50			3900	5100	120	150
C					45000	59000	57	76
O	39	68			70	9.2	790	100
O							350	46
Na	1.5	230					3.3	58
Mg	10.6	86	12	90			64	59
Al	1.2	110	1.0	80	1.0	12	7.2	85
Si	13.3	≡100	16	≡100	≡100	≡100	≡100	≡100
P	*0.4*	*300*	0.19	110				
S	1.0	13	2.2	25				
Cl	*0.03*	*30*	0.11	110	0.014	2.7	3.4	640
K			0.096	120			0.30	81
Ca	0.52	45	0.96	71			2.3	38
Sc							0.0046	130
Ti			0.058	91			0.15	62
V							0.011	36
Cr	*0.2*	*70*	0.35	90			0.77	57
Mn	*0.2*	*80*	0.32	110			0.88	92
Fe	28	120	23.4	84.4			33	36
Co							0.057	25
Ni	1.4	100	0.94	59			1.7	35

Table 5.11: Element abundances in U2071C3. The TOF-SIMS surface analysis actually represents a measurement of impeding silicone oil residues; the average of two small area measurements is given.

Surface analysis. Again, silicone oil residues made the analysis of the very IDP surface impossible. This contaminant is responsible for the measured secondary ions (Fig. 5.11) and the hence resulting abundances (Table 5.11).

Section analysis. The FEG-SEM image shows an irregular outer surface on a submicrometer scale. The particle material encloses several cavities.

The particle is dominated by silicates with varying abundances of Mg, Al, Ca, and Fe. Generally, this IDP seems to be a rather heterogeneous mixture of different mineral phases.

Fe and Ni are enriched close to the surface, whereas the silicates deeper inwards are characterized by high Mg and Al abundances. The occurrence of $FeOH^+$ is correlated with $CaOH^+$ (and Ca^+). In the top right region of the particle is a $2\,\mu m \times 0.5\,\mu m$ sized Ca-rich and Si-poor phase. Apart from O and some minor amounts of Mn, no other elements are present. It is probably a carbonate.

The alkali metal K is almost homogeneously distributed, whereas Na is more enriched in a $\sim 3\,\mu m$ sized area on the top side of the particle.

Several S-rich and Si-depleted mineral grains, probably sulfides, are found around the central cavities. Ni and especially Fe are also found in this phase, whereas metals like Mg, Al, Cr, Mn, and the alkali metals are missing. The occurrence of Fe_2S^+ corroborates the identification as sulfides. Their sizes range from $\sim 0.2\,\mu m$ to $\sim 1\,\mu m$.

The halogens F and Cl suggest a surface correlated enrichment, especially on the left and top side. F is regularly incorporated into silicates throughout the particle with an enrichment on the left side, partly correlated with O. The Cl signal from the epoxy is much superior to signal from U2071C3, except for a chain of several tiny and separated Cl enrichments on the verge of the particle.

PIXE bulk analysis. The SEM-EDS derived abundances are approximately confirmed by PIXE analysis, including the depletion of S (Table 5.11). The particle's orientation during this measurement is the same as in the TOF-SIMS surface analysis, because it was still on the Kapton substrate. Unlike the analysis of U071D1, here a comparison of the derived element distribution with the results of the TOF-SIMS section analysis is difficult, because the section plane of the latter does not correspond with the field of view of the PIXE measurements.

The probably best approach is given in Figure 5.27: the PIXE images are rotated in a way that the outer shape and the S and Ca distribution show maximum coincidence with the TOF-SIMS measurements. Especially the confined occurrence of S enables hardly another possibility. The PIXE

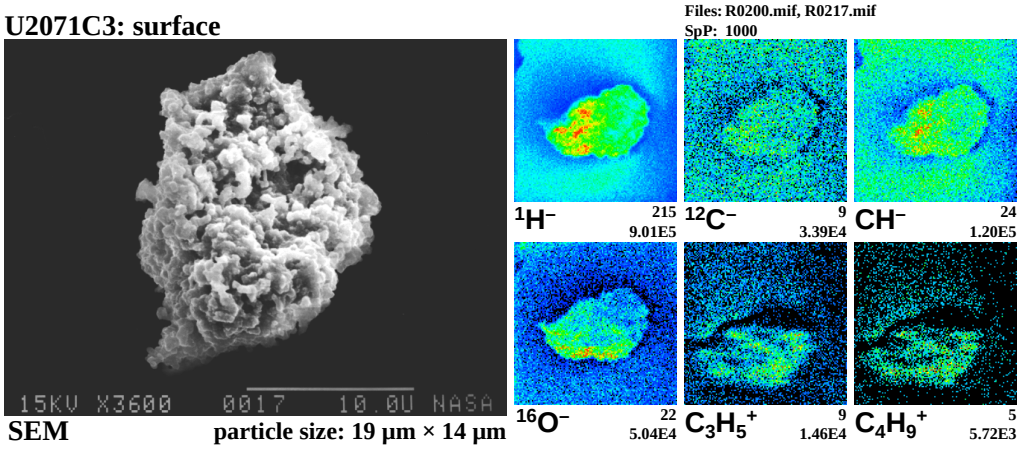

Figure 5.25: Field of view: $40 \times 40\,\mu m^2$; 128×128 pixels; no sputtering

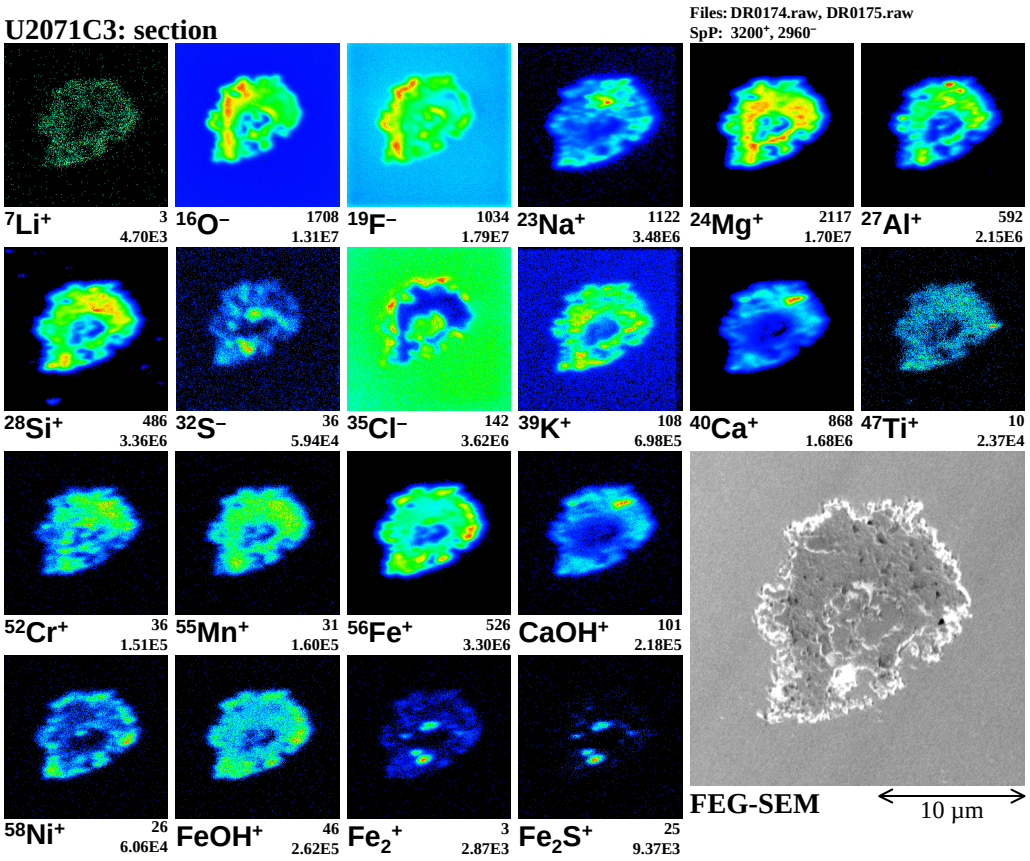

Figure 5.26: Field of view: $25 \times 25\,\mu m^2$; 256×256 pixels; with Ar sputtering

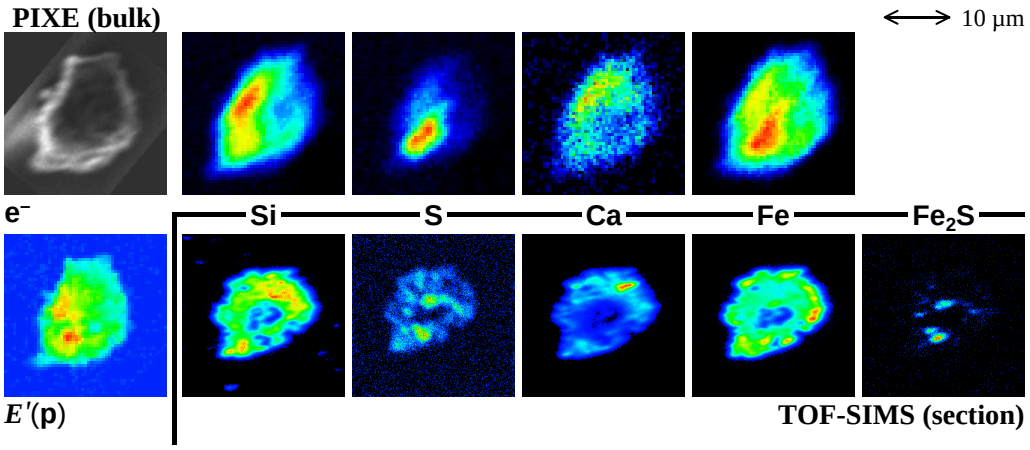

Figure 5.27: 2-dimensional distribution of the element concentrations in U2071C3 as derived from PIXE bulk analysis. For a better comparison the corresponding TOF-SIMS section results are given again.

data prove that S is enriched close to the center of U2071C3, obviously in the Fe-sulfides found with TOF-SIMS.

The distributions of Si and Fe, as derived by the two techniques, are rather dissimilar. While the PIXE bulk analysis found the majority of Fe in the center, correlated with S, it seems to be enriched in a rim close to the surface in the TOF-SIMS section analysis. One has to keep in mind that the Fe distribution only slightly deviates from the total mass distribution, here represented by the STIM measurement of $E'(\mathrm{p})$, indicating an almost homogeneous distribution inside the particle.

Discussion. The surface relation of Cl indicates a contamination. The F that is enriched in surface near silicates may also stem from a contamination — it could have migrated into this region. However, the majority of the remaining, homogeneously distributed F is probably indigenous.

The combination of the results from the different analytical techniques is not trivial for U2071C3. Particularly the comparison of the PIXE bulk measurement and the TOF-SIMS section analysis suffer from the different orientations of the particle during the respective analyses.

5.6.3 U2071H9

SEM analysis. This IDP has an irregular shape, a size of 17 µm × 12 µm, and a mostly smooth surface. It was classified as FSN particle, because it contains 38 wt% Fe, 9 wt% S, and 19 wt% Ni (Table 5.12). In the SEM-EDS analysis also some chondritic material was identified accounting for 1.7 wt% Si and 0.4 wt% Mg. A high C content (6 wt%) indicates a special carbonaceous phase.

	SEM-EDS		PIXE (bulk)		TOF-SIMS (surf.)		TOF-SIMS (sect.)	
E	[wt%]	$[E]_{Si,CI}$	E/Fe [wt]	$[E]_{Si,CI}$	E/Si [at]	$[E]_{Si,CI}$	E/Si [at]	$[E]_{Si,CI}$
Li					0.0009	17		
Be					0.006	8000		
B					0.06	3100	2.4	110000
C	6	1100			2200	2900	6500	8500
C					470	620	1900	2500
O	26	350			1700	220	620	81
O					780	100	4000	500
Na					7.8	140	310	5300
Mg	0.39	25			1.1	1.0	31	29
Al					0.10	1.2	6.1	72
Si	1.66	≡100	7.5	≡100	≡100	≡100	≡100	≡100
P					0.59	57		
P					*3*	*300*		
S	9.0	920	68.8	1560				
Cl	*0.4*	*3000*	1.7	3300	230	44000	69	13000
K			0.90	2300	19	5000	49	13000
Ca			0.24	37	0.86	14	15	240
Ti					0.007	3		
V					0.029	100		
Cr					0.026	1.9		
Mn			0.3	210	0.057	6.0	*10*	*1000*
Fe	38	1300	≡100	745	99	110	2300	2600
Co			5.4	15000	0.08	36	84	37000
Ni	19.2	11200	134	17300	13	270	6700	140000
Cu					0.21	410		

Table 5.12: Element abundances in U2071H9. The average of three small area measurements is given for the TOF-SIMS surface analysis. The Si abundance is possibly falsified by some silicone oil residues, which would result in an additional systematic error of the $[E]_{Si,CI}$ values.

After subtracting the silicate component and normalizing to Fe, the remaining atomic abundances amount to: C/Fe = 0.9, O/Fe = 2.4, S/Fe = 0.5, and Ni/Fe = 0.6. With (Fe,Ni)S being the usual sulfide phase of FSN particles, only one third of the metal is bound in this way. The remaining Fe and Ni can occur as pure metal, *e.g.*, taenite (γ-FeNi), or as oxides like magnetite, Fe_3O_4. Assuming that all non-sulfidic metal is oxidized, the remaining O is equally abundant as C. Together with H and N, which cannot be detected with SEM-EDS, these elements may form a 'CHON' phase of primitive material, as found in comet P/Halley (Jessberger *et al.*, 1988).

Surface analysis. Concerning the particles prepared on Kapton, U2071H9 is the only IDP, of which the very surface could be analyzed with TOF-SIMS (Fig. 5.28).

Fe and Ni are observed on the particle's surface, as expected from SEM-EDS analysis. The enhanced intensity in a spot on the lower left side is probably just a result of surface morphology.

S is also observed on the whole surface, but its intensity is very low, except for a spot that also coincides with high Na, Cl, and K signals. This may indicate the remains of an aerosol droplet. It cannot be an intact one, because free water would evaporate under the ultra-high vacuum conditions.

The halogens F, Cl, and Br are uniformly distributed over the particle's surface, apart form a Cl enrichment in one spot (see above).

The rather abundant Si cannot be expected to come from an Fe,Ni,S phase. It either points to the chondritic component observed with SEM-EDS or indicates some remaining silicone oil. The latter explanation is more plausible, because Mg and Al are not found in chondritic abundances on the surface, but only with $0.01 \times \mathrm{CI_{Si}}$ (cf. Table 5.12). Consequently, the observed H and C could also stem from oil residues. However, the detection of Fe and Ni on the very surface indicates that the thickness of this contamination can only be on the order of some monolayers.

PIXE bulk analysis. The distribution of Fe and Ni is rather homogeneous throughout U2071H9 (Fig. 5.29). S is also broadly abundant in the particle but more expressed in the upper region — even more than Ni. Their atomic abundances relative to Fe are S/Fe = 1.2 and Ni/Fe =,1.2, which does not correspond to the SEM-EDS results. But in both cases S and Ni are equally abundant. Therefore, a higher Fe content in the $\sim 2\,\mu$m thick surface volume analyzed by SEM-EDS must be responsible for the deviation.

Si, Cl, K, and Ca show similar distributions. They are mainly found in surface near particle material at the upper side, as seen in Figure 5.29.

Section analysis. This measurement was hampered by some epoxy smeared over the IDP during ultramicrotome cutting. It covered the sectioned IDP to approximately one third (cf. the FEG-SEM image in Fig.

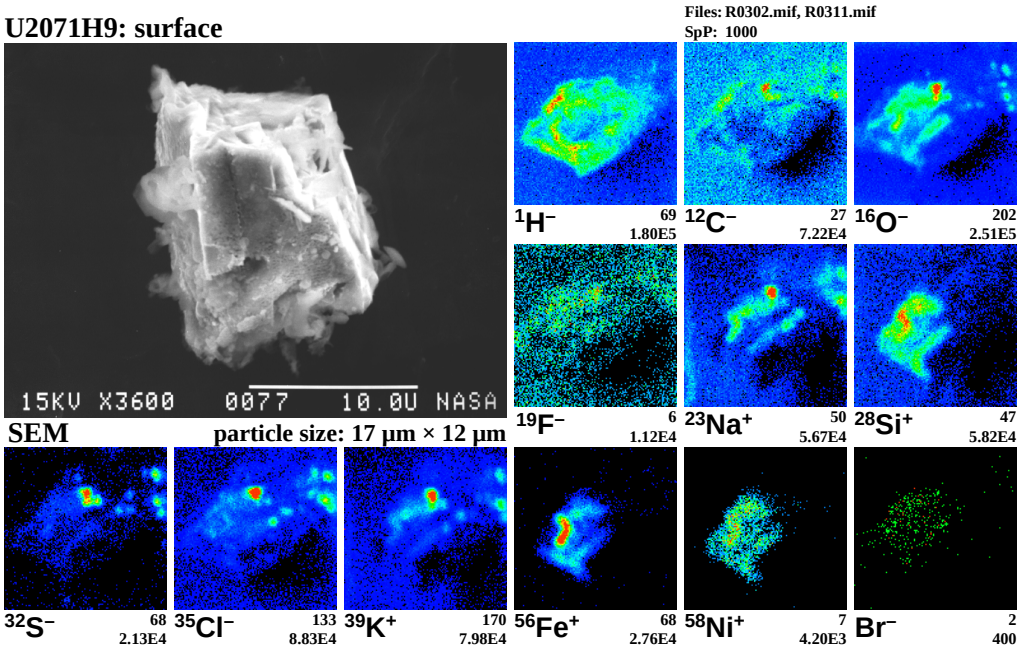

Figure 5.28: Field of view: $30 \times 30\,\mu m^2$; 128×128 pixels; no sputtering

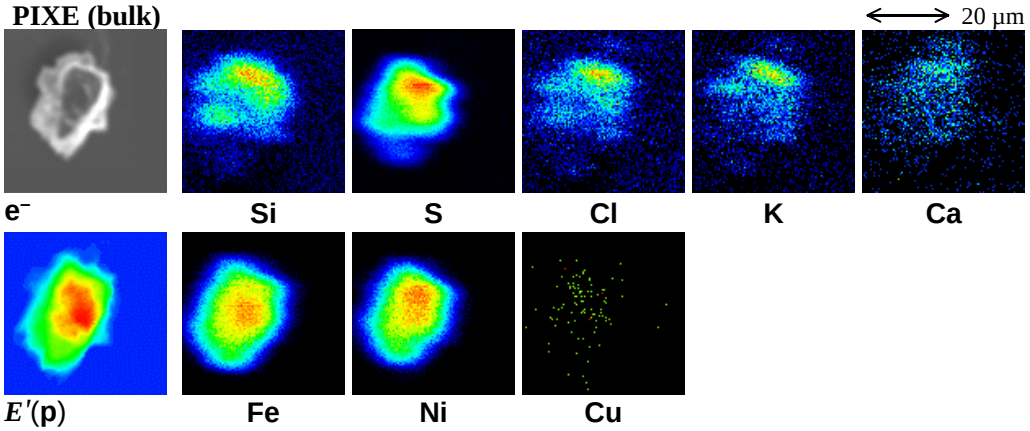

Figure 5.29: 2-dimensional distribution of the element concentrations in U2071H9 as derived from PIXE bulk analysis.

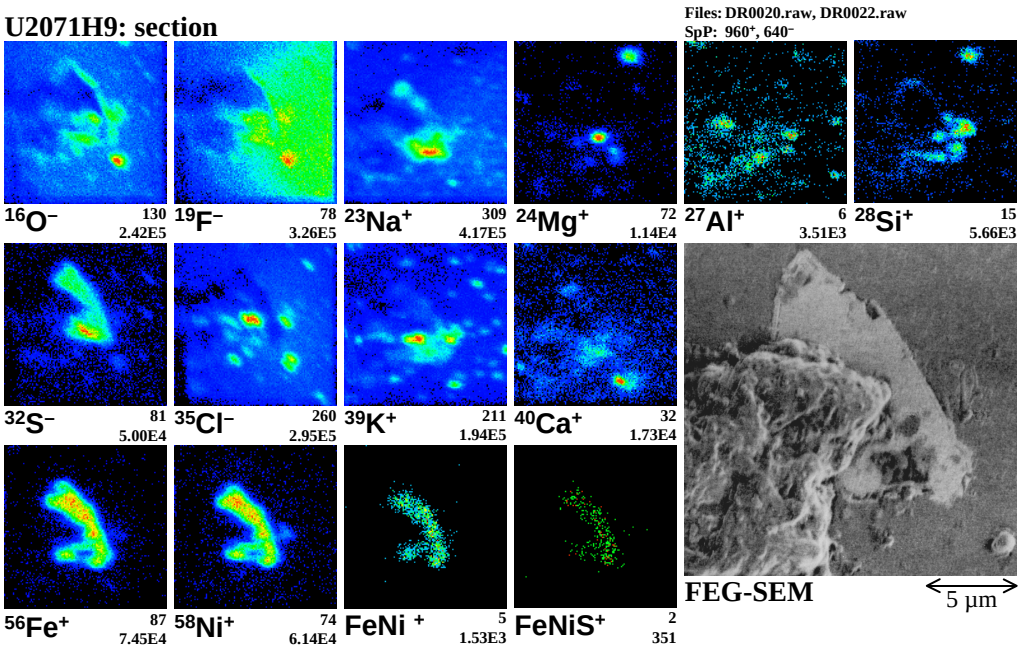

Figure 5.30: Field of view: $30 \times 30\,\mu m^2$; 128×128 pixels; no sputtering. The measurement of negative secondary ions has a field of view that is shifted downwards by $\sim 5\,\mu m$ relative to the analyzed area of the positive secondary ion measurement.

5.30). It accounts for the most intense Cl spot. Moreover, several smaller dirt particles and salt grains soil the sample surface, *e.g.*, the spot rich in Mg and Si in the upper right corner of the secondary ion images and several spots of Cl and K.

Most of the accessible particle area belongs to a phase rich in Fe, Ni, and S, as expected. It cannot be deduced from TOF-SIMS analysis, whether this phase is a stoichiometric sulfide or a mixing of sulfide and metal on a scale less than $\sim 0.3\,\mu m$, which is the lateral resolution. The lack of O in this area excludes metal oxides like magnetite, at least they are not present in the section plane.

Fe and Ni are highly correlated throughout the sulfide phase. Their TOF-SIMS derived atomic ratio amounts to Ni/Fe = 2.9, which is more than twice as much as the bulk ratio measured by PIXE. Their homogeneous distribution does not confirm enriched Fe toward the surface, as is expected for the material analyzed by SEM-EDS. The material analyzed by SEM-EDS is probably not located in the section plane. The slight deviation between the Ni and the Fe distribution found with PIXE are also not reflected in the

section. Probably a smaller phase rich in Ni accounts for the enrichment in the upper region of U2071H9 (cf. Fig. 5.29).

A narrow rim with a thickness of 0.3 µm can be observed in the FEG-SEM image around the particle. This rim is also outlined in the secondary ion distributions of O, Na, and Si — the same elements that coincided with the polymerized silicone oil around U2071B6 (cf. Fig. 5.23). However, the rim may also represent an indigenous, Na bearing silicate. According to its continuous appearance, especially in the FEG-SEM image, one would expect this phase to envelop the whole particle. This cannot be true, because it would have prevented the detection of the Fe,Ni,S-phase on the surface.

The halogens F and Cl that have been detected in this TOF-SIMS section analysis can all be a result of laboratory contamination like the epoxy resin that obstructs the section. Their overall occurrence is not related with U2071H9, except for two spots on the verge of the original particle surface.

Discussion. SEM-EDS, TOF-SIMS, and PIXE consistently found that U2071H9 is dominated by Fe, S, and Ni-rich material. But the relative ratios of these elements are different for the individual technique. This can, at least partly, be understood by considering the respective analyzed volume. In addition, TOF-SIMS sensitivities are not sufficiently known for sulfides.

PIXE analysis shows that the particle contains slightly more Ni than Fe. One section plane, not necessarily through the particle's center, intersects a large homogeneous sulfide, in which Ni is almost three times as abundant as Fe (TOF-SIMS). In a surface region on one side of the particle, some CHON material together with chondritic material occurs; here, on the average, Fe is twice as abundant as Ni (SEM-EDS).

On the very surface the halogens F, Cl, and Br are detected. They are absent in the sulfide phase inside the IDP. They are probably a result of stratospheric aerosols. An indigenous occurrence in the chondritic material or in the CHON phase cannot be excluded, but seems to be unlikely.

5.6.4 U2071B7a, F3, H1a: inhibited analysis

Surface analysis. Silicone oil residues on their surfaces prevented proper TOF-SIMS analyses (Figs. 5.31, 5.32, and 5.33, and Tables 5.13, 5.14, and 5.15). Therefore, the TOF-SIMS results are only given for completeness, together with the SEM images and the SEM-EDS derived abundances.

Section analysis. U2071B7a was lost during an attempt to rinse off the silicone oil with hexane. No remainders of U2071F3 are left in the stub after preparing thin sections for the TEM study – thus making a TOF-SIMS section analysis impossible. U2071H1a fell off the Kapton substrate before it could be carbon coated for the PIXE bulk analysis.

E	SEM-EDS [wt%]	SEM-EDS $[E]_{Si,CI}$	TOF-SIMS (surf.) E/Si [at]	TOF-SIMS (surf.) $[E]_{Si,CI}$
C	31	840	520	690
C			350	460
O	30	60	105	14
O			*100*	*20*
Na	1.1	200	1.3	23
Mg	6.7	63	0.30	0.28
Al	0.9	90	1.5	17
Si	11.5	≡100	≡100	≡100
P	*0.5*	*400*	*20*	*2000*
S	6.3	93		
Cl	*0.3*	*300*	2.7	510
K			0.011	3
Ca	0.48	48	0.15	2.4
Fe	10.8	52.7		
Ni	0.6	50		

Table 5.13: Element abundances in U2071B7a

E	SEM-EDS [wt%]	SEM-EDS $[E]_{Si,CI}$	TOF-SIMS (surf.) E/Si [at]	TOF-SIMS (surf.) $[E]_{Si,CI}$
C	6	130	2400	3100
C			6100	8100
O	38	60	32	4.1
Na	1.5	210		
Mg	9.1	68		
Al	1.4	120	2.6	30
Si	14.5	≡100	≡100	≡100
P	*0.4*	*200*		
S	2.5	29		
Cl	*0.3*	*300*	0.010	1.9
K			1.7	460
Ca	0.20	16		
Mn	*0.1*	*50*		
Fe	25	96		
Ni	1.1	71		

Table 5.14: Element abundances in U2071F3

E	SEM-EDS [wt%]	SEM-EDS $[E]_{Si,CI}$	TOF-SIMS (surf.) E/Si [at]	TOF-SIMS (surf.) $[E]_{Si,CI}$
C	6	190	24000	32000
C			7200	9500
O	29	69	46	6.1
Na	0.3	70	0.25	4.3
Mg	7.8	88		
Al	0.8	100	2.9	34
Si	9.6	≡100	≡100	≡100
P	*0.4*	*400*		
S	11.3	200		
Cl	*0.2*	*300*		
K				
Ca	0.61	73		
Cr	0.7	280		
Mn	*0.2*	*90*		
Fe	33	190		
Ni	1.3	130		

Table 5.15: Element abundances in U2071H1a

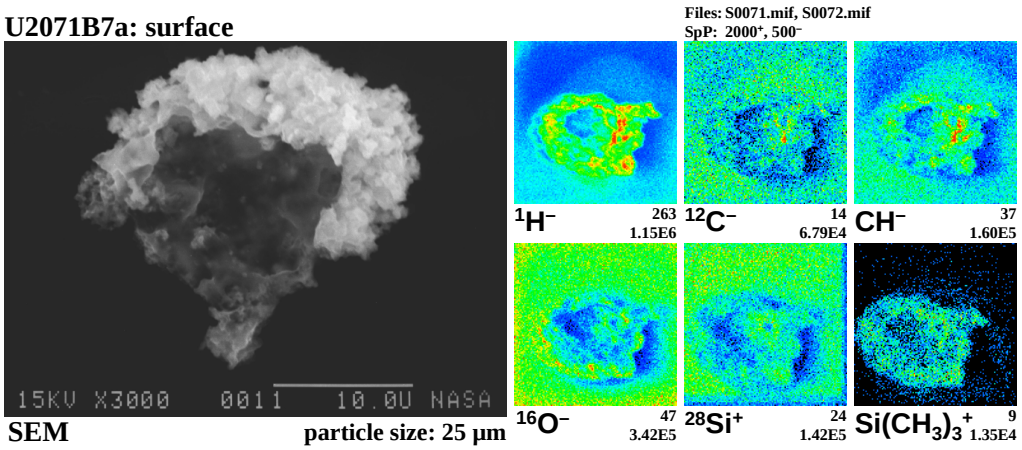

Figure 5.31: Field of view: $40 \times 40\,\mu m^2$; 128×128 pixels; no sputtering

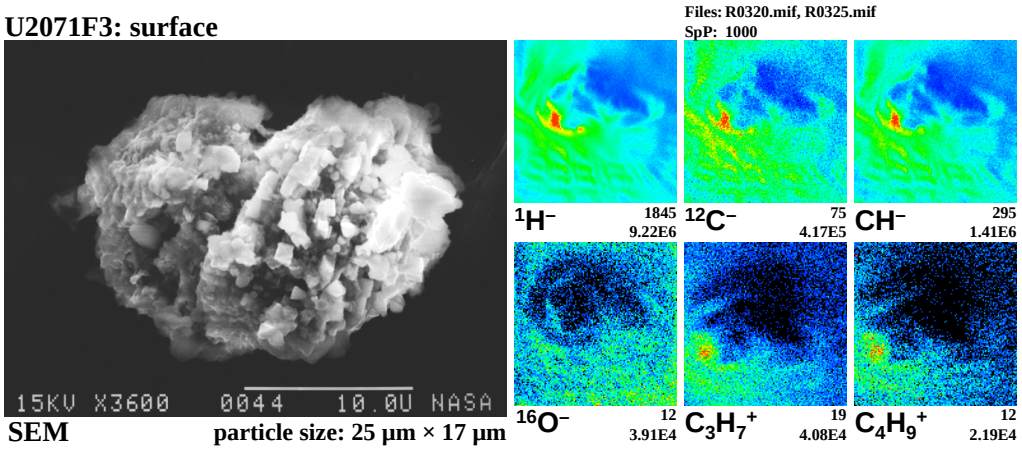

Figure 5.32: Field of view: $40 \times 40\,\mu m^2$; 128×128 pixels; no sputtering

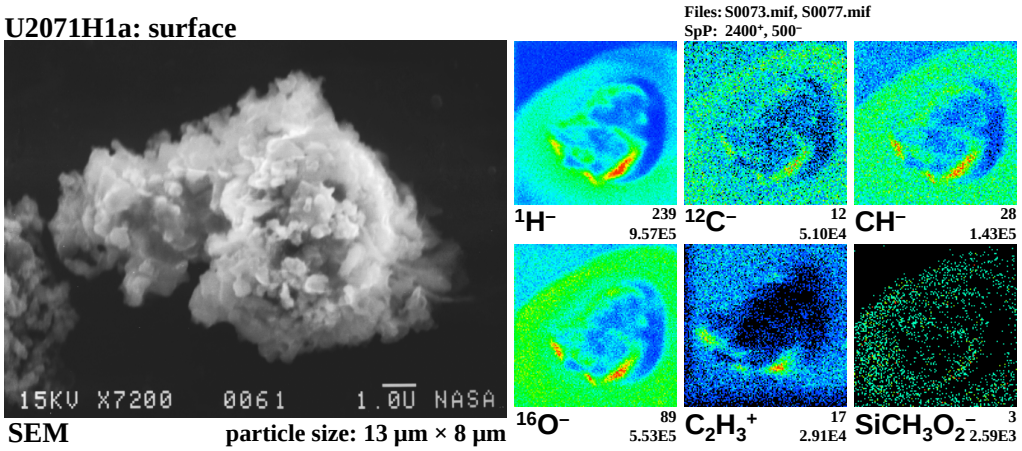

Figure 5.33: Field of view: $20 \times 20\,\mu m^2$; 128×128 pixels; no sputtering

Chapter 6

Summary

6.1 Particle surface analysis with TOF-SIMS

TOF-SIMS is usually applied to plane samples and easily allows the acquisition of secondary ion distribution images, *i.e.*, lateral element distributions. If rough surfaces are analyzed, however, the interpretation of the intensity variations is more complicated by angular effects on the secondary ion yields. Their influence was simulated in a model calculation. The model was successfully tested by analyzing spheres. It explains all peculiarities observed in the measurements: enhancement of the secondary ion signal on one side of the particle, a 'shadow' on the other side, and distortion effects as a consequence of the scanning technique. Furthermore, the nonuniform removal of surface material enables the identification of thin surface layers like contamination on the particle.

6.2 Contamination

The motivation to perform TOF-SIMS analysis of rough surfaces was to settle the question of stratospheric contaminants of IDPs. This, however, must also be discussed considering TOF-SIMS section and PIXE results.

Be. The TOF-SIMS study revealed surface correlated Be, usually small spots with high Be (up to some $10000 \times \mathrm{CI_{Si}}$). Since they often occur in exposed positions, it is highly probable that they stem from the Be substrate of the SEM-EDS analysis. In some cases, however, Be enrichments from $10 \times \mathrm{CI_{Si}}$ to $200 \times \mathrm{CI_{Si}}$ were found homogeneously distributed over the entire particle surface. Be was possibly spread over the surface during the hexane rinsing procedure.

Halogens. The TOF-SIMS results give several examples for halogens inside IDPs: One half of the sectioned IDP U2071B6 contains F, and high intensities of F and Cl are correlated with a Ca-rich phase. In U2071C3 F is broadly distributed within the IDP and enriched on one side in a rim of surface near material, partially correlated with O. The apatite detected in U2071L1 bears F and to a lesser extent also Cl. In addition to these chondritic IDPs, F, Cl, Br, and I were found in a presumably carbonaceous phase of U2071D1, whose extraterrestrial origin could not unequivocally be proven. Finally, the TCA particle U2071I9 shows homogeneously distributed F and some Cl coming from a small internal phase.

This study also revealed many instances of surface related halogens — far more than would emerge by chance, if inferring from their inner distribution. On four AOS particles a thin surface layer was identified, containing the halogens F, Cl, and Br. In the section analysis of U2071D4, E8, and L1 a F and Cl bearing rim around the particle was observed, probably related to the very surface of these IDPs. In case of U2071E8, on one side of the rim also Br was found. On the verge of the sectioned U2071C3 several separated Cl enrichments emerged. F and Br were found homogeneously distributed over the observable surface of the FSN IDP U2071H9. A spot rich in Cl was additionally detected. F, Cl, and Br appeared on the surface of U2071D1. The halogens (F, Cl, Br, I), that were found during the section analysis of this particle, are not necessarily pristine. They might have migrated into in their carbonaceous host phase from the adjacent surface. On one side of the TCN particle U2071E6 F, Cl, and Br were found partly correlated and close to the surface.

All these findings imply that a significant portion of the halogens is not indigenous, but acquired during the stratospheric residence of the particles. The remaining question is to what extent the observed mean Br enrichment in chondritic IDPs may be a result of stratospheric contamination. At first, a contamination process would affect only the surface near material of the particle. But IDPs frequently have a high porosity and contaminants may migrate into inner mineral phases. However, here it is impossible to discriminate the terrestrial from the indigenous portion.

On the other side, an indigenous mean enrichment of Br relative to CI abundances may be postulated. But no reasonable explanation is found up to now, how volatiles can be enriched in the IDP parent bodies with respect to the overall composition of the primitive solar dust cloud that is supposed to have CI chondritic abundances of all condensable elements, including Br.

Therefore, the broad occurrence of surface near halogen enrichments, as found in this study, rather implies, that the mean excess of Br must be attributed to stratospheric contamination. The detection of F and Br on the

surfaces of AOS particles and the flight experiment of Arndt *et al.* (1996a) indicate that such processes indeed occur.

6.3 Common properties of the studied IDPs

Only the FSN IDP U2071H9 could be analyzed with all methods as scheduled. Their findings require a varying Fe/Ni ratio throughout the particle. Not all of the metal can occur in sulfides, because the S content is consistently observed to be too low. The hence expected metal oxide was not observed in TOF-SIMS section analysis.

The other IDPs, all chondritic, lack at least the accomplishment of one method: TOF-SIMS surface analysis for U2071B6, C3 and F3, PIXE bulk measurement for U2071D4, E8, J9a, and L1, and TOF-SIMS section analysis for U2071F3 and J9a. Therefore, their overall picture is less complete than anticipated.

U2071J9a, *i.e.*, the entire 'J9' before it broke apart, is the only particle with strong evidence of being an anhydrous chondritic porous (CP) IDP. The other chondritic particles are compact and in most of them phyllosilicates are identified, *i.e.*, they are most probably hydrated chondritic smooth (CS) IDPs.

Ca. All cosmic IDPs in this study are depleted in Ca except U2071J9a. The precursor particle of U2071J9a had an estimated Ca content of $2 \times$ CI, which is within the usual range of CP particles, although their average concentration is slightly below CI (Schramm *et al.*, 1989; Arndt *et al.*, 1996b).

U2071D1 is exceptionally rich in Ca. The particle could not be classified at first, but its mineralogical characteristics indicate a possible extraterrestrial origin. U2071D1 may represent a non-chondritic IDP class, which carries the Ca that is missing on the average in the known IDP types, especially in CS particles (Schramm *et al.*, 1989; Arndt *et al.*, 1996b). Extraterrestrial particles with the size of U2071D1 ($\sim 40\,\mu m$) are only rarely collected in stratosphere, because they have a low probability to survive atmospheric entry heating (Love and Brownlee, 1994), and if they do, their faster settling velocities additionally decrease their abundance in the stratosphere.

S is depleted below $0.5 \times$ CI in the IDPs U2071C3, F3, and L1. It is possible that these particles had a chondritic abundance of S prior to their atmospheric entry. But at temperatures around 800°C, which should be often experienced during deceleration (Love and Brownlee, 1991, 1994), IDPs may sustain a significant loss of the volatile S (Fraundorf *et al.*, 1982). Nevertheless, it cannot entirely be excluded, that some or even all of the observed

depletions were pristine properties of the IDPs, reflecting a heterogeneous distribution of S in the parent bodies.

Conspicuous minerals. Several interesting phases were observed in the TOF-SIMS analysis. Their unambiguous identification is not possible, because absolute element concentrations cannot be given with sufficient accuracy. From the broader scope of the Collector Project, this purpose is assigned to TEM analyses. Then the conspicuous phases found in the TOF-SIMS analysis should be characterized on a submicrometer scale resulting in their proper identification.

But unfortunately, the very thin section, that is opposed to the remainder of the particle left behind in the epoxy stub for TOF-SIMS section analysis, is often not available for a TEM study. In addition, not all available thin sections are analyzed so far due to shortage of manpower. Therefore, only a few TEM results exist.

Thus limited to the assumptions arising from TOF-SIMS, following conspicuous, unusual, or rare phases were found in the interplanetary dust particles of this study:

- Several Ca-rich phases $\lesssim 1\,\mu m$, presumably carbonate, inside U2071B6, C3, D1
- Some Fe sulfide grains $\lesssim 1\,\mu m$: one inside U2071B6 and three inside C3
- One $\sim 1\,\mu m$ sized, Mn dominated sulfide (alabandite) inside U2071B6; the estimated composition is $(Mn_{0.47}Fe_{0.53})S$
- One $10\,\mu m \times 2\,\mu m$ sized Fe,Ni-sulfide phase, presumably pentlandite, inside U2071E8
- Several grains of phosphate (apatite) $\lesssim 1\,\mu m$: one on the surface of U2071L1, the others inside the same particle
- The main phase of U2071H9 contains only Fe, Ni, and S, with an average atomic ratio of $Ni/Fe = 1.2$ (PIXE measurement).
- One C and halogen rich phase inside U2071D1, a particle not yet proven to be extraterrestrial

6.4 Synthesis of results from different analytical techniques

The combination of the independently obtained results is advantageous for two reasons: One technique can support the results of another, at least to

a certain degree — and/or the results complement each other yielding more information on the particle than a single measurement. U2071D1 serves as an example for this. Its bimodal structure with a Ca-rich phase in each center, surrounded by several other phases, is consistently found. For the FSN IDP U2071H9 the results were partly different, but not mutually exclusive. They could be combined in way that a more complete overall picture of the particle arose.

However, sometimes the results are not compatible with one another or at least difficult to interpret. The main reason is the lack of knowledge, how the respectively analyzed volumes are arranged in the whole particle. In case of U2071C3, the unknown orientation of the section plane relative to the particle complicated a proper synthesis of results.

6.5 Outlook

PIXE analyses of the sectioned stratospheric dust particles are just running. For this purpose 2–5 µm thick slices from the stubs containing the particle remainders had to be cut off. This and the following preparation (transfer onto Kapton foil and carbon coating) succeeded for U2071B6, C3, E8, H9, L1.

Some of the conspicuous phases discovered with TOF-SIMS will be further characterized and identified in a future TEM study of the already existing thin sections. Results from the PIXE section analysis will also be helpful for this purpose.

6.6 Final remarks

This thesis gives a midway report of the Collector project. Many difficulties were encountered, not all of which were anticipated: the silicone oil problem, the required developments of sample preparation and cutting, sample loss, the different 'time scale' of studies in different laboratories with different methods, the general impossibility to repeat measurements other than TOF-SIMS. Anticipated, but not yet fully solved problems include the different 'volumes of information' of SEM-EDS, PIXE, TOF-SIMS, and TEM and the TOF-SIMS yield problem.

The study, however, made it clear that one single analytical method applied to individual stratospheric dust particles inevitably will reveal a certain and limited portion of the information content in that particle. Complementary analyses are required to 'tell the story' of an IDP. To contribute to

learning how to do that was a major goal of this thesis. It is hoped that future studies will build on those experiences.

Acknowledgements

This work started at the *Max Planck Institut für Kernphysik* in Heidelberg and was continued at the *Institut für Planetologie*, Münster.

I am greatly indebted to Prof. Elmar K. Jessberger, who aroused my interest in analyzing 'extraterrestrial dust' and enabled this thesis. Numerous fruitful discussions guided me through the work — the experimental and the writing.

No lesser thanks go to Thomas Stephan, for providing help in all circumstances, beginning with the secrets of TOF-SIMS and not even ending with the mysteries of tax return. But becoming a friend to him was the biggest support.

I gratefully acknowledge contributions to the Collector Project from Kathy Thomas-Kepra and Jack Warren (SEM analysis at *JSC*), Wolfgang Klöck amd Keiko Nakamura (TEM analysis at the *Martin-Luther-Universität Halle-Wittenberg*), and the members of the PIXE working group in Heidelberg, Peter Arndt, Mischa Maetz, and especially Christian 'L.' Wies.

I thank all current and former members of the TOF-SIMS working group, especially my roommates Michael Commer, Torsten Henkel, Christian Heiß, Andreas Morlok, and Stefan Schirmeyer, for their tremendous team spirit going far beyond the concrete of the institute.

The technical assistance of the always helpful Frank Bartschat, Renate Budell, Margrit Flucks, Thorsten Grund, Ulla Heitmann, and Dietmar Pitzler is appreciated, and, not to forget, Gea McCormac, the heart of the institute.

Several colleagues supported me and if only by keeping company, Addi Bischoff, Ansgar Greshake, Andreas Kaus, Bianca and Dirk Kettrup, Jochen Kissel, Tim Röstermundt, Birgit Sepp, Iris and Dietmar Weber, and especially my former NON-TOF-SIMS roommates Annette Jäckel and Nadia Vogel.

P. Hudek, I. W. Rangelow gratefully provided the Si etched silicon wafer.

The work was supported by the *Deutsche Forschungsgemeinschaft* (grants Je96/6 and Je96/10) and a special grant from the *Minsterium für Schule und Weiterbildung, Wissenschaft und Forschung des Landes Nordrhein-Westfalen.*

This research has made use of NASA's Astrophysics Data System Abstract Service.

The last but not least thanks go to my amie $\mathcal{GUNDA}$ Lippoldt, for all her support and patience over the last years, as well as to my parents, my brother, and all my friends.

Bibliography

Anders E. and Grevesse N. (1989) Abundances of the elements: Meteoritic and solar. *Geochim. Cosmochim. Acta* **53,** 197–214.

Andersen C. A. (1969) Progress in analytic methods for the ion microprobe mass analyzer. *Int. J. Mass Spectrom. Ion Phys.* **2,** 61–74.

Antz C., Bavdaz M., Jessberger E. K., Knöchel A. and Wallenwein R. (1987) Chemical analysis of interplanetary dust particles with synchrotron radiation. *Proc. Europ. Regional Astronomy Meeting of the IAU* **10th,** 249–252.

Arndt P. (1997) Spurenelementgehalte und Dichten Interplanetarer Staubteilchen gemessen mit der Heidelberger Protonenmikrosonde. Dissertation, Universität Heidelberg. 97 pp.

Arndt P., Jessberger E. K., Warren J. and Zolensky M. (1996a) Bromine contamination of IDPs during collection (abstract). *Meteorit. Planet. Sci.* **31,** A8.

Arndt P., Bohsung J., Maetz M. and Jessberger E. K. (1996b) The elemental abundances in interplanetary dust particles. *Meteorit. Planet. Sci.* **31,** 817–833.

Arndt P., Jessberger E. K., Maetz M., Reimold D. and Traxel K. (1997) On the accuracy of element concentrations and masses of micron sized samples determined with the Heidelberg proton microprobe. *Nucl. Instr. and Meth. B* **130,** 192–198.

Benninghoven A. and Mueller A. (1972) Secondary ion yields near 1 for some chemical compounds. *Phys. Lett.* **40A,** 169–170.

Benninghoven A., Rüdenauer F. G. and Werner H. W. (1987) *Secondary Ion Mass Spectrometry.* John Wiley & Sons, New York. 1227 pp.

Beske H. E. (1967) Untersuchungen zur Emission positiver Sekundärionen aus festen Targets. Die Brauchbarkeit der Ionenbeschuß-Ionenquelle in der Massenspektroskopie. *Z. Naturforschg.* **22a,** 459–467.

Bohsung J., Arndt P., Jessberger E. K., Maetz M., Traxel K. and Wallianos A. (1995) High resolution PIXE analyses of interplanetary dust particles with the new Heidelberg proton microprobe. *Planet. Space Sci.* **43,** 411–428.

Bradley J. P. (1994a) Mechanisms of grain formation, post-accretional alteration, and likely parent body environments of interplanetary dust particles

(IDPs). *Analysis of Interplanetary Dust*, *Proc. AIP Conference 310* , 89–104 New York, USA. American Institute of Physics.

Bradley J. P. (1994b) Nanometer-scale mineralogy and petrography of fine-grained aggregates in anhydrous interplanetary dust particles. *Geochim. Cosmochim. Acta* **58,** 2123–2134.

Bradley J. P., Brownlee D. E. and Fraundorf P. (1984) Discovery of nuclear tracks in interplanetary dust. *Science* **226,** 1432–1434.

Bradley J. P., Sandford S. A. and Walker R. M. (1988) Interplanetary dust particles. In *Meteorites and the Early Solar System* (eds. J. F. Kerridge and M. S. Matthews), pp. 861–895. Univ. Arizona Press, Tucson.

Brownlee D. E. (1994) The origin and role of dust in the early solar system. *Analysis of Interplanetary Dust* (eds. M. E. Zolensky *et al.*), *Proc. AIP Conference 310* , 5–8 New York, USA. American Institute of Physics.

Brownlee D. E. and Wheelock M. M. (1985) Microprobe analysis of sectioned mafic and sulfide micrometeorites (abstract). *Meteoritics* **20,** 617.

Brownlee D. E., Tomandl D. A. and Hodge P. W. (1976a) Extraterrestrial particles in the stratosphere. *Interplanetary Dust and Zodiacal Light, Proc. of the IAU-Colloquium No. 31*, 279–283.

Brownlee D. E., Ferry G. V. and Tomandl D. (1976b) Stratospheric aluminum oxide. *Science* **191,** 1270–1271.

Brownlee D. E., Tomandl D. A. and Olszewski E. (1977) Interplanetary dust; A new source of extraterrestrial material for laboratory studies. *Proc. Lunar Sci. Conf.* **8th,** 149–160.

Brownlee D. E., Joswiak D. J., Love S. G., Nier A. O. and Schlutter D. J. (1993) Identification of cometary and asteroidal particles in stratospheric IDP collections (abstract). *Lunar Planet. Sci.* **24,** 205–206.

Brownlee D. E., Joswiak D. J., Love S. G., Bradley J. P., Nier A. O. and Schlutter D. J. (1994) Identification and analysis of cometary IDPs (abstract). *Lunar Planet. Sci.* **25,** 185–186.

Cassini J. D. (1730) Découverte de la lumière celeste qui paroist dans le zodiaque. *Mem. Acad. Roy. Sci., Paris* **8,** 119–209.

Cofer W. R., III, Pellett G. L., Sebacher D. I. and Wakelyn N. T. (1984) Surface chloride salt formation on space shuttle exhaust alumina. *J. Geophys. Res.* **89** (D11), 2535–2540.

Dohnanyi J. S. (1970) On the origin and distribution of meteoroids. *J. Geophys. Res.* **75,** 3468–3493.

Dohnanyi J. S. (1978) Particle dynamics. In *Cosmic Dust* (ed. J. A. M. McDonnell), pp. 861–895. John Wiley & Sons, Chichester.

Esat T. M., Brownlee D. E., Papanastassiou D. A. and Wasserburg G. J. (1979) Magnesium isotopic composition of interplanetary dust particles. *Science* **206,** 190–197.

Firsov O. B. (1970) Dependence of sputtering of a target on the angle of incidence of the bombarding particles. *Soviet Physics – Doklady* **14,** 1092–1094.

Flynn G. J. (1990) The near-Earth enhancement of asteroidal over cometary dust. *Proc. Lunar Planet. Sci. Conf.* **20th,** 363–371.

Flynn G. J. (1994) Interplanetary dust particles collected from the stratosphere: physical, chemical, and mineralogical properties and implications for their sources. *Planet. Space Sci.* **42,** 1151–1161.

Flynn G. J. and Sutton S. R. (1990) Synchrotron X-ray fluorescence analyses of stratospheric cosmic dust: New results for chondritic and low-nickel particles. *Proc. Lunar Planet. Sci. Conf.* **20th,** 335–342.

Flynn G. J. and Sutton S. R. (1991) Chemical characterization of seven large area collector particles by SXRF. *Proc. Lunar Planet. Sci. Conf.* **21st,** 549–556.

Flynn G. J. and Sutton S. R. (1992) Element abundances in stratospheric cosmic dust: Indications for a new chemical type of chondritic material (abstract). *Lunar Planet. Sci.* **23,** 373–374.

Flynn G. J., Bajt S. and Sutton S. R. (1996) Evidence for weakly bound bromine in large interplanetary dust particles collected from the stratosphere (abstract). *Lunar Planet. Sci.* **27,** 367–368.

Formann E., Viehböck F. P. and Wotke H. (1968) The angular distribution of scattered and sputtered 40-keV particles on poycrystalline target. *Can. J. Phys.* **46,** 753–758.

Fraundorf P., Brownlee D. E. and Walker R. W. (1982) Laboratory studies of interplanetary dust. In *Comets* (ed. L. L. Wilkening), pp. 383–409. The University of Arizona Press, Tucson, Arizona.

Ganapathy R. and Brownlee D. E. (1979) Interplanetary dust: Trace element analysis of individual particles by neutron activation. *Science* **206,** 1075–1077.

Hagenhoff B., van Leyen D., Niehuis E. and Benninghoven A. (1989) Time-of-flight secondary ion mass spectrometry of insulators with pulsed charge compensation by low-energy electrons. *J. Vac. Sci. Technol. A* **7,** 3056–3064.

Hamilton D. P., Grün E., Baguhl M. and Riemann R. (1995) Electromagnetic influences on solar system dust. *Physics, Chemistry, and Dynamics of Interplanetary Dust, IAU Colloquium No. 150*, 24.

Hennequin J.-F. (1968) Distributions énergétique et angulaire de l'émission ionique secondaire III. Distribution angulaire et rendements ioniques. *J. Phys.* **29,** 957–968.

Hinthorne J. R. and Anderson C. A. (1975) Microanalysis for fluorine and hydrogen in silicates with the ion microprobe mass analyzer. *Am. Mineral.* **60,** 143–147.

Homma Y. (1994) Sims quantitative analysis using relative sensitivity factors. *Secondary Ion Mass Spectrometry, Proc. SIMS IX* (eds. A.Benninghoven *et al.*), 135–139. Wiley, Chichester.

Hudson B., Flynn G. J., Fraundorf P., Hohenberg C. M. and Shirk J. (1981) Noble gases in stratospheric dust particles: Confirmation of extraterrestrial origin. *Science* **211,** 383–386.

Jessberger E. K. and Wallenwein R. (1986) PIXE characterization of stratospheric micrometeorites. *Adv. Space Res.* **6,** 5–8.

Jessberger E. K., Christoforidis A. and Kissel J. (1988) Aspects of the major element composition of Halley's dust. *Nature* **332,** 691–695.

Jessberger E. K., Bohsung J., Chakaveh S. and Traxel K. (1992) The volatile element enrichment of chondritic interplanetary dust particles. *Earth Planet. Sci. Lett.* **112,** 91–99.

Klačka J. (1992) Poynting-Robertson effect: I. Equation of motion. *Earth, Moon, and Planets* **59,** 41–59.

Klačka J. (1993a) Interplanetary dust particles: Disintegration and orbital motion. *Earth, Moon, and Planets* **60,** 17–21.

Klačka J. (1993b) Poynting-Robertson effect and orbital motion. *Earth, Moon, and Planets* **61,** 57–62.

Klöck W. (1999) Korrelierte mineralogische und chemische Untersuchungen an interplanetaren Staubteilchen und Mikrometeoriten. Habilitationsschrift, Martin-Luther-Universität Halle-Wittenberg. 163 pp.

Klöck W., Thomas K. L., McKay D. S. and Palme H. (1989) Unusual olivine and pyroxene composition in interplanetary dust and unequilibrated ordinary chondrites. *Nature* **339,** 126–128.

Kortenkamp S. J. and Dermott S. F. (1995) The origin of interplanetary dust particles. *Physics, Chemistry, and Dynamics of Interplanetary Dust, IAU Colloquium No. 150*, 24.

Leinert C. and Grün E. (1990) Interplanetary dust. In *Physics of the Inner Heliosphere I: Large-Scale Phenomena* (eds. R. Schwenn and E. Marsch), pp. 207–275. Springer, Berlin.

Love S. G. and Brownlee D. E. (1991) Heating and thermal transformation of micrometeoroides entering the Earth's atmosphere. *Icarus* **89,** 26–43.

Love S. G. and Brownlee D. E. (1993) A direct measurement of the terrestrial mass accretion rate of cosmic dust. *Science* **262,** 550–553.

Love S. G. and Brownlee D. E. (1994) Peak atmospheric entry temperatures of micrometeorites. *Meteoritics* **29,** 69–70.

Mackinnon I. D. R., McKay D. S., Nace G. A. and Isaacs A. M. (1982) Classification of the Johnson Space Center stratospheric dust collection. *Proc. Lunar Planet. Sci. Conf.* **13th,** *J. Geophys. Res.* **87,** A413–A421.

Mackinnon I. D. R., Gooding J. L., McKay D. S. and Clanton U. S. (1984) The El Chinón stratospheric cloud: Solid particulates and settling rates. *J. Volcanol. Geotherm. Res.* **23,** 125–146.

Maetz M. (1994) Scanning Transmission Ion Microscopy zur Bestimmung von Dichteprofilen von interplanetaren Staubteilchen. Diplomarbeit, Universität Heidelberg. 91 pp.

Maetz M., Arndt P., Greshake A., Jessberger E. K., Klöck W. and Traxel K. (1996) Structural and chemical modifications of microsamples induced during PIXE analysis. *Nucl. Instr. and Meth. B* **109/110,** 192–196.

Mamyrin B. A., Karataev V. I., Shmikk D. V. and Zagulin V. A. (1973) The mass-reflectron, a new nonmagnetic time-of-flight mass spectrometer with high resolution. *Sov. Phys.-JETP* **37** (1), 45–48.

Maurette M., Immel G., Hammer C., Harvey R., Kurat G. and Taylor S. (1994) Collection and curation of IDPs from the Greenland and Antarctic ice sheets. *Analysis of Interplanetary Dust* (eds. M. E. Zolensky *et al.*), *Proc. AIP Conference 310* , 277–289 New York, USA. American Institute of Physics.

McHugh J. A. (1975) Secondary ion mass spectrometry. In *Methods of Surface Analysis* (ed. A. W. Czanderna), pp. 223–278. Elsevier, Amsterdam.

McHugh J. A. and Stevens J. F. (1972) Elemental analysis of single mircrometer-size airborne particulates by ion microprobe mass spectrometry. *Anal. Chem.* **44,** 2187–2192.

McKeegan K., Zinner E. and Zolensky M. (1986) Ion probe measurements of O isotopes in refractory stratospheric dust particles: Proof of extraterrestrial origin (abstract). *Meteoritics* **21,** 449–450.

Morrison D. A. and Zinner E. (1976) The size frequency distribution and rate of production of microcraters. *Interplanetary Dust and Zodiacal Light, Proc. of the IAU-Colloquium No. 31*, 227–231.

Niehuis E., Heller T., Bendel C. and Zehnpfenning A. (1998) Recent developments forthe cameca tof-sims iv. *Secondary Ion Mass Spectrometry, Proc. SIMS XI* (eds. G. Gillen *et al.*), 779–782. Wiley, Chichester.

Oechsner H. (1970a) Energieverteilungen bei der Festkörperzerstäubung durch Ionenbeschuß. *Z. Physik* **238,** 433–451.

Oechsner H. (1970b) Energy distribution in sputtering processes. *Phys. Rev. Lett.* **24,** 583–584.

Oechsner H. (1973) Untersuchungen zur Festkörperzerstäubung bei schiefwinkligem Ionenbeschuß polykristalliner Metalloberflächen im Energiebereich um 1 keV. *Z. Physik* **261,** 37–58.

Öpik E. J. (1951) Collision probabilities with the planets and the distribution of interplanetary matter. *Proc. Roy. Irish Acad.* **54,** 165–199.

Prather M. J., García M. M., Douglass A. R., Jackman C. H., Ko M. K. W. and Sze N. D. (1990) The space shuttle's impact on the stratosphere. *J. Geophys. Res.* **95** (D11), 18583–18590.

Rajan R. S., Brownlee D. E., Tomandl D., Hodge P. W., Farrar IV H. and Britten R. A. (1977) Detection of ^{4}He in stratospheric particles gives evidence of extraterrestrial origin. *Nature* **267,** 133–134.

Rietmeijer F. J. M. (1987) Silicone oil: A persistent contaminant in chemical and spectral microanalyses of interplanetary dust particles (abstract). *Lunar Planet. Sci.* **18,** 836–837.

Rietmeijer F. J. M. (1989) Tin in a chondritic interplanetary dust particle. *Meteoritics* **24,** 43–47.

Rietmeijer F. J. M. (1993) The bromine content of micrometeorites: Arguments for stratospheric contamination. *J. Geophys. Res.* **98,** E7409–E7414.

Rietmeijer F. J. M. (1995) Post-entry and volcanic contaminant abundance of zinc, copper, selenium, germanium and gallium in stratospheric micrometeorites. *Meteoritics* **30,** 33–41.

Rietmeijer F. J. M. and Flynn G. J. (1996) Lower stratospheric abundances of aluminum oxide and Al'-spheres > 9 micrometers from May 22, 1981 to July 1991 (abstract). *Meteorit. Planet. Sci.* **31,** A114–A115.

Robertson H. P. (1937) Dynamical effects of radiation in the solar system. *Mon. Not. Roy. Astron. Soc.* **97,** 423–438.

Rost D. (1995) Oberflächenanalysen von stratosphärischen Staubteilchen mit TOF-SIMS. Diplomarbeit, Universität Heidelberg. 86 pp.

Rost D., Stephan T., Jessberger E. K., Nakamura K. and Klöck W. (1998) New TOF-SIMS analyses of sections from stratospheric dust particles (abstract). *Lunar Planet. Sci.* **29,** #1637.

Rost D., Stephan T. and Jessberger E. K. (1999) Surface analysis of stratospheric dust particles. *Meteorit. Planet. Sci.* **34,** 637–646.

Sandford S. A. and Walker R. M. (1985) Laboratory infrared transmission spectra of individual interplanetary dust particles from 2.5 to 25 microns. *Astrophys. J.* **291,** 838–851.

Schiøtt H. E. (1970) Approximations and interpolation rules for ranges and range stragglings. *Radiat. Eff.* **6,** 107–113.

Schramm L. S., Brownlee D. E. and Wheelock M. M. (1989) Major elemental composition of stratospheric micrometeorites. *Meteoritics* **24,** 99–112.

Schwehm G. and Rohde M. (1977) Dynamical effects on circumsolar dust grains. *J. Geophys.* **42,** 727–735.

Schwieters J., Zehnpfenning J., Niehuis E. and Benninghoven A. (1990) Experimental study of the response of a liquid metal field ion source to short HV-extraction pulses. *J. Vac. Sci. Technol. A* **8,** 3752–3757.

Sigmund P. (1969) Theory of sputtering. I. Sputtering yield of amorphous and polycrystalline targets. *Phys. Rev.* **184,** 383–415.

Sigmund P. (1972) Collision theory of displacement damage, Lecture V: Some aspects of sputtering. *Rev. Roum. Phys.* **17,** 1079–1106.

Stadermann F. J. (1990) Messung von Isotopen- und Elementhäufigkeiten in einzelnen Interplanetaren Staubteilchen mittels Sekundärionen-Massenspektrometrie. Dissertation, Universität Heidelberg. 97 pp.

Stephan T. (1999) TOF-SIMS in cosmochemistry. Habilitationsschrift, Westfälische Wilhelms-Universität Münster. 107 pp.

Stephan T., Thomas K. L. and Warren J. L. (1994a) Comprehensive consortium study of stratospheric particles from one collector (abstract). *Meteoritics* **29,** 536–537.

Stephan T., Zehnpfenning J. and Benninghoven A. (1994b) Correction of dead time effects in time-of-flight mass spectrometry. *J. Vac. Sci. Technol. A* **12,** 405–410.

Stephan T., Jessberger E. K., Rulle H., Thomas K. L. and Klöck W. (1994c) New TOF-SIMS results on hydrated interplanetary dust particles (abstract). *Lunar Planet. Sci.* **25,** 1341–1342.

Stephan T., Thomas K. L. and Warren J. L. (1995) Particles from collection flag U2071 volume 1. Stratospheric dust catalog, MPI-Kernphysik, Heidelberg. 121 pp.

Stephan T., Rost D. and Jessberger E. K. (1997) Volatile-element enrichments in interplanetary dust due to nebular processes? In *Workshop on Parent-Body and Nebular Modification of Chondritic Materials* (eds. M. E. Zolensky *et al.*), pp. 59–60. LPI Tech. Rpt. 97–02, Part 1, Lunar and Planetary Institute, Houston.

Storms H. A., Brown K. F. and Stein J. D. (1977) Evaluation of a cesium positive ion source for secondary ion mass spectrometry. *Anal. Chem.* **49,** 2023–2030.

Sutton S. R. and Flynn G. J. (1988) Stratospheric particles: Synchrotron X-ray fluorescence determination of trace element contents. *Proc. Lunar Planet. Sci. Conf.* **18th,** 607–614.

Sutton S. R., Flynn G. J., Rivers M., Newville M. and Eng P. (2000) X-ray fluorescence microtomography of individual interplanetary dust particles (abstract). *Lunar Planet. Sci.* **31,** #1857.

Thomas K. L., Blanford G. E., Keller L. P., Klöck W. and McKay D. S. (1993) Carbon abundance and silicate mineralogy of anhydrous interplanetary dust particles. *Geochim. Cosmochim. Acta* **57,** 1551–1566.

Thomas K. L., Keller L. P., Blanford G. E. and McKay D. S. (1994) Quantitative analyses of carbon in anhydrous and hydrated interplanetary dust particles. *Analysis of Interplanetary Dust*, *Proc. AIP Conference 310* , 165–172 New York, USA. American Institute of Physics.

Thomas K. L., Blanford G. E., Clemett S. J., Flynn G. J., Keller L. P., Klöck W., Maechling C. R., McKay D. S., Messenger S., Nier A. O., Schlutter D. J., Sutton S. R., Warren J. L. and Zare R. N. (1995) An asteroidal beccia: The anatomy of a cluster IDP. *Geochim. Cosmochim. Acta* **59,** 2797–2815.

Turco R. P., Toon O. B., Whitten R. C. and Cicerone R. J. (1982) Space shuttle ice nuclei. *Nature* **298,** 830–832.

Wallenwein R., Blank H., Jessberger E. K. and Traxel K. (1987) Proton microprobe analysis of interplanetary dust particles. *Anal. Chim. Acta* **195,** 317–322.

Wallenwein R., Antz C., Jessberger E. K., Buttkewitz A., Knöchel A., Traxel K. and Bavdaz M. (1989) Multielement analysis of interplanetary dust particles with PIXES and SYXFA (abstract). *Lunar Planet. Sci.* **20,** 1171–1172.

Warren J. L. and Zolensky M. E. (1994) Collection and curation of interplanetary dust particles recovered from the stratosphere by NASA. *Analysis of Interplanetary Dust* (eds. M. E. Zolensky *et al.*), *Proc. AIP Conference 310* , 245–254 New York, USA. American Institute of Physics.

Wies C. (1998) Bestimmung der Elementzusammensetzung interplanetarer Staubteilchen. Diplomarbeit, Westfälische Wilhelms-Universität Münster. 78 pp.

Wilson L. and Huang T. C. (1979) The influence of shape on the atmospheric settling velocity of volcanic ash particles. *Earth Planet. Sci. Lett.* **44,** 311–324.

Wyatt S. P. and Whipple F. L. (1950) The Poynting-Robertson effect on meteor orbits. *Astrophys. J.* **111,** 134–141.

Zhang Y., Benoit P. H. and Sears D. W. G. (1993) Lew 88180, lew 87119, and alh 85119: New eh6, el7, and el4 enstatite chondrites (abstract). *Meteoritics* **28,** 468–469.

Zolensky M. E. and Thomas K. L. (1995) Iron and iron-nickel sulfides in chondritic interplanetary dust particles. *Geochim. Cosmochim. Acta* **59** (22), 4707–4712.

Zook H. A. and Berg O. E. (1975) A source for hyperbolic cosmic dust particles. *Planet. Space Sci.* **23,** 183–203.

Zook H. A. and McKay D. S. (1986) On the asteroidal component of cosmic dust (abstract). *Lunar Planet. Sci.* **17,** 977–978.